THE UNIVERSITY OF CHICAGO

MULTIMODE CIRCUIT QUANTUM ELECTRODYNAMICS

A DISSERTATION SUBMITTED TO
THE FACULTY OF THE DIVISION OF THE PHYSICAL SCIENCES
IN CANDIDACY FOR THE DEGREE OF
DOCTOR OF PHILOSOPHY

DEPARTMENT OF PHYSICS

BY
RAVI KAUSHIK NAIK

CHICAGO, ILLINOIS
DECEMBER 2018

To Mom, Dad, and Bro

TABLE OF CONTENTS

LIST OF FIGURES

LIST OF TABLES

ACKNOWLEDGMENTS

Through my six years in graduate school, I have been fortunate enough to not only learn about and participate in the world of experimental physics, but to also have so much fun in the process. I owe that good fortune to the many people that have supported me along the way.

First, I would like to thank my advisor Dave Schuster. Working with Dave has been a thrilling scientific experience; I never knew when he would come to me with a fun idea to try, whether it was related to what I was working on or not. He has shaped the way I approach research more than anyone else. But the most important thing is that create an inviting and enjoyable atmosphere in the Schuster Lab, allowing me to meet and work with an incredible group of scientists in our group.

Much, if not all, of the work presented in this thesis would not possible with the many people in the lab that I had the fortune to work alongside. First, I would like to mention the two postdocs that I worked with closest with during my time at Chicago. Vatsan Chakram was my partner in crime for most of the work presented in this thesis. Vatsan is the first person I go to for any scientific discussion I wanted to have. He has naturally inquisitive approach and treats even the craziest ideas with earnestness and sincerity, which makes him a pleasure to work with. I have many fond memories slogging late at night in lab with Vatsan, trying to understand the wackiest of datasets. I worked with Dave McKay during my first few years in the lab, as he mentored me on all parts of an experiment: design, fabrication, measurement, and analysis. He created our first multimode resonator sample and laid the groundwork for the random access memory experiments with both 2D and 3D resonators. His care and tenacity toward working through even the most frustrating experimental issues were and are an inspiration for me.

I have also been lucky to have many fellow graduate students that have been my cohorts over the years. Nelson Leung contributed heavily to our work on random access memories, helping with designing the sample, creating the data taking structure, and working through

the data analysis. Andrew Oriani helped considerably with the flute cavity fabrication and measurement. Akash Dixit has taken over integrating 3D cavities with superconducting qubits. Finally, I would like to thank my buddy Nate Earnest, who has been my cohort in the Schuster Lab from day one, for being my sounding board for all the silly ideas over the years. There are many more people in the lab that I have not yet mentioned here, but I have had so much fun interacting with them as both colleagues and friends.

These projects have also allowed me to work with several people outside the lab. I would like to thank Jens Koch and Peter Groszkowski, for adding soundness and clarity to the work through their theory contributions. I would also like to thank Dave Czaplewski at Argonne National Laboratory and Peter Duda at the Priztker Nanofabrication Facility for their guidance with fabrication.

Lastly, I would like to thank all the friends and family that have supported me throughout my graduate studies. In particular, I would like to thank my roommate Zach for reminding me to live in the moment and Mom, Dad, and my brother for their unconditional love.

ABSTRACT

In this thesis, we examine an extension of circuit quantum electrodynamics (QED), cavity QED using superconducting circuits, that utilizes multimode cavities as a resource for quantum information processing. We focus on the issue of qubit connectivity in the processors, with an ideal processor having random access – the ability of arbitrary qubit pairs to interact directly. Here, we implement a random access superconducting quantum information processor, demonstrating universal operations on a nine-qubit memory, with a Josephson junction transmon circuit serving as the central processor. The quantum memory is a multimode cavity, using the eigenmodes of a linear array of coupled superconducting resonators. We selectively stimulate vacuum Rabi oscillations between the transmon and individual eigenmodes through parametric flux modulation of the transmon frequency. Utilizing these oscillations, we perform a universal set of quantum gates on 38 arbitrary pairs of modes and prepare multimode entangled states, all using only two control lines. We thus achieve hardware-efficient random access multi-qubit control. We also explore a novel design for creating long-lived 3D cavity memories compatible with this processor. Dubbed the "quantum flute", this design is monolithic, avoiding the loss suffered by cavities with a seam between multiple parts. We demonstrate the ability to manipulate the spectrum of a multimode cavity and also measure photon lifetimes of 0.5-1.3 ms for 21 modes. The combination of long-lived quantum memories with random access makes for a promising architecture for quantum computing moving forward.

CHAPTER 1

INTRODUCTION

1.1 Cavity Quantum Electrodynamics

One of the fundamental interactions in nature is that between light and matter. Understanding and controlling the quantum mechanical nature of this interaction is a major topic of modern research. However, due to the small cross section of atoms with respect to light, coupling a single atom and photon is challenging. To enhance the strength of coupling, the atoms and light can be trapped in a cavity, confining the light and thus increasing the effective cross section. Due to this discovery, a number of measurements have been demonstrating controlled coupling between single photons and atoms, a field known as cavity quantum electrodynamics (QED).

1.2 Superconducting Circuits

While cavity QED with atoms has produced impressive results in the field of quantum control, it still has several limits in overall coupling strength, as well as flexibility and tunability. However, recent developments have led to a promising alternative: superconducting circuit quantum electrodynamics [57]. Using superconducting printed circuits, we can create lossless microwave circuit elements, including inductors, capacitors, and waveguides. Crucially, the addition of a non-linear element, the Josephson junction, allows for the creation of "artificial atoms". Due to macroscopic size of the artificial atoms, the coupling strength between microwave photons and the atoms can be made very large, allowing for the exploration of very interesting regimes. Additionally, since the circuits can be printed, there is a large degree of flexibility in geometry and connectivity in the circuits. Finally, including multiple Josephson junctions in a loop to create a superconducting quantum interference device (SQuID) allows for in-situ tunability via magnetic flux through the loop.

1.3 Near-term Quantum Information Processing

The aforementioned quantum control capabilities of superconducting circuits make them promising candidates for the components of a quantum information processor. In fact, recent progress in the field has shown that circuit QED-based processors are rapidly approaching the requirements for demonstrating quantum advantage. Quantum information processors can provide a notable computational enhancement for a number of potential applications, including encryption, data processing, and quantum simulation of many-body systems.

1.4 Thesis Overview

In this thesis, we will discuss progress towards building a quantum information processor with superconducting circuits. First, we will provide an overview of cavity and circuit QED, describing the relevant Hamiltonians and how to manipulate them. Next, we will discuss an implementation of a particular quantum processor involving multimode cavities. Here, we will demonstrate universal quantum control of a multi-qubit memory with random access using a single central processing unit. We will characterize the fidelity of gates on and large entangled states of this memory. Then, we will show how implementing this processor using long-lived quantum memories comprised of bulk, three-dimensional (3D) superconducting cavities is a particularly enticing architecture toward demonstrating quantum advantage in the near-term. After that, we will consider a novel method for a making long-lived cavities that are monolithic and seamless. We show how this method can be used to make a variety of geometries and spectral distributions, with a focus on how to create multimode cavities. Finally, we will conclude on a outlook for how this architecture can be scaled to a viable quantum computer.

CHAPTER 2

CIRCUIT QUANTUM ELECTRODYNAMICS

Cavity quantum electrodynamics (QED) is an essential component in the study of a fundamental interaction in a nature: that between matter and light. Generally, the interaction strength between single quanta of light and matter, photons and atoms, respectively, is very small, due to the small electromagnetic cross section of atoms, making the physics difficult to study experimentally. However, cavity QED provides a remedy to this by trapping the photons and atoms in a cavity, enhancing the interaction strength by confining the photon locally to the atom.

In this chapter, we will first describe the dynamics describing the physics of cavity QED. Then, we lay the foundations for circuit QED, beginning with the Josephson junction and describing how we can recreate cavity QED with superconducting circuits. Finally, we will describe coherent control of a circuit QED system and describe basic experiments used to characterize the components of the system.

2.1 Jaynes-Cummings Hamiltonian

In order to understand the dynamics of cavity QED, we consider a simple hybrid system: a two-level system, a qubit, coupled to a harmonic oscillator, shown in Figure 2.1. That system is described by the Jaynes-Cummings Hamiltonian:

$$H = \hbar\omega_c a^\dagger a + \frac{\hbar}{2}\omega_q \sigma_z + \hbar g(a\sigma_+ + a^\dagger \sigma_-). \tag{2.1}$$

Here, ω_c and ω_q are the cavity and qubit resonance frequencies, respectively, and g is the resonant coupling rate between the qubit and the cavity. The Hilbert space of this Hamiltonian

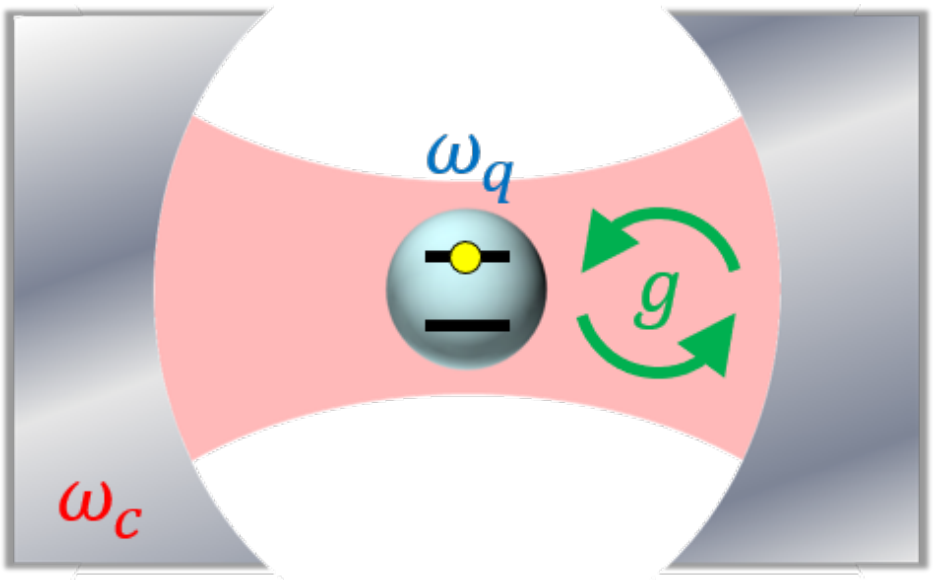

Figure 2.1: Cavity quantum electrodynamics. This is a cartoon depiction of a hybrid quantum system: an atom coupled to an electromagnetic field in a cavity. To simplify matters, the atom is a two-level system, a qubit. The dynamics of this system are explained by the Jaynes-Cummings Hamiltonian, equation 2.1.

consists of superpositions of the form

$$|\psi\rangle = \sum_{n=0}^{\infty} \sum_{i \in \{g,e\}} a_{n,i} \, |n, i\rangle \, , \tag{2.2}$$

where $|n\rangle$ is the Fock state of the cavity with n photons and $|g\rangle$ and $|e\rangle$ are the ground and excited states of the qubit, respectively.

To understand the dynamics under this Hamiltonian, it is instructive to consider a couple of parameter regimes. First, let the qubit and cavity transition frequencies be resonant, $\omega = \omega_c = \omega_q$. The eigenmodes of this Hamiltonian are $|\psi_\pm\rangle = \frac{1}{\sqrt{2}} \left(|n+1, g\rangle \pm |n, e\rangle \right)$, with eigenfrequencies $\omega_\pm = \omega \pm g$, respectively. If the system is initialized with the qubit excited and n photons in the cavity, $|n, e\rangle = \frac{1}{\sqrt{2}}(|\psi_+\rangle - |\psi_-\rangle)$, then the state after a time t is:

$$|\psi(t)\rangle = \cos(gt) \, |n, e\rangle + \sin(gt) \, |n+1, g\rangle \, . \tag{2.3}$$

Here, the system undergoes vacuum Rabi oscillations, where the excitation is swapped be-

tween the qubit and cavity at a rate g. This interaction allows for the qubit and cavity to exchange coherent quantum information, as well as enabling entanglement between the two.

Another regime to consider is the dispersive limit, when the qubit and the cavity are far off resonance $\Delta = \omega_q - \omega_c \gg g$, where g is the coupling strength. Here, the Hamiltonian (2.1) can be approximated as:

$$H = \hbar\omega_c a^\dagger a + \frac{\hbar}{2}\omega_q \sigma_z + \hbar\chi a^\dagger a \sigma_z, \tag{2.4}$$

where $\chi = g^2/\Delta$. It is instructive to rewrite the Hamiltonian in a couple of suggestive forms:

$$H = \hbar(\omega_c + \chi\sigma_z)a^\dagger a + \frac{\hbar}{2}\omega_q\sigma_z, \tag{2.5}$$

$$H = \hbar a^\dagger a + \hbar\left(\frac{\omega_q}{2} + \chi a^\dagger a\right)\sigma_z. \tag{2.6}$$

In the first form, we see that the cavity incurs a frequency shift dependent on the qubit state. This allows for a critical feature of cavity QED, the ability to perform quantum non-demolition (QND) measurement of the qubit state by probing the cavity. The second form, where the qubit frequency is dependent on the photon number state of the cavity is known as photon number splitting. In situations where the cavity state needs to be measured, the qubit can then be probed to determine the cavity occupation. The eigenstates of Equation (2.4) are weakly hybridized cavity and qubit states:

$$|\psi_c\rangle \approx |n+1, g\rangle + \frac{\sqrt{n}g}{\Delta}|n, e\rangle \tag{2.7}$$

$$|\psi_q\rangle \approx |n, e\rangle + \frac{\sqrt{n}g}{\Delta}|n+1, g\rangle \tag{2.8}$$

The dynamics described above represent the unitary evolution of a cavity QED system. However, because the system is not fully isolated from its environment, we need to consider incoherent processes as well. The first type of loss is decay, where the excited qubit or cavity

emits a photon which is absorbed by the environment. The rate of decay is governed by Fermi's golden rule:

$$\kappa = \frac{2\pi}{\hbar} |\langle n| H_{\text{env}} |n+1\rangle|^2 S(\omega_c), \tag{2.9}$$

$$\gamma = \frac{2\pi}{\hbar} |\langle g| H_{\text{env}} |e\rangle|^2 S(\omega_q), \tag{2.10}$$

where κ and γ are the cavity and qubit decay rates, respectively, $S(\omega)$ is the density of states of the interacting environment at frequency ω, and H_{env} is the Hamiltonian describing the coupling between cavity-qubit system and the environment. Here, we see that when the qubit and cavity are in the dispersive limit, the cavity can actually provide protection for the qubit. Since the cavity reflects radiation that is off resonance from its frequency, the qubit is shielded from environmental noise at its frequency while in the cavity.

However, when the cavity is used for readout of the qubit, as discussed above, the cavity is made intentionally transparent, such that $\kappa \gg \gamma$, so that information is extracted from the cavity before the qubit decays. Because the qubit and cavity are hybridized, the decay rate of the cavity places a lower bound on the decay rate of the qubit, a phenomenon known as the Purcell effect [51]. This decay rate is given by:

$$\gamma_p = \frac{ng^2}{\Delta^2}\kappa. \tag{2.11}$$

In addition to decay, another incoherent process that quantum systems suffer from is dephasing: the scrambling of the phase of a quantum superposition. The sources of dephasing vary from system to system, but one universal cause in cavity QED is due to residual excitations in the system. As seen in Equation (2.6), any residual photons in the cavity would cause the qubit frequency to shift. For a qubit prepared in superposition,$\psi(0) = a|g\rangle + b|e\rangle$, the time evolution of the qubit is

$$|\psi(t)\rangle = a|g\rangle + be^{i\omega_q t}|e\rangle. \tag{2.12}$$

However, in the presence of qubit frequency fluctuations, the phase of the superposition would be scrambled, leading to decoherence.

2.2 Josephson Junctions

Now that we have introduced cavity QED, we explain how to create the system using superconducting circuits. Superconductors are special materials that demonstrate quantum coherence over large distances due to the condensation of pairs of conducting electrons, known as Cooper pairs. Because of this, we can use them to create quantum circuits consisting of macroscopic numbers of atoms with wavefunctions spanning distances of several centimeters. However, classical circuit elements, such as inductors, capacitors, and transmission lines, only allow for the creation of linear elements. To introduce non-linearity into the system, we investigate the central element essential to superconducting circuits: the Josephson junction [29].

The Josephson junction consists of two superconducting leads separated by a weak link in the form of an insulator, normal metal, or constriction. Here, we will focus on superconducting-insulator-superconducting (S-I-S) junctions. The dynamics of Josephson junction are determined by two relations:

$$V(t) = \frac{\Phi_0}{2\pi}\frac{\partial\varphi(t)}{\partial t} \tag{2.13}$$

$$I(t) = I_c \sin\left(\varphi(t)\right) \tag{2.14}$$

where $\Phi_0 = h/(2e)$ is the magnetic flux quantum, V is the voltage across the junction, I is the current across the junction, φ is the phase difference of the superconducting wavefunction across the Josephson junction, and I_c is the critical current of the junction, the maximum current before the junction becomes a normal resistive junction. We can combine these

relations:

$$\frac{\partial I(t)}{\partial t} = I_c \cos(\varphi) \frac{\partial \varphi(t)}{\partial t}, \tag{2.15}$$

$$V(t) = \frac{\Phi_0}{2\pi I_c \cos(\varphi(t))} \frac{\partial I(t)}{\partial t}. \tag{2.16}$$

We recognize the form of the Equation (2.16) as Faraday's law of induction. Thus, a Josephson junction behaves like a non-linear inductor, with an inductance of

$$L = \frac{\Phi_0}{2\pi I_c \cos(\varphi(t))}. \tag{2.17}$$

To understand the dynamics of Josephson junctions, we find the energy stored in the junction as current passes through it. With the junction initialized in a state $\varphi = 0$, the energy stored in the junction is

$$U = \int_0^t IV \mathrm{d}t. \tag{2.18}$$

Substituting in the Josephson relations (Equations (2.13) and (2.14)):

$$U = \frac{\Phi_0 I_c}{2\pi}(1 - \cos(\varphi)). \tag{2.19}$$

We define the coefficient as the Josephson energy, $E_J = \Phi_0 I_c / 2\pi$.

2.3 Quantum Bits with Superconducting Circuits

Now that we have introduced the Josephson junction, we build the framework for understanding the dynamics of superconducting circuit QED. First, we consider the simple example of an LC circuit. The energy in the circuit is given by:

$$H = \frac{\Phi^2}{2L} + \frac{q^2}{2C} \tag{2.20}$$

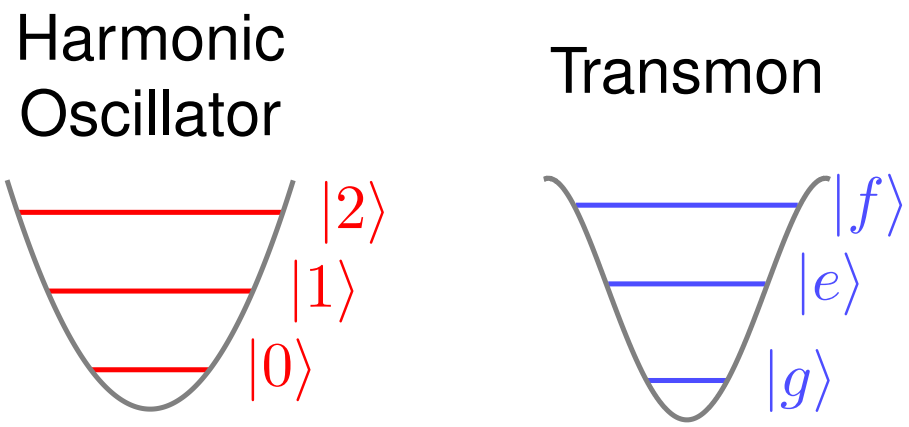

Figure 2.2: The potentials and energy landscape for a harmonic oscillator and a transmon. The anharmonicity of the transmon allows us to address individual energy level transitions.

where Φ is the flux through the inductor and q is the charge on the capacitor. The resonance frequency of this circuit is $\omega_0 = 1/\sqrt{LC}$ and its impedance is $Z_0 = \sqrt{L/C}$. To quantize this circuit [66], we write the flux and charge as operators:

$$\Phi = \sqrt{\frac{\hbar Z_0}{2}}(a + a^\dagger), \tag{2.21}$$

$$q = i\frac{\hbar}{2Z_0}(a^\dagger - a). \tag{2.22}$$

where $c(c^\dagger)$ is the annihilation (creation) operator, satisfying the commutation relation $[c, c^\dagger] = 1$. With this quantization, the Hamiltonian in Equation (2.20) becomes:

$$H = \hbar\omega_0 \left(a^\dagger a + \frac{1}{2}\right), \tag{2.23}$$

the familiar Hamiltonian for a harmonic oscillator.

Now that we created the cavity portion of circuit QED, we can move to the qubit portion. Unlike the cavity, the qubit cannot be created with linear elements alone. This is where the Josephson junction comes into play. If we replace the inductor in our circuit with a Josephson

junction, the circuit Hamiltonian becomes:

$$H = 4E_C n^2 + E_J(1 - \cos(\varphi)) \tag{2.24}$$

where $E_C = e^2/2C$ is the charging energy of an electron and $n = q/2e$ is the number of Cooper pairs on one side of the capacitor. This circuit is generally known as a charge qubit and can be considered in a number of parameter regimes, including the Cooper pair box [47] and quatronium [59] regimes, but here we will focus on the transmon [33] regime, where $E_J \gg E_C$. In this regime, the Hamiltonian is insensitive to fluctuations in the charge on the capacitor, and the circuit dynamics is well described by expanding Equation (2.24) for small $\varphi \ll \pi$. The resulting Hamiltonian is:

$$H = 4E_C n^2 + E_J \left(\frac{\varphi^2}{2} - \frac{\varphi^4}{24} \right). \tag{2.25}$$

We need to bound the range of this Hamiltonian to a single well, otherwise the potential would be unbound. We quantize this Hamiltonian analogous to the classical case, with $n = q/2e$ and $\varphi = \Phi/\Phi_0$. Upon using the transformations in Equations (2.21) and (2.22), the Hamiltonian becomes:

$$H = \hbar\omega_q a^\dagger a + \hbar\alpha a^\dagger a(a^\dagger a - 1) \tag{2.26}$$

where $\omega_q = \sqrt{8E_J E_C} - E_C$ is the fundamental frequency and $\alpha = -E_C$ is the anharmonicity. We recognize this Hamiltonian as that of an anharmonic oscillator, known as the Duffing oscillator [18]. The anharmonicity of the transmon is crucial in allowing for addressability of individual transitions within the energy landscape. The eigenstates of the transmon will be labelled $|g\rangle, |e\rangle, |f\rangle ...$ The lowest two levels, $|g\rangle$ and $|e\rangle$, of a transmon can thus be thought of as a individually addressable qubit. A comparison of the harmonic and transmon potentials and energy levels is shown in Figure 2.2.

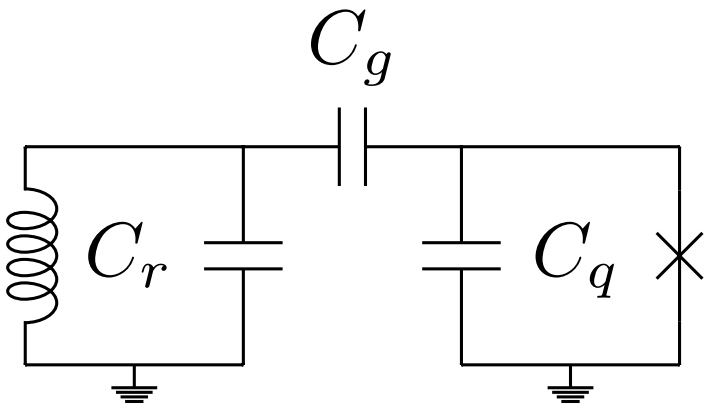

Figure 2.3: Capacitive coupling between an LC resonator and a transmon. The ratio between the coupling capacitance C_g and the total capacitance of the circuit determines the coupling rate between the resonator and transmon.

Now that we are able to recreate both qubit and cavity with superconducting circuits, we need to establish coupling between the two. In circuit QED, this can be achieved a number of ways. A simple method is by introducing a mutual capacitance, C_g, between the two circuits, as shown in the diagram in Figure 2.3. The effective coupling rate for such a circuit is given by [33]

$$g = 2\beta e V_{\text{rms}}^0 \left(\frac{E_J}{8E_C}\right)^{1/4}, \tag{2.27}$$

where $\beta = C_g/C_\Sigma$ is the ratio between the coupling capacitance and the total capacitance, C_Σ, and $V_{\text{rms}}^0 = \sqrt{\hbar\omega_r/2C_r}$ is the root-mean-square voltage on the resonator's capacitor.

Now that we have established coupling in circuit QED, it is important to note a specific difference in the dispersive Hamiltonian when we consider the transmon as a multilevel system beyond a qubit. Due to the presence of higher energy levels, the state-dependent dispersive shift χ (Equation (2.4)) is reduced to [33]

$$\chi = \frac{g^2}{\Delta}\left(\frac{\alpha}{\Delta+\alpha}\right). \tag{2.28}$$

Because the parameters in circuit QED are customizable, we can achieve a wide variety of Hamiltonian regimes, one of the greatest strengths of cavity QED. Nonetheless, there are

limitations to the regimes we can access. First, superconducting properties have a fundamental gap for production of single electron quasiparticles from the Cooper pair bath. This gap is directly related to the critical temperature of the superconductor. For aluminum, the most common material for superconducting circuits, this gap is $\Delta = h(44\text{ GHz})$ [12]. This sets an upper bound on the energy parameters allowed in the Hamiltonian.

Additionally, the circuits need to be initialized in a known, well-defined pure quantum state, ideally the ground state, so that they can be used for quantum control without error. From the Bose-Einstein distribution [4], we see that the excited state population of a resonator with fundamental frequency ω at a temperature T is

$$\bar{n} = \frac{1}{e^{\hbar\omega/k_B T} - 1}. \tag{2.29}$$

In modern dilution fridges, a typical temperature base temperature is 20 mK. To insure that the excess excited state population is less than 1%, the fundamental transition frequencies of the transmons and resonators in our circuits must be more than 2 GHz. However, at 4 GHz, the excess excited state population is already $\bar{n} < 1 \times 10^{-4}$. Typical experiments in circuit QED have transition frequencies from 4-12 GHz, with anharmonicities from 100-300 MHz. Notably, coupling strengths up to several hundreds of MHz are possible, meaning ratios of $g/\omega \sim 10^{-1}$ are possible. That is a significant improvement over atomic cavity QED systems, where, at a maximum, $g/\omega \sim 10^{-6}$.

In addition to charge qubits like the transmon, a number of other types of circuits have been designed using superconducting circuit elements, including phase qubits [39, 38], flux qubits [45, 37, 68, 19], and more complex multi-nodal circuits [5, 26]. These circuits allow for extended coherence times, greater tunability, and larger anharmonicities, at the cost of greater complexity in design, fabrication, and control and are a promising area of active research.

2.4 Quantum Control in Circuit QED

Here, we provide a brief overview of preparation and manipulation of the quantum states with the elements of circuit QED. First, we replace the single Josephson junction in the transmon circuit with a pair of junctions in parallel, known as the superconducting quantum interference device (SQuID) [11]. Assuming the junctions have Josephson energies E_{J1} and E_{J2}, the resulting total junction Hamiltonian is

$$H_J = -(E_{J1} + E_{J2}) \cos\left(\pi \frac{\Phi}{\Phi_0}\right) \cos(\varphi) - (E_{J1} - E_{J2}) \sin\left(\pi \frac{\Phi}{\Phi_0}\right) \sin(\varphi). \tag{2.30}$$

where Φ is the external flux penetrating the SQuID loop. From (2.30), we see that the total Josephson energy is tunable via an externally applied flux, in a range $E_{J1} - E_{J2} < E_J < E_{J1} + E_{J2}$. If the two junctions are symmetric ($E_{J1} = E_{J2}$), the E_J can be turned all the way to zero. This functionality allows for complete in-situ tunability of the transmon transition frequency. In the symmetric junction case, the fundamental transmon frequency is given by

$$\hbar\omega_q = \sqrt{8E_C E_J \left|\cos\left(\pi \frac{\Phi}{\Phi_0}\right)\right|} - E_C \tag{2.31}$$

where E_J is the sum of the Josephson energies of the junctions. The ability of in-situ tunability of the transmon transition frequencies allows us to move between different regimes of circuit QED, from strong coupling to dispersive, with ease. This allows for flexibility in readout, as well as control over coupling rates. Additionally, as we will see in section 3.2, it also allows for parametric control of a circuit QED system with AC flux modulation.

To address the transmon directly, we apply a microwave tone to a transmission line that is capacitively coupled to transmon, referred to as the charge bias line. The microwave tone alternates the voltage, and thus the relative charge on the transmon capacitor pads. Thus, the electric field of the applied tone couples to the dipole moment of the transmon. Treating

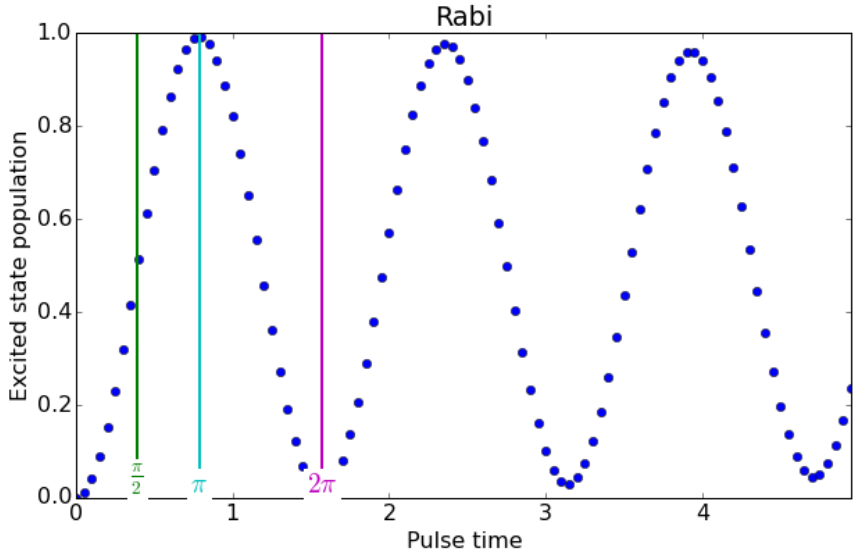

Figure 2.4: An example of a Rabi oscillation of a driven qubit, with the excited state population of the qubit measured for each point after the qubit is driven for a time. The Rabi oscillation experiment is used to calibrate the pulses required to excite the qubit (π), prepare an equal superposition of the qubit ($\pi/2$), or rotate the qubit entirely (2π) to apply a phase flip to a superposition.

the transmon as a qubit, the Hamiltonian for the driven qubit is

$$H = \hbar\omega_q a^\dagger a + \hbar\alpha a^\dagger a(a^\dagger a - 1) + \varepsilon \sin(\omega_D t)(a + a^\dagger) \tag{2.32}$$

where ε is the strength of the applied drive to the transmon. When this drive frequency is resonant with the fundamental transition frequency of the transmon, the transmon undergoes a Rabi oscillation, sequential stimulated absorption and emission of photons, as shown in Figure 2.4. This oscillation occurs at a rate proportional to ε and provides an essential tool to prepare arbitrary quantum states of the transmon, using the pulse lengths described in the figure. However, when the bandwidth of the applied drive approaches the anharmonicity of the transmon, a limit is placed on the rate of the oscillations to avoid spurious excitations up to higher energy levels. These limitations can be somewhat overcome by using specially shaped pulses to modify the Fourier profile of the applied drive [9].

An image of an actual circuit QED device is shown in Figure 2.5. In this case, the

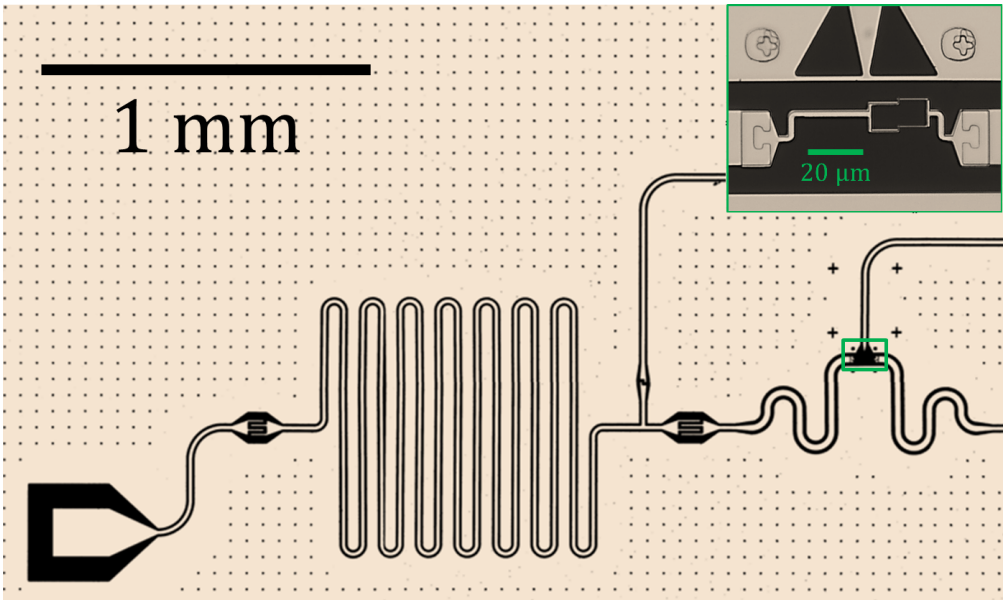

Figure 2.5: An optical image of a flux-tunable transmon qubit coupled to a coplanar waveguide resonator. The light-shaded area is the superconducting film, where the dark area is the gap region, with entire circuit on top of dielectric. The resonator is coupled to external electronics via two interdigitated finger capacitors, to allow for transmission measurement. It is also coupled capacitively to a transmon qubit, which is tunable via an external flux. The inset shows the SQuID of the transmon, as well as its mutual inductance flux bias line above it.

resonator is a coplanar waveguide (CPW), where the resonance frequency is inversely proportional to the length of resonator. In this image, the charge drive of the qubit is through the resonator. While this allows for filtering of the noisy environment of the drive line, it also reduces the strength of applied drives on the qubit.

CHAPTER 3

CONTROL OF CAVITY-BASED QUANTUM MEMORIES

Superconducting circuit quantum electrodynamics (cQED), introduced in the previous chapter, is rapidly progressing towards small and medium-scale quantum computation [15]. Superconducting circuits consisting of lattices of Josephson junction qubits [30, 8] have been used to realize quantum information processors relying on nearest-neighbor interactions for entanglement. An outstanding challenge in cQED is the realization of architectures with high qubit connectivity, the advantages of which have been demonstrated in ion trap quantum computers [28, 14, 34]. Classical computation architectures typically address this challenge by using a central processor which can randomly access a large memory, with the two elements often comprising distinct physical systems. Here, we present a quantum analog of this architecture, realizing a random access quantum information processor using cQED.

Quantum logic elements, such as superconducting qubits, are expensive in terms of control resources and have limited coherence times. Quantum memories based on harmonic oscillators, instead, can have coherence times two orders of magnitude longer than the best qubits [54, 53, 50], but are incapable of logic operations on their own. This observation suggests supporting each logic-capable processor qubit with many memory qubits. In the near term, this architecture provides a means of controlling tens of highly coherent qubits with minimal cryogenic and electronic-control overhead. To build larger systems compatible with existing quantum error correction architectures [21, 22, 31, 44], one can connect individual modules consisting of a single processor qubit and a number of bits of memory while still accessing each module in parallel.

In this chapter, we describe the use of a single non-linear element to enable universal quantum logic with random access on a collection of harmonic oscillators, as shown in Figure 3.1. We store information in distributed, readily accessible, and spectrally distinct resonator modes. We show how to perform single qubit gates on arbitrary modes by using frequency-selective parametric control [2, 63, 60, 41, 69, 48] to exchange information be-

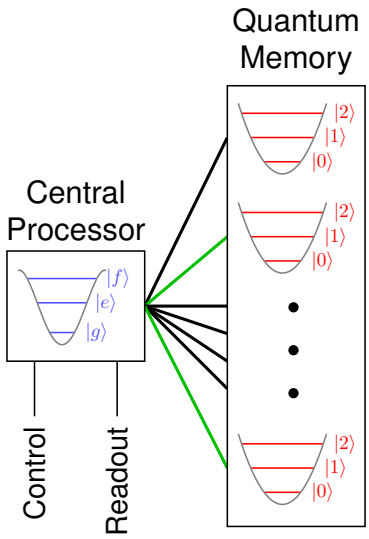

Figure 3.1: Random access with multiplexed control. The quantum memory consists of harmonic oscillator modes, with each mode accessible to a central processor, in this case a transmon. This allows for quantum operations between two arbitrary memory modes (such as those highlighted in green) via the central processing transmon and its control lines.

tween a superconducting transmon qubit [33] and individual resonator modes. Next, using higher levels of the transmon, we realize controlled-phase (CZ) and controlled-NOT (CX) gates on arbitrary pairs of modes. Therefore, we demonstrate all the ingredients necessary for universal quantum computation with harmonic modes. Finally, we use these tools to prepare multi-mode entangled states as an important step towards quantum error correction. Note that the content of this chapter is based on previously published work [46] with permission [13].

3.1 Multimode cavities

Our multimode quantum memory implementation uses the eigenmodes of a linear array of $n = 11$ nominally identical, coupled, half-wave transmission line resonators [40], as shown in Figure 3.2. The array is described by the Hamiltonian:

$$\hat{H}_{\mathrm{mm}} = \sum_{j=1}^{n} h\nu_{\mathrm{r}} \hat{c}_j^{\dagger}\hat{c}_j + \sum_{j=1}^{n-1} hg_{\mathrm{r}}(\hat{c}_j^{\dagger}\hat{c}_{j+1} + \hat{c}_j\hat{c}_{j+1}^{\dagger}), \tag{3.1}$$

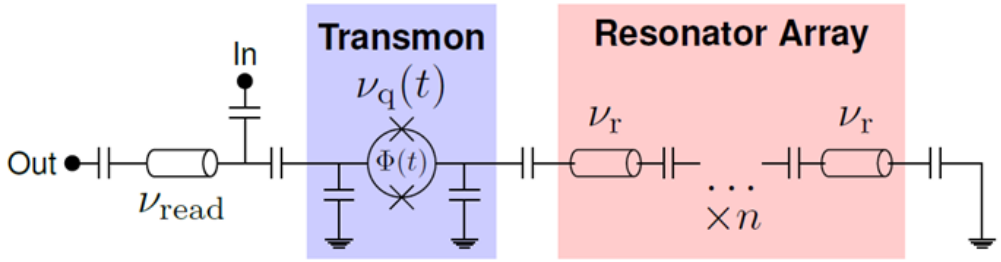

Figure 3.2: Schematic of the random access quantum information processor. The circuit comprises an array of 11 identical half-wave transmission line resonators, capacitively coupled strongly to each other. One end of the array is capacitively coupled to a tunable transmon qubit. The transmon is measured with a separate transmission line resonator.

where ν_r is the resonance frequency of the identical resonators, g_r is the coupling rate between neighboring resonators, and $\hat{c}_j^\dagger$ ($\hat{c}_j$) is the operator that creates (annihilates) photons in the resonator at spatial index j. The single-photon eigenmodes of this circuit are 11 distributed "momentum" states of the array.

The eigenmodes and eigenfrequencies of the tight-binding Hamiltonian of Equation (3.1) are [40]:

$$|\psi\rangle_k = \sum_{j=1}^{n} \sqrt{\frac{2}{n+1}} \sin\left(\frac{jk\pi}{n+1}\right) |1\rangle_j, \tag{3.2}$$

$$\nu_k = \nu_r - 2g_r \cos\left(\frac{k\pi}{n+1}\right) \quad k \in \{1, n\}, \tag{3.3}$$

where $|\psi\rangle_k$ and ν_k are the kth eigenmode and eigenfrequency, respectively, and $|1\rangle_j$ is the state with a single photon in the jth resonator of the array and with all other resonators in the ground state.

One end of the array is capacitively coupled to a tunable transmon qubit. Importantly, every mode has non-zero amplitude at the edge, allowing a transmon to couple to each mode. The Hamiltonian of the combined system is:

$$\hat{H} = h\nu_q(t)\hat{a}^\dagger\hat{a} + \frac{1}{2}h\alpha\,\hat{a}^\dagger\hat{a}(\hat{a}^\dagger\hat{a} - 1) + \sum_{k=1}^{n} h\nu_k\hat{b}_k^\dagger\hat{b}_k + \sum_{k=1}^{n} hg_k(\hat{b}_k + \hat{b}_k^\dagger)(\hat{a} + \hat{a}^\dagger), \tag{3.4}$$

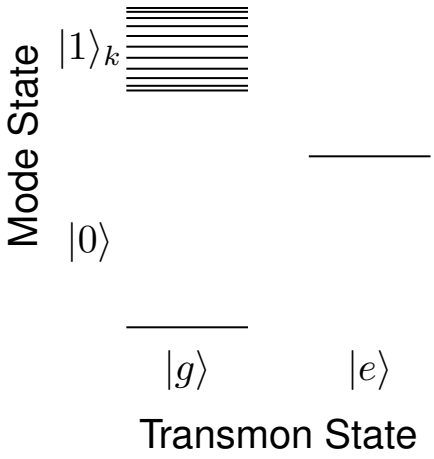

Figure 3.3: Energy level diagram of the combined transmon-multimode memory manifold, restricted to single excitations. The state $|1\rangle_k$ corresponds to a photon in mode k and all other modes in the ground state.

where the transmon is treated as a Duffing oscillator [33] with anharmonicity α, coupled to the modes with frequency ν_k and coupling strength g_k. The operators $\hat{a}^\dagger$ ($\hat{a}$) and $\hat{b}_k^\dagger$ ($\hat{b}_k$) create (annihilate) photons in the transmon and in eigenmode k, respectively. Thus,

$$b_k|n\rangle_k = \sum_{j=1}^{n} \sqrt{\frac{2}{n+1}} \sin\left(\frac{jk\pi}{n+1}\right) c_j|n\rangle_j \tag{3.5}$$

The coupling between the transmon and a given eigenmode is given by:

$$g_k = g_{\mathrm{q}} \sqrt{\frac{2}{n+1}} \sin\left(\frac{k\pi}{n+1}\right). \tag{3.6}$$

The resulting energy level diagram for the combined system, restricted to single excitations manifold, is shown in Figure 3.3.

3.2 Parametric flux-modulation of a transmon qubit

Given access to the multimode memory via the transmon, we demonstrate methods to address each mode individually. In many circuit QED schemes, excitations are loaded into modes by adiabatically tuning the qubit frequency through or near a mode resonance [16].

This works well for single modes, but for a multimode manifold, one must carefully manage Landau-Zener transitions through several modes [40], to avoid leaving residual excitations elsewhere in the manifold. Also, the qubit must be returned to the far-dispersive regime to minimize spurious unwanted interactions, requiring longer gate durations.

The frequency of the transmon is tunable using the magnetic flux threading the SQuID loop of the transmon, controlled by passing a current through a nearby flux line. For a sinusoidally modulated flux, the transmon $|g\rangle - |e\rangle$ transition frequency is:

$$\nu_{\mathrm{ge}}\left(\Phi\left(t\right)\right) = \nu_{\mathrm{ge}}\left(\Phi_b + \epsilon_\Phi \sin\left(2\pi\nu_{\mathrm{sb}}t + \phi\right)\right) \approx \bar{\nu}_{\mathrm{ge}} + \epsilon \sin\left(2\pi\nu_{\mathrm{sb}}t + \phi_{\mathrm{m}}\right) \tag{3.7}$$

where $\bar{\nu}_{\mathrm{ge}} = \nu_{\mathrm{ge}}\left(\Phi_b\right) + \delta\nu_{\mathrm{DC}}(\Phi_b, \epsilon_\Phi)$ is the mean qubit frequency during the flux modulation. The relation between the frequency (ϵ) and flux (ϵ_Φ) modulation amplitudes and the DC-shift of the transmon frequency during flux-modulation are:

$$\epsilon = \epsilon_\Phi \left.\frac{d\nu_{\mathrm{ge}}}{d\Phi}\right|_{\Phi_b} \quad \text{and} \quad \delta\nu_{\mathrm{DC}} = \frac{\epsilon_\Phi^2}{4} \left.\frac{d^2\nu_{\mathrm{ge}}}{d\Phi^2}\right|_{\Phi_b}, \tag{3.8}$$

respectively. Note that this approximation is only valid in regime where $\epsilon \ll |\nu_{\mathrm{ge}}(\Phi = 0) - \bar{\nu}_{\mathrm{ge}}|$, so that the linear term in the flux-to-frequency relation is dominant. The frequency is shifted from its bare value due to the non-linear flux dependence of the transmon frequencies, and is quadratic in the modulation amplitude.

We obtain a simple description for parametric control of this system by considering the Hamiltonian of Equation (3.4) and using to the lowest two transmon levels as the eigenstates of a qubit, with resonance frequency ν_q. The Hamiltonian then reduces to:

$$\hat{H} = \sum_{k=1}^{n} h\nu_k \hat{b}_k^\dagger \hat{b}_k + \frac{1}{2} h\nu_q(t)\hat{\sigma}_z + \sum_{k=1}^{n} hg_k(\hat{b}_k + \hat{b}_k^\dagger)(\hat{\sigma}_- + \hat{\sigma}_+). \tag{3.9}$$

In this work, we focus on iSWAP interactions between the transmon and the resonator mode. As a result, we modulate the transmon frequency near the the difference frequencies of the

memory modes and transmon. The $(\hat{b}_k\hat{\sigma}_- + \text{c.c.})$ terms in Equation (3.9) can be therefore be dropped in the rotating-wave approximation. When one of these sidebands is resonant with a mode of the memory, the system experiences stimulated vacuum Rabi oscillations: parametrically induced exchange of a single photon between the transmon and the selected mode. These sidebands manifest in a rotating frame defined by the transformation [2, 63]:

$$U(t) = \exp\left[-2\pi i\left(\bar{\nu}_{ge}t - \frac{\epsilon}{2\nu_{sb}}\cos\left(2\pi\nu_{sb}t\right)\right)\hat{\sigma}_z - 2\pi i\nu_k\hat{b}_k^\dagger\hat{b}_k t\right]. \tag{3.10}$$

In this rotating frame, the Hamiltonian is transformed to:

$$\begin{aligned}\hat{H}' = U\hat{H}U^\dagger - iU\partial_t U^\dagger &= \sum_{j=1}^{n} hg_k J_0\left(\frac{\epsilon}{2\nu_{\text{sb}}}\right)\left(e^{-2\pi i\Delta_k t}\hat{b}_k^\dagger\hat{\sigma}_- + e^{2\pi i\Delta_k t}\hat{b}_k\hat{\sigma}_+\right) \\ &+ \sum_{j=1}^{n} hg_k\hat{b}_k^\dagger\hat{\sigma}_-\left(\sum_{m=1}^{\infty}(-1)^m J_m\left(\frac{\epsilon}{2\nu_{\text{sb}}}\right)e^{2\pi i(m\nu_{\text{sb}}-\Delta_k)t}\right) \\ &+ \text{c.c.},\end{aligned} \tag{3.11}$$

where $\Delta_k = \nu_k - \bar{\nu}_{ge}$, is the detuning between the qubit and the k^{th} eigenmode. When $\nu_{sb} = \Delta_k$, we obtain resonant first-order sideband transitions between the transmon and mode k, described by:

$$H'_{\text{sb},k} = hg_k J_1\left(\frac{\epsilon}{2\nu_{\text{sb}}}\right)\left(\hat{b}_k^\dagger\hat{\sigma}_- + \hat{b}_k\hat{\sigma}_+\right). \tag{3.12}$$

Thus, the effective coupling rate is with these transitions is $g_{\text{eff},k} = g_k J_1\left(\epsilon/2\nu_{\text{sb}}\right)$.

We perform universal operations on the multimode memory using the parametric operations described above between a given mode and both the $|g\rangle - |e\rangle$ and $|e\rangle - |f\rangle$ transmon transitions, with the latter allowing the realization of entangling gates between arbitrary eigenmodes. The minimal description of our gate operations on the multimode memory therefore involves three transmon levels, with the parametric control of the eigenmodes described by an extension of the Hamiltonian of Equation (3.11) to a single qutrit coupled

to the harmonic memory modes. In addition to sideband transitions, the Hamiltonian also includes dispersive shifts arising from photons in the memory modes, due to the bare coupling between the eigenmodes and the transmon. We ignore the correction to the dispersive shift due to the modulation amplitude dependence of the bare term ($\propto J_0(\epsilon/2\nu_{\rm sb})$), whose lowest order contribution is quadratic in $\epsilon/2\nu_{\rm sb}$. These effects are described by the following simplified Hamiltonian:

$$\begin{aligned}
\tilde{H}(t) &= \tilde{H}_{\rm sb} + \tilde{H}_{\rm q} + \tilde{H}_{\chi}, && (3.13)\\
\tilde{H}_{\rm sb} &= \sum_k \sum_{\alpha\in ge,ef} \left(g^{\alpha}_{eff,k}(t)\hat{b}^{\dagger}_k \hat{\sigma}^{-}_{\alpha} e^{2\pi i(\nu_{sb}-\Delta^{\alpha}_k)t} + \text{c.c.} \right), && (3.14)\\
\tilde{H}_{\rm q} &= \sum_{\alpha\in ge,ef} \left(\Omega^{\alpha}(t)\,\hat{\sigma}^{-}_{\alpha} + \text{c.c.} \right), && (3.15)\\
\tilde{H}_{\chi} &= \sum_k \left(\chi^{e}_k |e\rangle\langle e| + \chi^{f}_k |f\rangle\langle f| \right) \hat{b}^{\dagger}_k \hat{b}_k. && (3.16)
\end{aligned}$$

In the above, $\hat{\sigma}^{-}_{ge} = |g\rangle\langle e|$, $\hat{\sigma}^{-}_{ef} = |e\rangle\langle f|$ and $g^{\alpha}_{\text{eff},k}(t) = g^{\alpha}_k J_1\left(\frac{\epsilon^{\alpha}_k(t)}{2\nu_{\rm sb}}\right)$. $\epsilon^{\alpha}_k(t)$ for $\alpha \in \{ge, ef\}$ are the strengths of time-dependent parametric frequency modulation tones addressing mode k and $\Delta^{\alpha}_k = \nu_k - \bar{\nu}_{\alpha}$ is the detuning between mode k and the frequency of the corresponding transmon transition frequency $\alpha \in \{ge, ef\}$. $\Omega^{\alpha}(t)$ are the strengths of the transmon charge drives and $\chi^{e,f}_k$ are the dispersive shifts of the $|e\rangle$ and $|f\rangle$ levels resulting from the addition of a photon in mode k. In addition to the dispersive shift, there are second-order terms of the form $b^{\dagger}_l b_k$ for $l \neq k$ arising from the virtual hopping of photons between different eigenmodes via the transmon. These terms are of the same order as the dispersive shift, but their effect can be ignored since they correspond to off-resonant coupling ($\sim$ 1 MHz) between non-degenerate levels (spaced by $\sim$ 100 MHz). We note that there is also a shift (DC-offset) of the qubit frequency during the flux modulation, arising from the non-linear flux-frequency relation of the transmon. Given that only sequential flux pulses are used in

the experimental sequences in this work, we include their effect as:

$$\tilde{H}_{\mathrm{DC}} = \sum_{j;\beta\in\{e,f\}} \delta\nu_{\mathrm{DC}}^{j,\beta}\left(\epsilon_j^{\beta}(t)\right)|\beta\rangle\langle\beta|\,, \tag{3.17}$$

with additional cross terms being present if different flux tones were simultaneous. We can further simplify the Hamiltonian above by ignoring off-resonant terms. If the transmon charge and flux-modulation tones are of the form $\epsilon_{q,\mathrm{sb}}\cos\left(\omega_{q,\mathrm{sb}}t+\phi_{q,\mathrm{sb}}\right)$, and we consider near resonant operations with a single eigenmode k, the drive phases ($\phi_{q,\mathrm{sb}}$) enter the effective Hamiltonian as:

$$\tilde{H}_{\mathrm{sb},\alpha}(t) = g_{\mathrm{sb},\alpha}(t)\hat{a}_k^{\dagger}\hat{\sigma}_{\alpha}^{-}e^{-i\phi_{\mathrm{sb}}} + \mathrm{c.c.} \qquad \tilde{H}_{\mathrm{q}} = \Omega_{\alpha}(t)\hat{\sigma}_{\alpha}^{+}e^{-i\phi_q} + \mathrm{c.c.} \quad \alpha\in\{ge,ef\} \tag{3.18}$$

Reducing to 2×2 subspaces over which each of these terms act, and taking the top row to be the state with the higher transmon level, and with $\theta(t) = 2\Omega_{\alpha}t$ and $2g_{\mathrm{sb},\alpha}t$ for the sideband and qubit drives, we obtain:

$$\hat{H}_{\mathrm{sb},ge}(t) = \begin{pmatrix} 0 & g_{\mathrm{sb},ge}e^{i\phi_{\mathrm{sb}}} \\ g_{\mathrm{sb},ge}e^{-i\phi_{\mathrm{sb}}} & 0 \end{pmatrix} \tag{3.19}$$

$$\hat{U}_{\mathrm{sb},ge}^{\theta} = \begin{pmatrix} \cos\left(\frac{\theta}{2}\right) & -i\sin\left(\frac{\theta}{2}\right)e^{i\phi_{\mathrm{sb}}} \\ -i\sin\left(\frac{\theta}{2}\right)e^{-i\phi_{\mathrm{sb}}} & \cos\left(\frac{\theta}{2}\right) \end{pmatrix}, \tag{3.20}$$

$$\hat{H}_{\mathrm{q},ge}(t) = \begin{pmatrix} 0 & \Omega_{ge}e^{-i\phi_{\mathrm{q}}} \\ \Omega_{ge}e^{i\phi_{\mathrm{q}}} & 0 \end{pmatrix} \tag{3.21}$$

$$\hat{U}_{\mathrm{q},ge}^{\theta} = \begin{pmatrix} \cos\left(\frac{\theta}{2}\right) & -i\sin\left(\frac{\theta}{2}\right)e^{-i\phi_{\mathrm{q}}} \\ -i\sin\left(\frac{\theta}{2}\right)e^{i\phi_{\mathrm{q}}} & \cos\left(\frac{\theta}{2}\right) \end{pmatrix}. \tag{3.22}$$

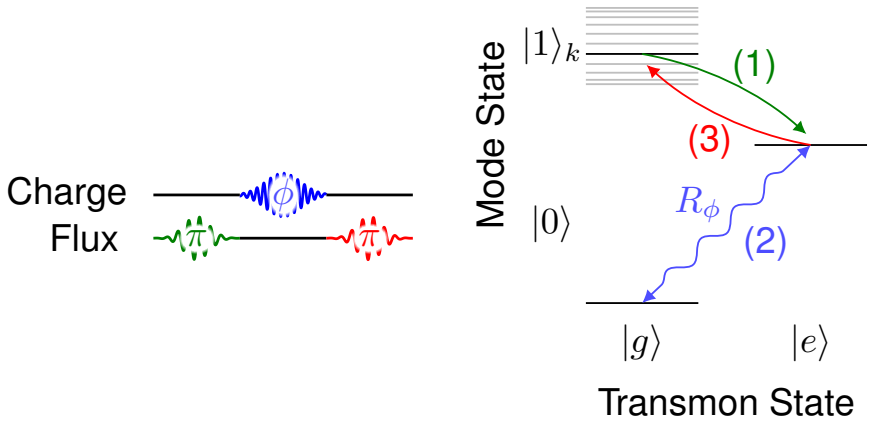

Figure 3.4: The sequence for generating arbitrary single-qubit gates of a memory mode: (1) The mode's initial state, consisting of a superposition of 0 and 1 photon Fock states, is swapped to the transmon (initially in its ground state), using a transmon-mode iSWAP. (2) The transmon is rotated by the desired amount (R_ϕ) via its charge control line. (3) The rotated state is swapped back to the mode, by reversing the iSWAP gate in (1). Segments of this sequence are used to achieve state preparation [steps (2) and (3)] and measurement [steps (1) and (2)] of each mode.

3.3 Universal gates on memory modes

The transmon-mode iSWAP and arbitrary rotations of the transmon state via its charge bias provide a toolbox for universal state preparation, manipulation, and measurement of each mode of the quantum memory. In Figure 3.4, we illustrate how to perform these operations.

To achieve universal control of the quantum memory, we extend our parametric protocols to realize two-mode gates. We perform conditional operations between the transmon and individual modes by utilizing the $|e\rangle - |f\rangle$ transition of the transmon. A controlled-phase (CZ) gate between the transmon and an individual mode consists of two sideband iSWAPs resonant to the $|e1\rangle - |f0\rangle$ transition, selectively mapping the state $|e1\rangle\, to\, -|e1\rangle$, leaving all other states unchanged due to the anharmonicity of the transmon. To enact a CZ gate between two arbitrary modes, the control mode is swapped into the transmon, a transmon-mode CZ is performed, and the mode is swapped back.

The level diagram describing the relevant multimode states and transitions involved in

Two-mode gate	Pulse Sequence
$\mathrm{CZ_{j,k}}$	$\pi^{ge}_{\mathrm{sb},j} + \pi^{ef}_{\mathrm{sb},k} + \pi^{ef}_{\mathrm{sb},k} + \pi^{ge}_{\mathrm{sb},j}(\phi = \pi)$
$\mathrm{CX_{j,k}}$	$\pi^{ge}_{\mathrm{sb},j} + \pi^{ef}_{\mathrm{sb},k} + \pi^{ef}_{\mathrm{q},y} + \pi^{ef}_{\mathrm{sb},k} + \pi^{ge}_{\mathrm{sb},j}(\phi = \pi)$
$\mathrm{CY_{j,k}}$	$\pi^{ge}_{\mathrm{sb},j} + \pi^{ef}_{\mathrm{sb},k} + \pi^{ef}_{\mathrm{q},x} + \pi^{ef}_{\mathrm{sb},k} + \pi^{ge}_{\mathrm{sb},j}(\phi = \pi)$
$\mathrm{SWAP_{j,k}}$	$\pi^{ge}_{\mathrm{sb},j} + \pi^{ef}_{\mathrm{sb},k} + \pi^{ge}_{\mathrm{sb},k} + \pi^{ef}_{\mathrm{sb},k} + \pi^{ge}_{\mathrm{sb},j}$

Table 3.1: Pulse sequences used for realizing various two-mode gates. j and k are indices corresponding to the control and target mode, respectively.

the CZ gate are shown in Figure 3.5. Control of the relative phases between these pulses allows for the correction of additional phase errors arising from the dispersive shift and the realization of an arbitrary controlled phase gate.

We obtain a CNOT gate by inserting an $|e\rangle - |f\rangle$ transmon charge π pulse (π^{ef}_{q}) between the two $|e\rangle - |f\rangle$ sideband iSWAP pulses. This allows for mapping the state $|e0\rangle$ to $|e1\rangle$ (and vice versa) via the state $|f0\rangle$ (qubit-mode CNOT), which again becomes a mode-mode CNOT gate when sandwiched with two $|g\rangle - |e\rangle$ sideband iSWAP pulses. The pulse sequence, energy level diagram, and relevant transitions for the CNOT gate are shown in Figure 3.5.

Slight modifications of these pulse sequences allow the realization of other two-mode gates such as the mode-mode CY and SWAP gates. The pulse sequences (without corrections from the dispersive shift) for realizing these two-mode gates are summarized in Table 3.1.

3.4 Constructing large entangled states

Parametric control of the quantum memory allows us to build maximally entangled states spanning several modes, using the protocol described in Figure 3.6. First, we create a superposition of the transmon ground and excited states. Next, we add a photon to the desired mode, conditioned on the transmon state. This is repeated for each mode in the entangled state. Finally, we disentangle the transmon from the memory modes, transferring the remaining population into the final mode.

This protocol illustrates the ease with which a random access quantum information pro-

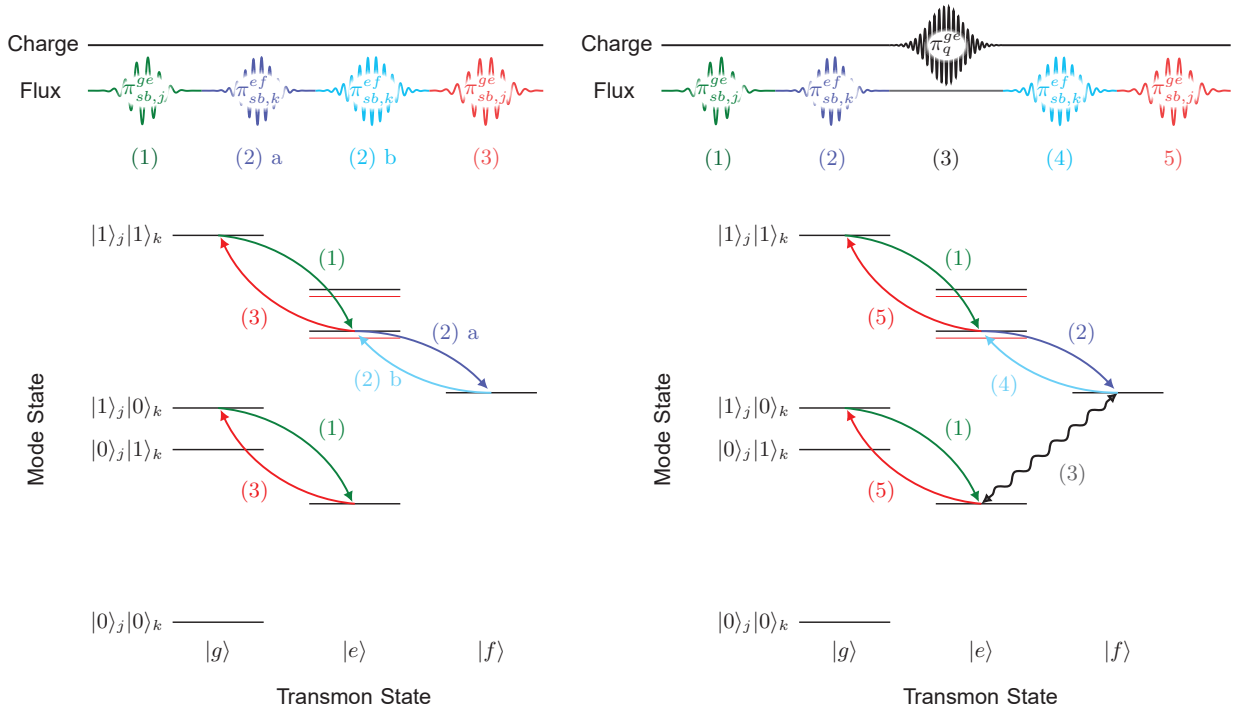

Figure 3.5: Protocol for controlled-phase (CZ) and controlled-NOT (CNOT) gates between an arbitrary pair of modes, with j indicating the control mode and k indicating the target mode of the gate. The CZ gate is performed as follows: (1) The state of mode j is swapped to the transmon via a transmon-mode iSWAP pulse at the frequency difference between the transmon $|g\rangle - |e\rangle$ transition and mode k. (2) A CZ gate is performed between mode k and the transmon, by applying two frequency-selective iSWAPs from energy level $|e1\rangle$ to level $|f0\rangle$ and back, mapping the state $|e1\rangle$ to $-|e1\rangle$. (3) The state of the transmon is swapped back to mode j, reversing the iSWAP in (1). A CNOT gate is realized by inserting an $|e\rangle - |f\rangle$ transmon charge π pulse (π_{q}^{ef}) between the two $|e\rangle - |f\rangle$ sideband iSWAP pulses. CY gates are realized by adjusting the phase of the π_{q}^{ef} pulse.

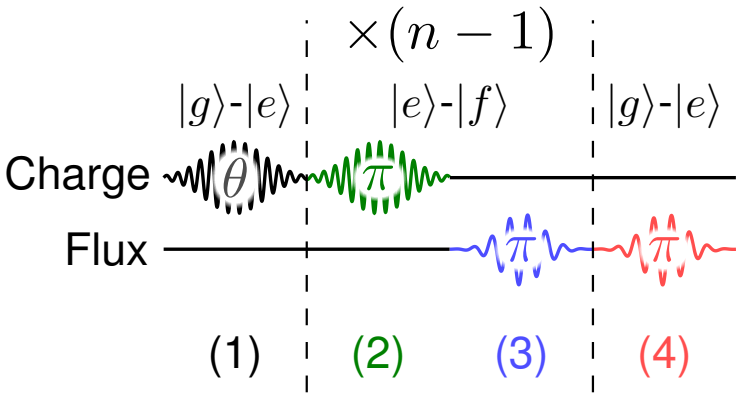

Figure 3.6: Pulse sequence for generating n-mode maximally-entangled states. Step (1) creates a superposition of the transmon $|g\rangle$ and $|e\rangle$ states, with the relative amplitudes of the superposition controlled by the rotation angle θ. Steps (2) and (3) load photons into modes of the memory, conditioned on the transmon state by utilizing the transmon $|f\rangle$ state. These steps are repeated $n-1$ times to entangle additional modes. Step (4) performs a $|g\rangle - |e\rangle$ iSWAP to the last mode, disentangling the transmon from the modes.

cessor can be used to generate multimode entangled states of arbitrary modes. Variants of this sequence can be used to create other classes of multimode entangled states, including W states, Dicke states [17] and cluster states [52]. Such states are valuable resources in several quantum error correction schemes and are useful for quantum optics and sensing [3].

CHAPTER 4

DESIGN, FABRICATION, AND CHARACTERIZATION OF A RANDOM ACCESS QUANTUM INFORMATION PROCESSOR

In this chapter, we present an implementation and characterization of the random access quantum information processor proposed in the previous chapter. First, we describe the design and fabrication of the transmon and the multimode memory, as well as the microwave setup used in the measurements. Then, we measure the transmon properties, including readout, coherence, and flux dependence. We demonstrate a fundamental tool used in control of this processor, the stimulated vacuum Rabi oscillation. We use these oscillations to characterize the fundamental properties of the multimode memory. We describe the subtleties in construction of a universal set of quantum gates using the oscillations and how to calibrate the pulses to account for these subtleties. After preparing the gates, we characterize them using randomized benchmarking and process tomography. Note that the content of this chapter is based on previously published work [46] with permission [13].

4.1 Processor design and fabrication

In this implementation, the multimode memory consists of the eigenmodes of an array of coplanar waveguide (CPW) resonators. The CPW resonators in the array have a center pin width of 12 μm and a gap width of 6 μm. They are coupled to each other via interdigitated capacitors, where each side of the capacitor has 6 digits that are 107 μm long, 6 μm wide, and spaced by 6 μm. The capacitor coupling the array to the qubit is identical to the intra-array capacitors to minimize disorder of the resonators in the array. The transmon is capacitively coupled to ground via CPW capacitors on either side of the SQuID, with a center pin width of 20 μm and gap of 10 μm. The SQuID is a 20 μm by 10 μm loop, with two square junctions that are 170 nm and 125 nm wide. The flux bias line 6 μm from the SQuID is dipolar, with 25 μm long and 2 μm wide wires on each end. The ground plane of the chip has an array of

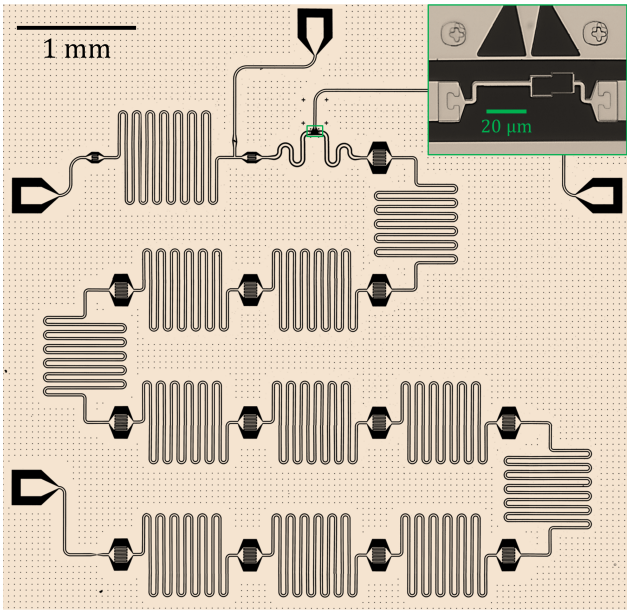

Figure 4.1: Optical image of the superconducting microwave circuit. The circuit comprises an array of 11 identically designed, co-planar waveguide (CPW) half-wave resonators, capacitively coupled strongly to each other. The top end of the array is capacitively coupled to a tunable transmon qubit. The transmon is measured with a separate CPW resonator, whose input line doubles as a charge bias for the transmon. The inset shows the tunable SQuID of the transmon, as well as its flux bias above it.

5 μm wide square holes spaced by 50 μm for flux vortex pinning [61]. The linear elements of the full circuit design have been simulated with a commercial 3D finite element analysis software (ANSYS HFSS).

The device (shown in Figure 4.1) was fabricated on a 430 μm thick C-plane sapphire substrate. The base layer of the device, which includes the majority of the circuit (excluding the Josephson junctions of the transmon), consists of 100 nm of aluminum deposited via electron-beam evaporation at 1 Å/s, with features defined via optical lithography and reactive ion etch (RIE) at wafer-scale. The wafer was then diced into 7x7 mm chips. The junction mask was defined via electron-beam lithography with a bi-layer resist (MMA-PMMA) in the Manhattan pattern, with overlap pads for direct galvanic contact to the optically defined capacitors. Before deposition, the overlap regions on the pre-deposited capacitors were milled *in-situ* with an argon ion mill to remove the native oxide. The junctions were then deposited with a three step electron-beam evaporation and oxidation process. First, an initial 35 nm

layer of aluminum was deposited at 1 Å/s at an angle of 29° relative to the normal of the substrate, parallel azimuthally to one of the fingers in the Manhattan pattern [24] for each of the junctions. Next, the junctions were exposed to 20 mBar of high-purity O_2 for 12 minutes for the first layer to grow a native oxide. Finally, a second 120 nm layer of aluminum was deposited at 1 Å/s at the same angle relative to the normal of the substrate, but orthogonal azimuthally to the first layer of aluminum. After evaporation, the remaining resist was removed via liftoff in N-Methyl-2-pyrrolidone (NMP) at 80°C for 3 hours, leaving only the junctions directly connected to the base layer, as seen in the inset of Figure 4.1. After both the evaporation and liftoff, the device was exposed to an ion-producing fan for 15 minutes, in order to avoid electrostatic discharge of the junctions.

4.2 Measurement setup and transmon characterization

The device is mounted and wirebonded to a multilayer copper PCB microwave-launcher board. Additional wirebonds connect separated portions of the ground plane to eliminate spurious differential modes. The device chip rests in a pocketed OFHC copper fixture that presses the chip against the launcher board. Notably, the fixture contains an additional air pocket below the chip to alter 3D cavity modes resulting from the chip and enclosure, shifting their resonance frequencies well above the relevant band by reducing the effective dielectric constant of the cavity volume.

The device is heat sunk via an OFHC copper post to the base stage of a Bluefors dilution refrigerator (10-30 mK). The sample is surrounded by a can containing two layers of μ-metal shielding, thermally anchored using an inner close fit copper shim sheet, attached to the copper can lid. The schematic of the cryogenic setup, control instrumentation, and the wiring of the device is shown in Figure 4.2. The device is connected to the rest of the setup through three ports: a charge port that applies qubit and readout drive tones, a flux port for shifting the qubit frequency using a DC-flux bias current and for applying RF sideband flux pulses, and an output port for measuring the transmission from the readout

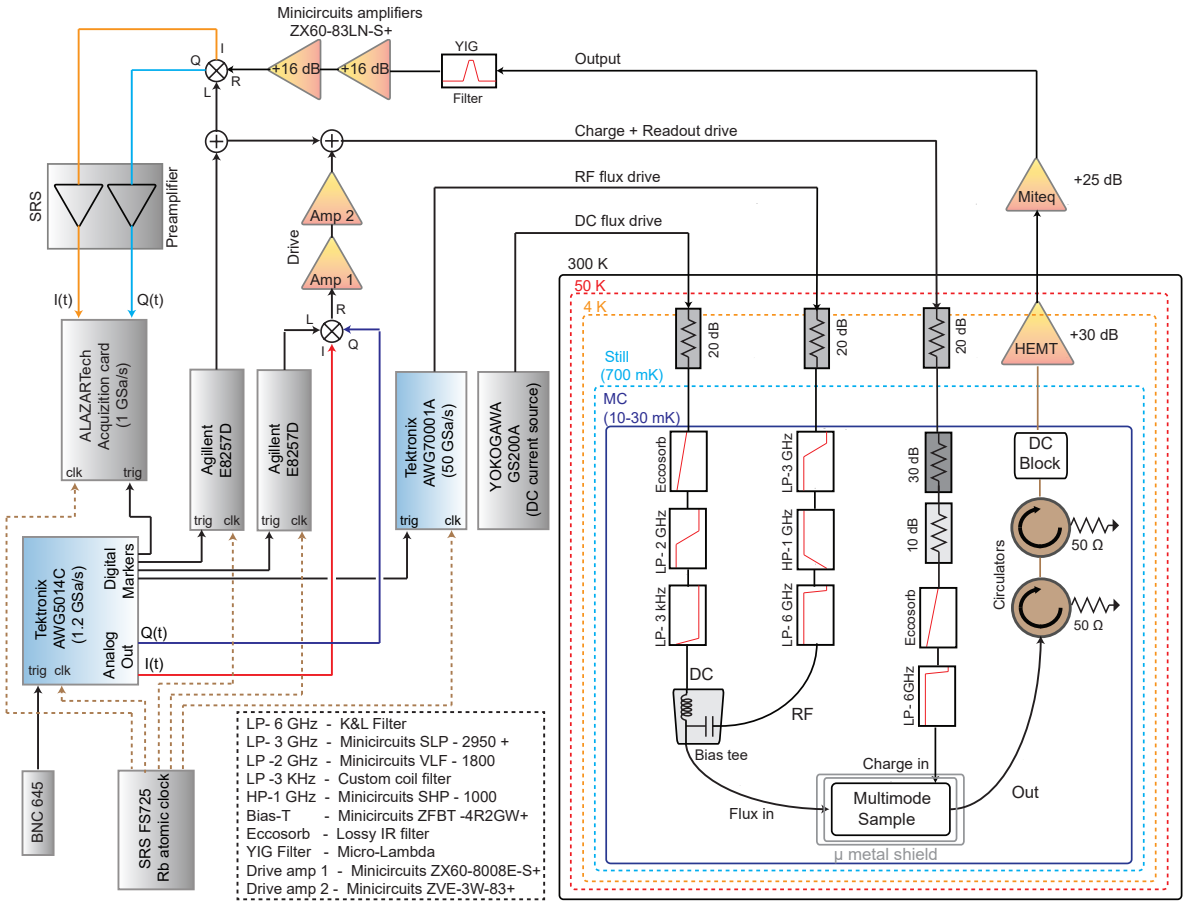

Figure 4.2: Schematic of the cryogenic setup, control instrumentation, and the wiring of microwave and DC connections to the device.

resonator. The charge pulses are generated by mixing a local oscillator tone (generated from an Agilent 8257D RF signal generator), with pulses generated by a Tektronix AWG5014C arbitrary waveform generator (TEK) with a sampling rate of 1.2 GSa/s, using an IQ-Mixer (MARQI MLIQ0218). The charge drive pulses are amplified at room temperature (30 dB), and subsequently combined with the readout drive pulse, generated from a second Agilent 8257D RF signal generator, which is also controlled by digital trigger pulses from the TEK. The combined signals are sent to the device, after being attenuated a total of 60 dB in the dilution fridge, using attenuators thermalized to the 4K (20 dB) and base stages (10 + 30 dB). The charge drive line also includes a lossy ECCOSORB CR-117 filter to block IR radiation, and a low-pass filter with a sharp roll-off at 6 GHz, both thermalized to the base stage. The flux-modulation pulses are directly synthesized by a Tektronix AWG70001A arbitrary waveform generator (50 GSa/s) and attenuated by 20 dB at the 4 K stage, and bandpass filtered to within a band of 400 MHz - 3 GHz at the base stage, using the filters indicated in the schematic. The DC flux bias current is generated by a YOKOGAWA GS200 low-noise current source, attenuated by 20 dB at the 4 K stage, and low-pass filtered down to a bandwidth of 3 kHz using a home built C-L-C π filter with a coil inductor (superconducting wire wound on a spool machined out of Vim Var core iron) and NPO capacitors. The DC flux bias current is combined with the flux-modulation pulses at a bias tee thermalized at the base stage. The state of the transmon is measured using the transmission of the readout resonator, through the dispersive circuit QED readout scheme [67]. The transmitted signal from the readout resonator is passed through a set of cryogenic circulators (thermalized at the base stage) and amplified using a HEMT amplifier (thermalized at the 4 K stage). Once out of the fridge, the signal is filtered (tunable narrow band YIG filter with a bandwidth of 80 MHz) and further amplified. The amplitude and phase of the resonator transmission signal are obtained through a homodyne measurement, with the transmitted signal demodulated using an IQ mixer and a local oscillator at the readout resonator frequency. The homodyne signal is amplified (SRS preamplifier) and recorded using a fast ADC card (ALAZARtech).

The parameters of the transmon are obtained by fitting the spectrum obtained as a function of the applied DC flux. The Josephson and electrostatic charging energies extracted from these fits are $E_{\mathrm{J,max}} = 22.2$ GHz and $E_{\mathrm{C}} = 192$ MHz, while the SQuID loop junction asymmetry, $(E_{\mathrm{J1}} - E_{\mathrm{J2}})/(E_{\mathrm{J1}} + E_{\mathrm{J2}}) = 0.1$. These parameters correspond to maximum and minimum qubit frequencies of 5.84 GHz and ~ 2 GHz, respectively. The experiments in this work were typically performed with the transmon biased between $3.9 - 4.7$ GHz (see Figure 4.3). This frequency band is ~ 2 GHz away from the eigenmodes of the resonator array. As a result, photons in the multimode manifold cause relatively small dispersive shifts of the transmon frequency. Additionally, the slope of the flux-frequency curve in this regime allows for sufficiently large frequency modulation amplitudes, while limiting sensitivity to flux noise to maintain transmon coherence. The transmon qubit state is probed using a capacitively coupled CPW readout resonator. The frequency and the quality factor of the readout resonator are $\nu_{\mathrm{read}} = 5.255$ GHz and $Q = 15000$, and the coupling to the qubit is $g_{\mathrm{read}} = 47$ MHz. For the typical transmon frequency range, we obtain single-shot readout fidelities between $0.3 - 0.85$ using dispersive [67] and high-power [55] circuit QED readout schemes. The readout signal is calibrated by appending a sequence with no pulse, and one with a transmon $|g\rangle - |e\rangle$ π pulse at the of each set of experimental sequences. Upon averaging over 1000-2000 experiments, the readout signal results in a visibility of $\sim 99\%$, limited by the fidelity of the single qubit gates as determined by randomized benchmarking (RB) (see section 4.4).

The coherence of the transmon is characterized by standard lifetime (T_1) and Ramsey (T_2^*) experiments. The measured T_1 of the $|e\rangle$ state and T_2^* of the $|g\rangle - |e\rangle$ transition are shown as a function of the $|g\rangle - |e\rangle$ transition frequency in Figure 4.3. The T_1 is found to show a slight decrease with increasing frequency in this regime, explained partially by increased Purcell loss from coupling to the readout resonator. The T_1 at a given flux bias slowly varies with time (over the course of weeks) by $\sim 25 - 30\%$. The T_2^* is found to increase with frequency, consistent with reduced sensitivity to flux noise due to the decreasing slope of the

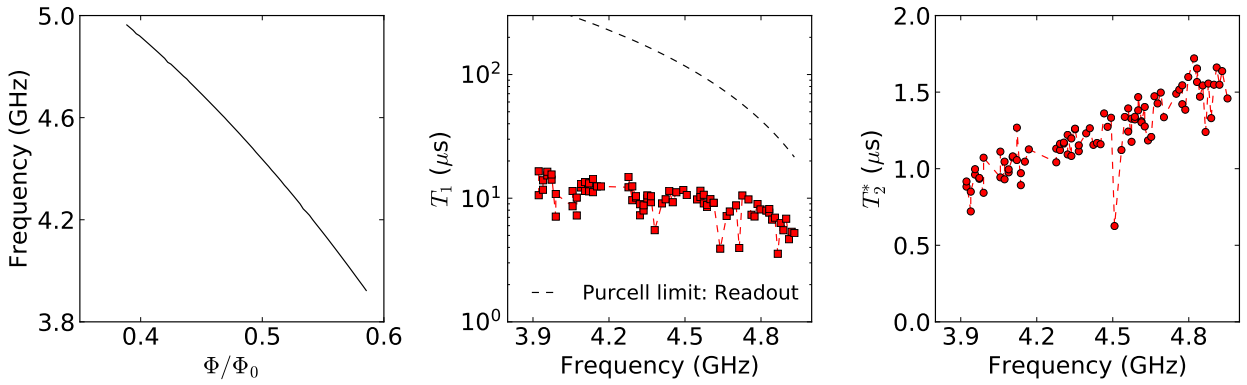

Figure 4.3: Flux dependence of the transmon frequency and coherence properties across this frequency range. On the left is the transmon frequency, ν_{q}^{ge}, as a function of applied DC flux bias in units of flux quanta, Φ_0. In the center are the energy relaxation times (T_1) as a function of transmon frequency, with the Purcell limit from the readout resonator shown for comparison. On the right are the Ramsey (T_2^*) coherence times as a function of transmon frequency.

frequency-flux curve transform. We note that T_2^* showed no improvement from reducing the cutoff frequency of the external cryogenic low-pass filter on the DC flux bias from 100 to 3 kHz. At $\nu_{\mathrm{q}} = 4.36$ GHz, the T_2 obtained from a spin-echo experiment with a single π pulse is 3.7 μs. This time could be increased to ~ 14 μs using a dynamical decoupling sequence (Carr-Purcell-Meiboom-Gill (CPMG) with 61 pulses) [6]. We note that the measured T_2^* jumped from 400 ns to 1.2 μs, 2-3 weeks following cooling the fridge to the base temperature (20 mK), coincident with a shift and stabilization of the applied current corresponding to a flux quantum. The coherence of the $|f\rangle$ level is characterized by analogous lifetime and Ramsey experiments, initializing the transmon in the excited state to begin with. The lifetime of the $|f\rangle$ level at $\nu_{\mathrm{q}}^{ge} = 4.3325$ GHz is $T_{1,ef} = 3.7$ μs while the phase coherence time is $T_{2,ef}^* = 1.2$ μs.

4.3 Stimulated vacuum Rabi oscillations and memory mode characterization

To illustrate the application of parametric control for addressing the multimode memory, we employ the experimental sequence shown in Figure 4.4. First, the transmon is excited via its charge bias. Subsequently, we modulate the flux to create sidebands of the transmon excited state at the modulation frequency. This is repeated for different flux pulse durations and frequencies, with the population of the transmon excited state measured at the end of each sequence. When the frequency matches the detuning between the transmon and a given eigenmode, we observe full-contrast stimulated vacuum Rabi oscillations. We see the resulting characteristic chevron patterns [63] as the modulation frequency approaches the detuning between the transmon and each of the modes. For long modulation times, the excited state population approaches zero. This is evident in the stimulated vacuum Rabi oscillation between the transmon and mode 6 shown in Figure 4.4. This indicates that the original photon is being exchanged between the transmon and the mode and no other photons are being pumped into the system. We achieve photon exchange between the transmon and individual modes in 20-100 ns, depending on the mode. This rate is limited by spectral crowding arising from neighboring modes and sideband transitions involving the transmon $|f\rangle$ level.

The rate of stimulated vacuum Rabi oscillations are related to the modulation strength and the bare coupling according to Equation (3.12). We can therefore extract the bare couplings from the measured sideband Rabi oscillation rates, particularly since the strength of the modulation can be independently calibrated from spectroscopy of the DC-offset of the transmon frequency, (see Figure 4.8).

Independently, we measure the eigenmode-state dependent dispersive shift of the transmon frequency. The shift for each mode k is measured with a transmon Ramsey interference experiment conducted after loading a photon into mode k, according to the protocol shown

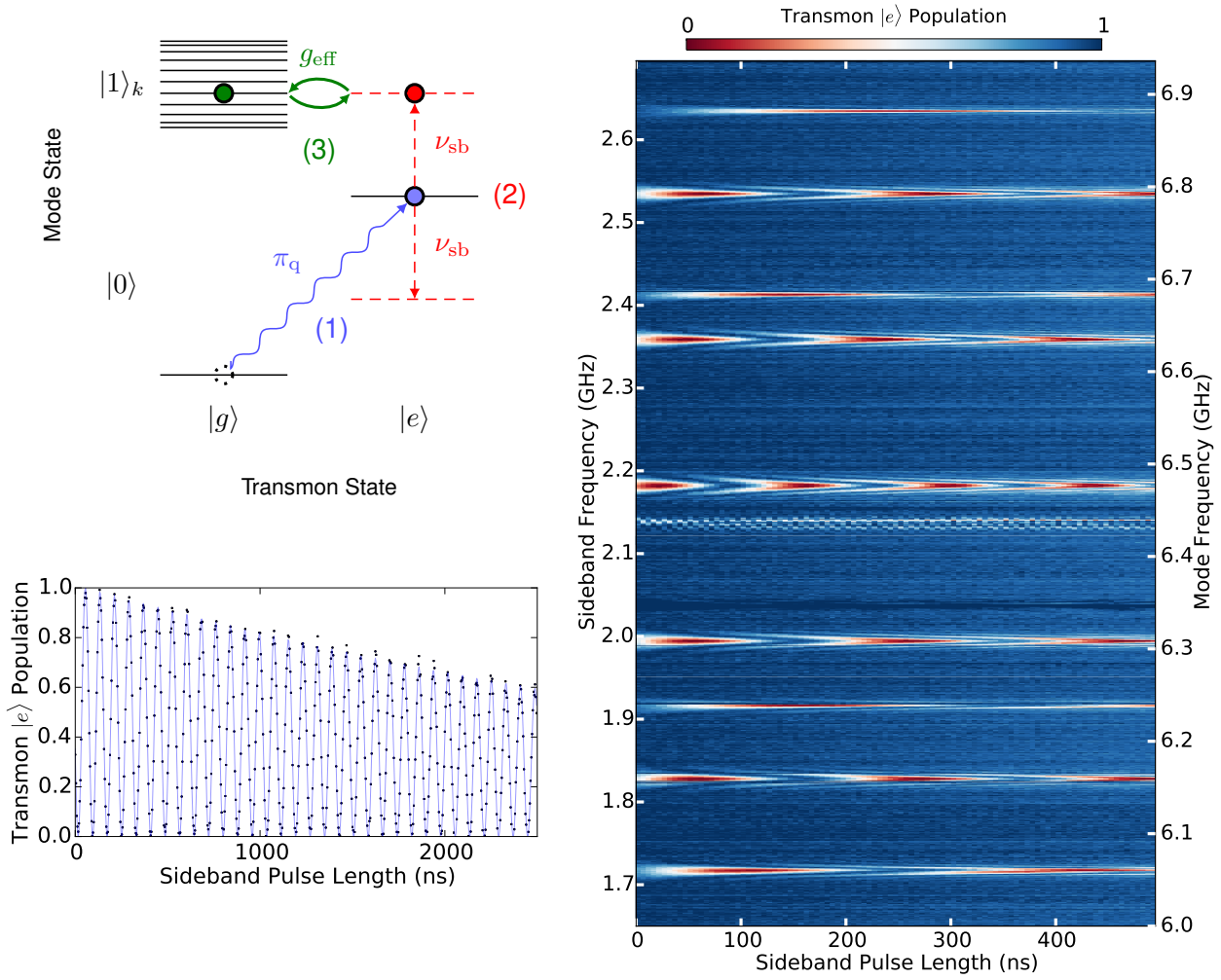

Figure 4.4: Generation of stimulated vacuum Rabi oscillations. $|1\rangle_k$ is the state with a single photon in mode k; all other modes are in the ground state. (1) An excitation is loaded into the transmon via its charge bias. (2) The transmon frequency is flux-modulated to create sidebands. (3) When a sideband is resonant with a mode, single-photon vacuum Rabi oscillations occur between transmon and the mode. Plotted on the right, experimental results obtained from this protocol for a range of sideband modulation frequencies, with the transmon biased at $\nu_{\rm q} = 4.28$ GHz. The length of the flux modulation pulse is swept for each frequency and the excited state population of the transmon is measured after the pulse ends. Chevron patterns indicate parametrically induced resonant oscillations with each of the memory modes. Two of the eleven modes are weakly coupled to the transmon and are not visible at these flux modulation amplitudes. The figure on the bottom left shows resonant oscillations between transmon and mode 6.

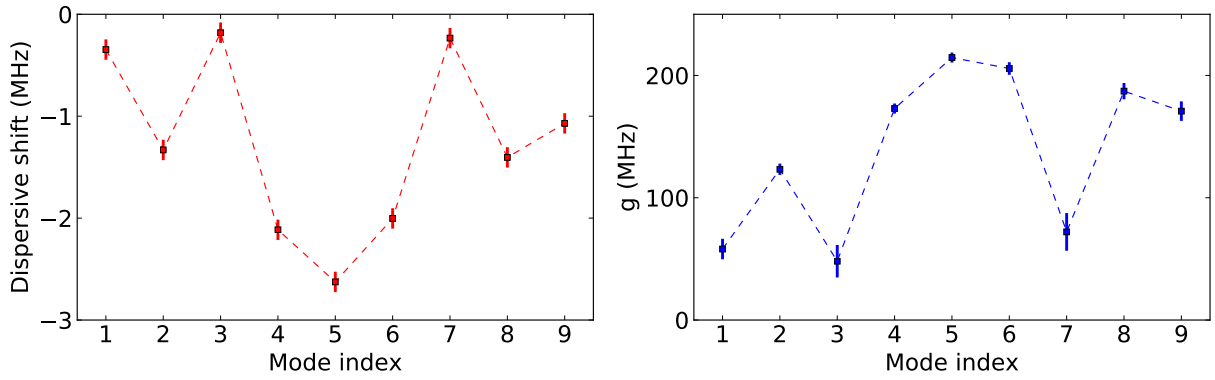

Figure 4.5: Dispersive shifts, χ_k, and corresponding transmon-mode couplings, g_k, as a function of mode index with the transmon biased at $\nu^{ge} = 4.3325$ GHz. The qubit frequency is stabilized to 50 kHz prior to each measurement and corresponds to the indicated error bar.

in Figure 4.5.

The dispersive shift is related to the measured oscillation frequency $\nu_{\mathrm{osc,k}}$ for each mode k and the Ramsey frequency ν_{Ram} according to $\chi_k = \nu_{\mathrm{osc}} - \nu_{\mathrm{Ram}}$, and is plotted as a function of mode number in Figure 4.5. We extract the coupling rate g_k from the measured dispersive shift χ_k, which are related by [33]:

$$\chi_k = \frac{g_k^2 \alpha}{\Delta_k(\Delta_k + \alpha)}, \tag{4.1}$$

where α is the transmon anharmonicity and $\Delta_k = \nu_q - \nu_k$ is the detuning between the transmon and mode k. The g_k's extracted from this expression are shown in Figure 4.5. The bare coupling rates extracted from the stimulated vacuum Rabi rate and from the dispersive shift are found to be consistent.

The resonance frequencies and coupling strengths measured are inconsistent with the values predicted from Equations (3.2) and (3.6), respectively. To explain these inconsistencies, we use Hamiltonian tomography [36] to extract the $2N - 1$ parameters of a chain of N nearest-neighbour coupled resonators. We assume the Hamiltonian for this chain is given by Equation (3.1), but allowing disorder of the individual resonator frequencies ($\nu_{\mathrm{r},i}$) and

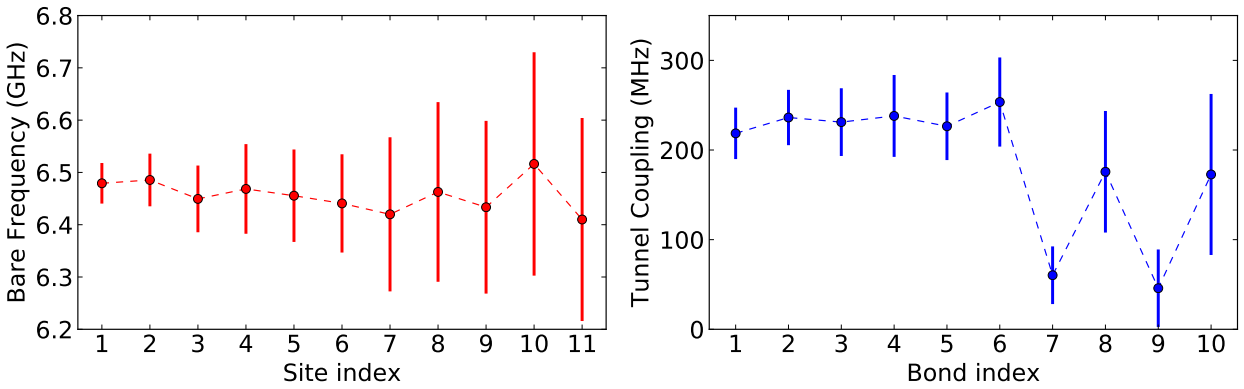

Figure 4.6: Bare resonator frequencies $\nu_{\mathrm{r},i}$ and nearest-neighbor tunnel couplings $g_{\mathrm{r},i}$ obtained from Hamiltonian tomography. The error bars in the bare frequencies and the couplings are obtained assuming a 25% uncertainty in the measured g_k's and a 0.5% uncertainty in the measured eigenfrequencies.

tunnel couplings ($g_{\mathrm{r},i}$):

$$\hat{H} = \sum_{i=1}^{N} \nu_{\mathrm{r},i} \hat{c}_i^\dagger \hat{c}_i + \sum_{i=1}^{N-1} g_{\mathrm{r},i} \left(\hat{c}_{i+1}^\dagger \hat{c}_i + \hat{c}_{i+1} \hat{c}_i^\dagger \right) \tag{4.2}$$

We extract these parameters using the frequencies (ν_k) and couplings to the transmon (g_k) of the eigenmodes of the array ($2N$ numbers). The coupling to the transmon is proportional to the amplitude of the memory-mode wavefunction at the edge resonator ($g_{\mathrm{eff},k} \propto |\phi_1^k|$), where the creation operator for eigenmode k is $\hat{b}_k^\dagger = \sum_i \phi_i^k \hat{c}_i^\dagger$. The bare frequencies and tunnel-couplings of the resonator are then extracted by iteratively solving the Schrödinger equation starting from the transmon end of the chain, while imposing the constraints from wavefunction normalization, $\sum_k \phi_i^k \left(\phi_j^k\right)^* = \delta_{ij}$, $\sum_i \phi_i^k \left(\phi_i^q\right)^* = \delta_{kq}$, as shown below:

$$\nu_{r,i} = \sum_k \nu_k \left| \phi_i^k \right|^2 \tag{4.3}$$

$$\phi_i^k = \frac{\left(\nu_k - \nu_{\mathrm{r},i-1}\right) \phi_{i-1}^k - g_{\mathrm{r},i-2} \phi_{i-2}^k}{g_{\mathrm{r},i-1}} \tag{4.4}$$

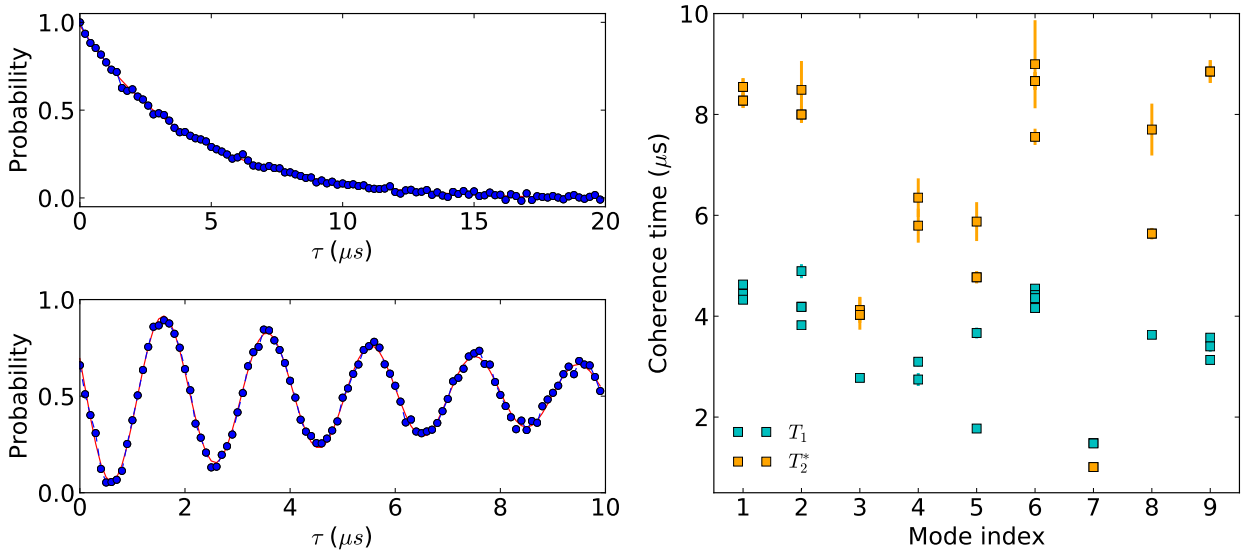

Figure 4.7: Coherence measurements of the memory modes. As an example, on the left are single-photon lifetime (T_1) and Ramsey coherence time (T_2^*) measurements on mode 1. The oscillation frequency of the Ramsey fringe can be used to infer the DC-shift of the transmon frequency during the iSWAP pulse. On the right is a summary of T_1 and T_2^* times for the modes in the multimode memory. The error bars for individual points are as extracted from the fits. Because of insufficient statistics, the figure includes all the coherence data obtained with the transmon biased at $\nu_\mathrm{q} \sim 4.59$ GHz.

$$g_{r,i}^2 = \sum_k \left(\nu_k - \nu_{\mathrm{r},i}\right)^2 \left|\phi_i^k\right|^2 - g_{\mathrm{r},i-1}^2. \tag{4.5}$$

The bare frequencies and tunnel couplings thus extracted are shown in Figure 4.6. We infer that two of the normal modes are extremely weakly coupled to the transmon because of couplers 7 and 9 being defective.

The coherence times of the memory modes are characterized through protocols analogous to those for the transmon, with the qubit pulses sandwiched with a pair of transmon-mode iSWAP pulses to transfer the quantum state between the transmon and the mode. The results of T_1 and T_2^* measurements are summarized in Figure 4.7. The T_2^* is not found to be $2T_1$ limited for many of the modes. Excess population of the transmon is a possible source of additional dephasing limiting T_2^* for those modes.

In addition to being used to characterize the memory mode properties, the stimulated

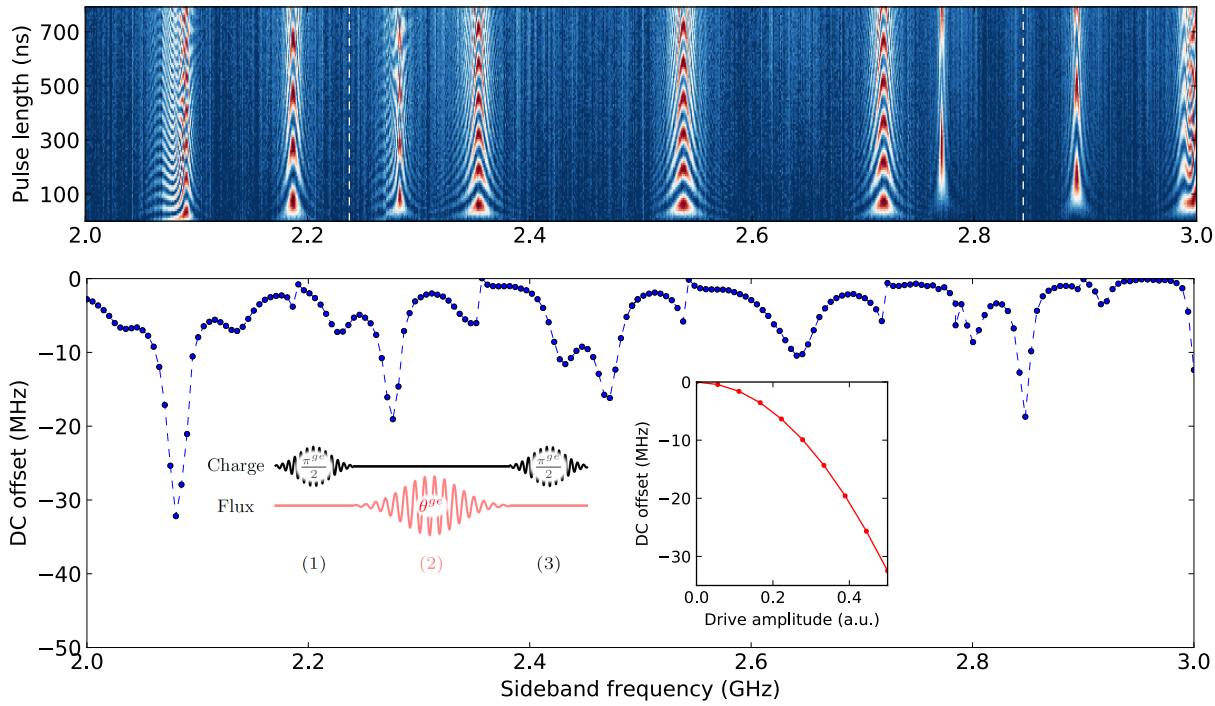

Figure 4.8: DC offset spectroscopy. On top is the pre-corrected stimulated vacuum Rabi spectrum on the $|g\rangle - |e\rangle$ transition with the transmon biased at $\nu^{ge} = 3.9225$ GHz, showing considerably more distortions than the corrected spectrum in Figure 4.4. On the bottom is the qubit DC-offset at a fixed drive amplitude as a function of sideband frequency measured using a transmon Ramsey experiment, shown as an inset, on the $|g\rangle - |e\rangle$ transition with a flux pulse inserted during the idle time. The plotted inset is the DC-offset as a function of drive amplitude for $\nu_{\text{sb}} = 2.63$ GHz, showing the expected quadratic dependence with drive amplitude.

vacuum Rabi spectrum can also be used to determine the transfer function of the flux control line and calibrate the flux-modulation amplitude as a function of frequency.

This calibration is done using the DC-shift of the qubit frequency during flux modulation. This frequency shift is measured using a transmon Ramsey interferometry experiment, with a flux pulse inserted during the idle time (Figure **??** inset). For a fixed external RF voltage amplitude, the measured DC-offset as a function of the flux-modulation frequency is shown in Figure **??**, along with the corresponding $|g\rangle - |e\rangle$ sideband spectrum. The stimulated vacuum Rabi chevrons for some modes are found to be distorted from the expected shape [63] (see mode 0 and 10). These distortions are due to resonances in the transmission profile of the

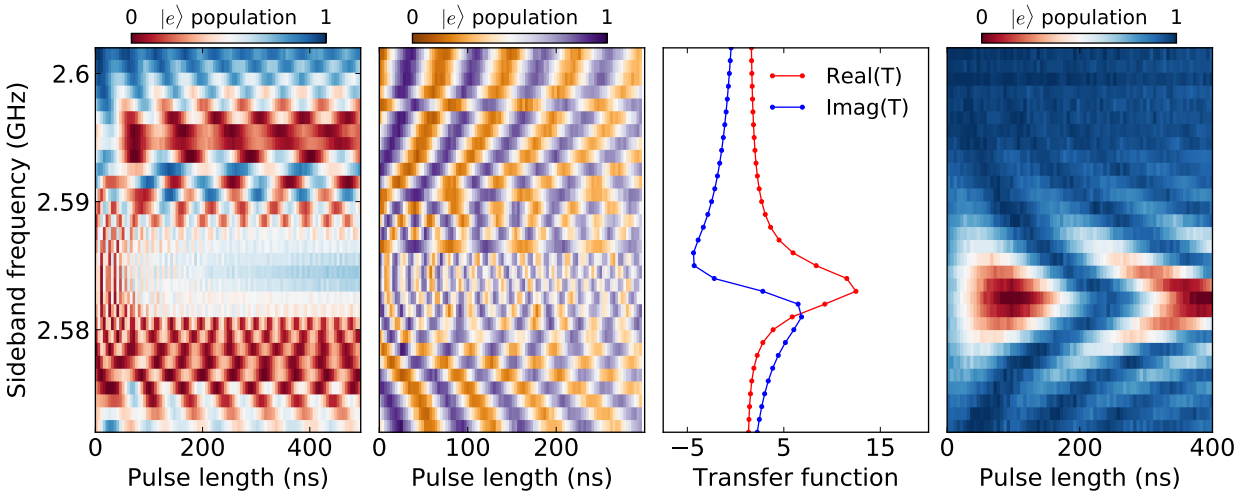

Figure 4.9: Correction of a stimulated vacuum Rabi chevron. On the left is the pre-corrected stimulated vacuum Rabi spectrum on the $|g\rangle - |e\rangle$ transition near mode 10 with the transmon biased at 4.3325 GHz. Next to that is the corresponding DC-offset calibration Ramsey experiment on the $|g\rangle - |f\rangle$ transition with a flux-pulse inserted during the idle time. This allows for a precise measurement of the line attenuation near the modes. The real and imaginary parts of the transfer function, obtained by fitting the experimentally measured transfer function amplitude to Equation (4.6), are plotted on the next graph. This form is automatically constrained to be causal, with the real and imaginary parts satisfying the Kramers-Kronig relations. Finally, on the right is the corrected spectrum, revealing a chevron pattern.

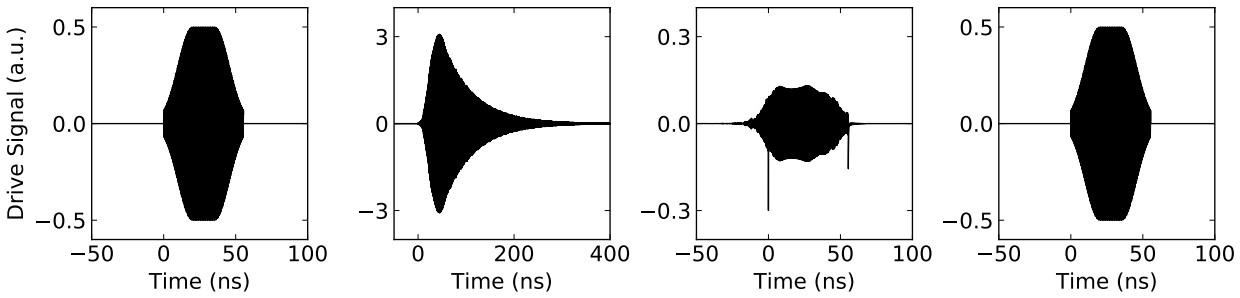

Figure 4.10: Correction process for a example distorted pulse. On the left is a ideal sideband pulse used perform a iSWAP between the transmon and mode 6. On the second graph, we plot the expected distorted pulse at the location of the sample based on the measured transfer function of the flux line. On third graph is the corrected AWG waveform calculated using Equation (4.7). Given this corrected input waveform, the final graph shows the expected pulse at the location of the sample due to distortion of the pulse through the flux line.

flux bias line, as seen in the DC-offset spectroscopy. The memory modes appear as avoided crossings in a Ramsey experiment on $|g\rangle - |e\rangle$ transition, due to interference of Ramsey fringes arising from the DC-offset and resonant stimulated vacuum Rabi oscillations. At a given frequency, the DC-offset shows a quadratic dependence on the modulation amplitude seen in Figure 4.8, as expected from Equation (3.8). The amplitude profile of the transfer function $T(\nu)$ of the flux bias line is obtained from the DC-offset at fixed AWG drive voltage, with $|T(\nu)| \propto \sqrt{|\delta\nu_{\mathrm{DC}}|}$.

For short pulse durations and large stimulated vacuum Rabi rates, the bandwidth of the pulse becomes commensurate with the frequency scale over which the transfer function of the flux bias varies significantly, causing distortion of the flux pulses. However, this effect is corrected using the knowledge of the transfer function of the flux bias. The complete complex transfer function (characterizing the amplitude and the phase of the flux bias distortion) is extracted only from the amplitude of the transfer function, by assuming that the response of the line is causal and enforcing the Kramers-Kronig relations [65]. We enforce these relations here by fitting the amplitude of the measured transfer function to the functional form:

$$|T(\nu)| = \left| y_0 + \sum_i \frac{A_i}{(\nu^2 - \nu_{0,i}^2) - i\gamma\nu} \right| . \tag{4.6}$$

We account for flux-pulse distortion by modifying the pulses generated by the AWG to account for the transfer function of the flux bias line. The AWG waveform used to generate a given pulse $f(t) = \mathrm{Re}[f_c(t)]$ at the location of the qubit is:

$$f_{\mathrm{AWG}}(t) = \mathrm{Re}\left[\mathrm{IFFT}\left(\frac{\mathrm{FFT}(f_c(t))}{T(\nu)}\right)\right] \ . \tag{4.7}$$

4.4 Single-mode gate calibration and characterization

We use stimulated vacuum Rabi oscillations to perform iSWAP gates between the transmon and memory modes. Combined with rotations of the transmon via its charge bias line, we can perform arbitrary single mode gates. The frequency of the iSWAP pulse acting on a particular mode is obtained by choosing the frequency corresponding to maximum contrast of the stimulated vacuum Rabi chevrons, such as those in Figure 4.4. The amplitude and pulse bandwidth of the flux-modulation pulses are optimized to maximize the oscillation rate, while minimizing cross talk with neighboring modes and sideband transitions across other transmon levels. The length of an iSWAP pulse is obtained using fits of stimulated vacuum Rabi oscillation. To achieve high fidelity gate operations, we also calibrate and correct phase errors arising during the sideband pulses.

The main phase error in the flux-modulation pulse is due to the DC-shift of the transmon frequency during flux-modulation ($\delta\nu_{\mathrm{DC}}$ in Equation (3.8)). The frequency of the center of the stimulated vacuum Rabi chevron is detuned from the difference frequency between the mode and the relevant transmon transition by $-\delta\nu_{\mathrm{DC}}$. Since the flux pulse frequency is set to the center of the chevron, the clock (rotating frame) of the applied drive is shifted from the frame of the Hamiltonian of equation 3.4. This results in an additional phase that accrues during that time. In the Ramsey experiment measuring the coherence time (T_2^*) of the modes (see Figure 4.7), the accrued phase shifts the frequency of the Ramsey fringes by $\delta\nu_{\mathrm{DC}}$. We can then account for the misalignment of clocks by advancing the phase of the subsequent pulse by $2\pi\delta\nu_{\mathrm{DC}}\tau$, where τ is the time between the pulses. This correction

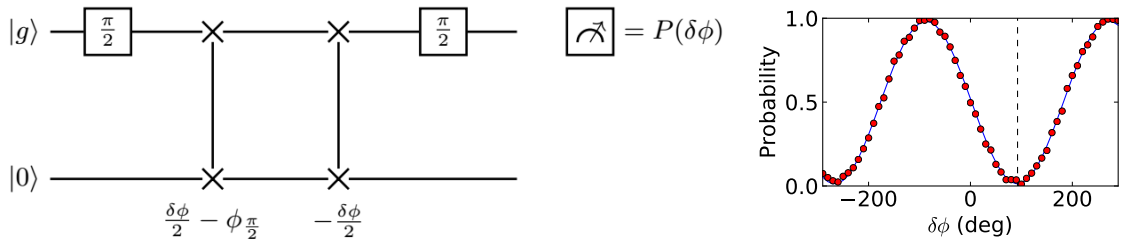

Figure 4.11: **a,** Circuit for calibrating phase of the iSWAP gate, where we sweep the phase $\frac{\delta\phi}{2}$ added and subtracted from the iSWAP pulses used to load and unload the state to the memory mode. We introduce an additional offset phase ($\phi_{\frac{\pi}{2}}$) which corrects σ_z errors occurring in the qubit pulse, ensuring that the mode state at the end of the first sideband pulse is free from all σ_z errors. The optimal phase for the iSWAP pulses is obtained by minimizing $P(\delta\phi)$. **b,** iSWAP phase calibration for mode 9 of the multimode memory, optimal phase ($92.5 \pm 0.1^\circ$) indicated by the black dashed line.

can be easily implemented by keeping the drive clock aligned with the bare qubit-resonator system when the flux pulse is off, and incrementing the drive frequency by $\delta\nu_{\mathrm{DC}}$ during the iSWAP pulse to bring it into resonance with the DC-shifted frame.

Fixing the drive clock to be in sync with the Hamiltonian of Equation (3.4) results in the absence of idle-time dependent phase errors. We additionally need to calibrate an additional dynamical phase (σ_z error) that occurs due to the change in the qubit frequency during the ramp up of the flux pulse. This phase is manifest in a rotating frame corresponding to the instantaneous qubit frequency $\bar{\nu}_{ge}(t)$ in equation (3.10). Repeating the transformation of equation (3.11) with a time-dependent qubit frequency results in an additional term:

$$\delta\hat{H} = -\frac{1}{2}h\frac{\partial\bar{\nu}_{ge}(t)}{\partial t}t\hat{\sigma}_z. \tag{4.8}$$

If we consider a square flux pulse with modulation amplitude corresponding to a DC-offset of ν_{DC} and pulse duration of t_π, the additional term in the Hamiltonian results in a dynamical phase of $\pi\nu_{\mathrm{DC}}t_\pi$. This error is calibrated using the sequence shown in Figure 4.11 and corrected by adjusting the relative iSWAP pulse phases. After calibrating the iSWAP phase ($\phi^{\pi-\pi}$), we add (subtract) $\frac{\phi^{\pi-\pi}}{2}$ to every iSWAP pulse for loading (unloading) an excitation into each of the memory modes. Subsequent $|g\rangle - |e\rangle$ iSWAP pulses in all circuit diagrams

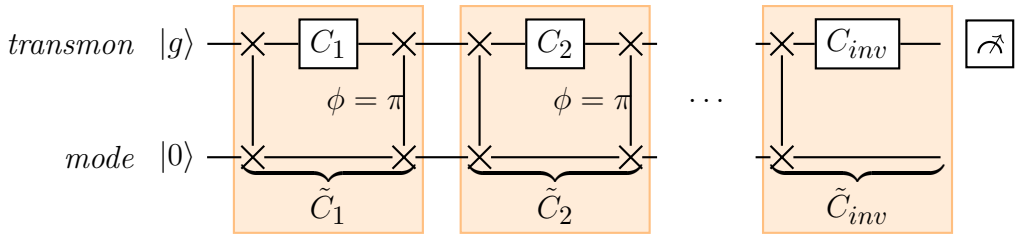

Figure 4.12: Randomized benchmarking (RB) characterizes the average random gate fidelity by acting randomly generated sequences of single-mode Clifford gates of increasing length, inverting the sequence, and then measuring the qubit state as a function of length. The sequence is applied to the multimode system initialized in the ground state, with the mode occupation error (ϵ) measured at the end of each sequence. The RB fidelity is extracted from the decay of the occupation fidelity ($1-\epsilon$) as a function of the length of the benchmarking sequence. For the data shown in Figure 4.13, we use sequence lengths corresponding to those in [32, 10] and average over 32 random sequences.

include this phase correction, and are represented by $\tilde{\pi}$ when represented in an equation.

To characterize the quality of our single-mode operations, we perform randomized benchmarking (RB) [32, 10]. We generate single-mode Clifford operations by sandwiching single-qubit Clifford rotations (C_i) of the transmon with transmon-mode iSWAPs.

$$\tilde{C}_i = U_{\tilde{\pi}_{\mathrm{sb}}} C_i U_{\tilde{\pi}_{\mathrm{sb}}(\phi=\pi)} = C_i$$

To map the state from mode to transmon and vice versa, we use iSWAP pulses that are 180° out of phase with each other, so that the mode Clifford operations are mapped directly from their transmon qubit counterparts. The Clifford operations are generated by concatenating an operator each from $\{0, \frac{\pi}{2}_y, \pi_y, -\frac{\pi}{2}_y\}$ and $\{0, \frac{\pi}{2}_x, \pi_x, -\frac{\pi}{2}_x, \frac{\pi}{2}_z, -\frac{\pi}{2}_z\}$, to generate all 24 elements of the single qubit Clifford group. The circuit showing the sequence used for RB of the modes is shown in Figure 4.12.

The RB fidelity (p) is extracted by fitting the decay curves to the form $Ap^m + B$, where m is the sequence length. We estimate the coherence limit to the RB fidelity to be:

$$p_i = p_q - 2\left(1 - \exp\left[-\frac{t^{\pi}_{\mathrm{sb},k}}{T_{1,k}}\right]\right), \tag{4.9}$$

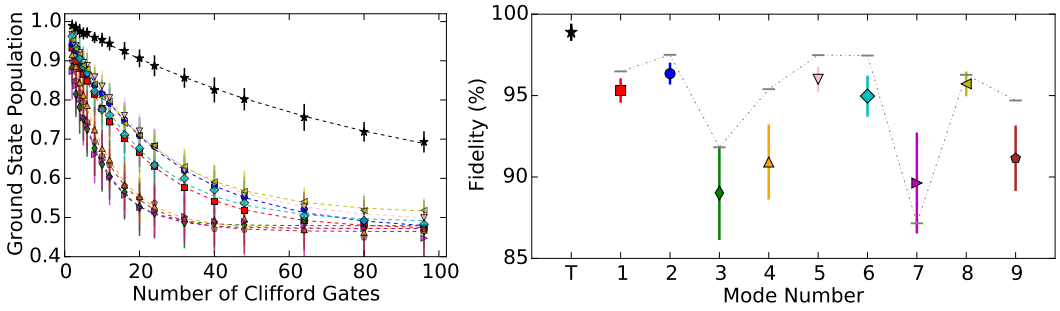

Figure 4.13: Single-mode randomized benchmarking. We apply sequences of varying numbers of consecutive Clifford gates, then invert each sequence with a unique Clifford gate. We measure the transmon ground-state population after inversion and average over 32 different random sequences, with the standard deviation (s.d.) plotted as error bars for each sequence length. From fitting the resulting data, we find single-mode gate fidelities from 89.0±2.9% to 96.3±0.7% and a transmon (T in the figure) gate fidelity of 98.9±1.3%. These are consistent with the expected coherence-limited fidelities, plotted as gray bars (s.d. from fit plotted as error bars.)

where $t^{\pi}_{sb,k}$ and $T_{1,k}$ are the iSWAP durations and lifetimes, respectively, of mode k, and p_q is the RB fidelity of the transmon.

We achieve RB fidelities ranging from 89.0±2.9% to 96.3±0.7%. These fidelities approach the expected coherence limit, indicated by the gray bars in the figure. The coherence limits are estimated based on the qubit RB fidelity, the iSWAP times ($20-100$ ns) and the coherence times ($T_1 = 1-5$ μs, $T_2^* = 1-8.5$ μs) of individual modes. Each single-mode gate consists of two transmon-mode iSWAPs, and a single transmon gate. From the error in the single-mode and transmon RB, we estimate the fidelities of the individual transmon-mode iSWAP operations to range from 95 to 98.6%.

4.5 Two-mode gate phase errors and calibration

The discussion in section 3.3 of two-mode gates only involved resonant first-order sideband transitions and ideal transmon charge drive pulses. This idealized description is corrected by additional terms in the Hamiltonian of Equation (3.13). The dominant additional effects are from: (1) dispersive shifts arising from photons in the multimode memory, (2) the qubit DC-offset due to flux modulation, and (3) phases from AC Stark shifts due to off-resonant first-

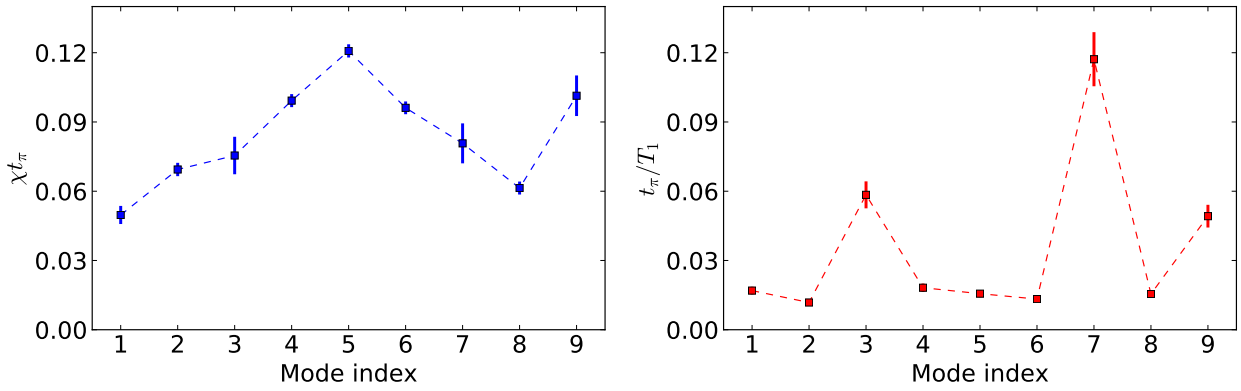

Figure 4.14: **a,** Error arising from the dispersive shift χ during an iSWAP pulse of duration t_π. The linear order phase errors ($\sim 25-60°$ over the course of a CZ gate) are corrected during the gate, leaving residual amplitude error ($\propto (\chi t_\pi)^2$). The error bar in χt_π is dominated by the error in the measurement of χ. **b,** Error arising from T_1 loss during a sideband, plotted for comparison to the dispersive shift error. The $T_1's$ are the mean of the data in Figure 4.7, with the error in $\frac{t_\pi}{T_1}$ extracted from a 10% uncertainty in the T_1 of each mode.

order sidebands. These shifts result in corrections to the transmon rotation and transmon-mode iSWAP unitaries.

For the case of the dispersive shift, the corrections to the target unitaries depend on the quantum state of the multimode memory and result in a transmon-mode ZZ error. If we ignore photons in the rest of the memory, the effect of the dispersive shift on ther modes involved in a two-mode entangling gate can be inferred from the energy level diagram of Figure 3.5. The dispersive shift causes the $|e10\rangle$ and $|e01\rangle$ levels to be shifted (red) from their bare values (black). As a result, sidebands resonant with $|e00\rangle \longleftrightarrow |g10\rangle$ are off-resonant from $|e01\rangle \longleftrightarrow |g11\rangle$.

The dispersive shift results in a phase and population error in the $|e01\rangle$ state. For the dispersive shifts χ and iSWAP times t_π used in this work, this population error is $\propto (\chi t_\pi)^2$ and, at worst, $\sim 5\%$ over the course of a CZ gate. This error is uncorrected and factors into the total gate error. The phase error, on the other hand, is $\propto (\chi t_\pi)$ and results in a more significant effect (see Figure 4.14a). Given that the $|e01\rangle$ state affected by the dispersive shift is selectively addressed by the $|e\rangle - |f\rangle$ sideband pulses used in the gate (Figure 3.5),

this phase error is calibrated and corrected by adjusting the relative phase between these pulses.

The state dependent phases arising in the gate can be calculated by considering the effective Hamiltonian of equation (3.16) in the 8×8 subspace of levels relevant for the gates and shown in Figure 3.5:

$$\tilde{H}(t) = \begin{pmatrix} 0 & 0 & 0 & 0 & \Omega_{ge}^* & 0 & 0 & 0 \\ 0 & 0 & 0 & 0 & g_{k,ge}^* & \Omega_{ge}^* & 0 & 0 \\ 0 & 0 & 0 & 0 & g_{j,ge}^* & 0 & \Omega_{ge}^* & 0 \\ 0 & 0 & 0 & 0 & 0 & g_{j,ge}^* & g_{k,ge}^* & 0 \\ \Omega_{ge} & g_{k,ge} & g_{j,ge} & 0 & 0 & 0 & 0 & \Omega_{ef}^* \\ 0 & \Omega_{ge} & 0 & g_{j,ge} & 0 & \delta_k & 0 & g_{k,ef}^* \\ 0 & 0 & \Omega_{ge} & g_{k,ge} & 0 & 0 & \delta_j & g_{j,ef}^* \\ 0 & 0 & 0 & 0 & \Omega_{ef} & g_{k,ef} & g_{j,ef} & 0 \end{pmatrix} \begin{matrix} |g\rangle \otimes |0_j 0_k\rangle \\ |g\rangle \otimes |0_j 1_k\rangle \\ |g\rangle \otimes |1_j 0_k\rangle \\ |g\rangle \otimes |1_j 1_k\rangle \\ |e\rangle \otimes |0_j 0_k\rangle \\ |e\rangle \otimes |0_j 1_k\rangle \\ |e\rangle \otimes |1_j 0_k\rangle \\ |f\rangle \otimes |0_j 0_k\rangle \end{matrix} \tag{4.10}$$

Here, the multimode state is labeled $|n_j, n_k\rangle$ and the phases of equation (3.18) have been absorbed into the g's and Ω's (which are time dependent), i.e.,

$$g_{i,\alpha} \to g_{i,\alpha} e^{i\phi_{\mathrm{sb},\alpha}} \quad , \quad \Omega_\alpha \to \Omega_\alpha e^{-i\phi_{\mathrm{q},\alpha}} \quad , \quad \alpha \in \{ge, ef\} \quad , \quad i \in \{j, k\}\,. \tag{4.11}$$

The $|e\rangle - |f\rangle$ sideband pulses act only on one transition and are unaffected by the state dependent shift when considering only two modes. We chose the $|e\rangle - |f\rangle$ sideband frequency to be resonant with the $|f00\rangle$ and the dispersively shifted $|e01\rangle$ level. In the rotating frame of equation (4.10), this corresponds to $|e\rangle - |f\rangle$ first-order sidebands acquiring the following time-dependence:

$$g_{j,ef}(t) = \tilde{g}_{j,ef} e^{-2\pi i \delta_k t} \quad , \quad g_{k,ef}(t) = \tilde{g}_{k,ef} e^{-2\pi i \delta_j t}. \tag{4.12}$$

$\tilde{g}_{i,ef}$ is proportional to the envelope of the $|e\rangle - |f\rangle$ sideband pulse, and δ_k and δ_j are the

Gate	Pulse Sequence
CZ	$\tilde{\pi}^{ge}_{\mathrm{sb},j}(\phi_\mathrm{a}) + \tilde{\pi}^{ef}_{\mathrm{sb},k}(\phi_\mathrm{b}) + \tilde{\pi}^{ef}_{sb,k}(\phi_\mathrm{c}) + \tilde{\pi}^{ge}_{\mathrm{sb},j}(\phi_\mathrm{d})$
CNOT	$\tilde{\pi}^{ge}_{\mathrm{sb},j}(\phi_\mathrm{a}) + \tilde{\pi}^{ef}_{\mathrm{sb},k}(\phi_\mathrm{b}) + \pi^{ef}_{q}(\phi_\mathrm{e}) + \tilde{\pi}^{ef}_{\mathrm{sb},k}(\phi_\mathrm{c}) + \tilde{\pi}^{ge}_{\mathrm{sb},j}(\phi_\mathrm{d})$

Table 4.1: Nomenclature for the pulse phases used in the CZ and CNOT gates resulting in the unitary operators in equation (4.14).

dispersive shifts of $\left|e0_j1_k\right\rangle$ and $\left|e1_j0_k\right\rangle$ respectively.

We compute the action of the CZ and CNOT gate sequences by evolving the Hamiltonian above, with time dependent coefficients and phases as per Table 4.1. In these pulse sequences, only one of the drive terms is on at any given time and the corresponding unitaries obtained upon integration of the Schrödinger equation are generalizations of those in Equation (3.22), with corrections arising from the dispersive shift. The effective unitary thus realized for the CZ and CNOT gates, to lowest order in χ/g_{sb} and χ/Ω are;

$$\mathrm{U_{CZ}} = \begin{pmatrix} 1 & 0 & 0 & 0 \\ 0 & 1 & 0 & 0 \\ 0 & 0 & -e^{i(\phi_\mathrm{a}-\phi_\mathrm{d})} & 0 \\ 0 & 0 & 0 & e^{i\left(\phi_\mathrm{a}-\phi_\mathrm{d}+\phi_\mathrm{b}-\phi_\mathrm{c}-2\pi t^{\pi}_{\mathrm{sb},j,ge}\delta_k\right)} \end{pmatrix} \tag{4.13}$$

$$\mathrm{U_{CNOT}} = \begin{pmatrix} 1 & 0 & 0 & 0 \\ 0 & 1 & 0 & 0 \\ 0 & 0 & 0 & e^{i\left(\phi_\mathrm{a}-\phi_\mathrm{d}+\phi_\mathrm{b}+\phi_\mathrm{e}-\pi t^{\pi}_{\mathrm{sb},j,ge}\delta_k\right)} \\ 0 & 0 & e^{i\left(\phi_\mathrm{a}-\phi_\mathrm{d}-\phi_\mathrm{c}-\phi_\mathrm{e}-\pi t^{\pi}_{\mathrm{sb},j,ge}\delta_k\right)} & 0 \end{pmatrix} \tag{4.14}$$

We see that one can choose sideband pulse phases that cancel phases arising from the dispersive shift and thereby realize the target unitaries for the CZ and CNOT gates.

Here, we describe protocols used to calibrate and correct each of the additional phases arising in the CZ gate. The phases of the iSWAP pulses used in the CZ gate are defined

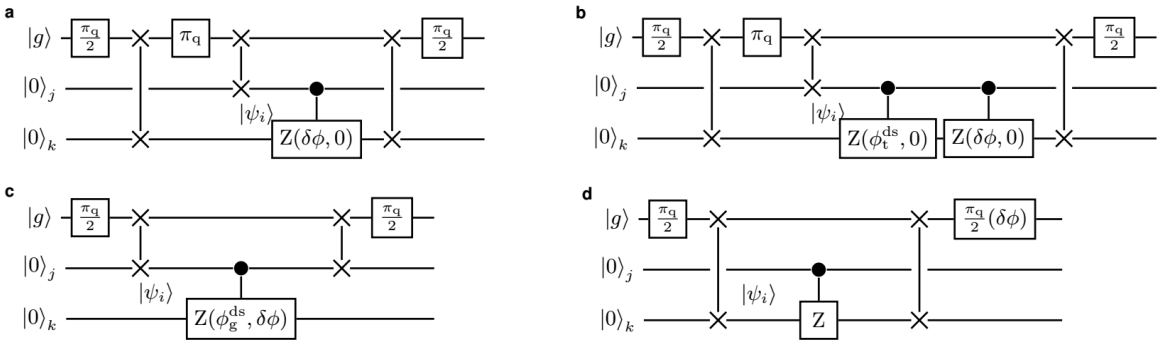

Figure 4.15: CZ gate calibration sequences. **a,** Measures phase error from the dispersive shift arising from the entire sequence. **b,** Isolates the error from the dispersive shift error occuring only during the gate. **c,** Measures the phase error arising from the qubit dc-offset occuring during the gate. **d,** Phase error arising from the AC Stark shift due to off-resonant first order sidebands.

below, where $\phi_{1,2}$ are the controlled phases:

$$\mathrm{CZ}_{j,k}(\phi_1, \phi_2) = \tilde{\pi}^{ge}_{\mathrm{sb},j} + \pi^{ef}_{\mathrm{sb},k}(\phi_1) + \pi^{ef}_{\mathrm{sb},k}(0) + \tilde{\pi}^{ge}_{\mathrm{sb},j}(\phi_2). \tag{4.15}$$

j is the control mode and k is the target mode of the CZ gate, with the states labeled $\left|n_j, n_k\right\rangle$, and $\tilde{\pi}$ indicating iSWAP pulses for which the DC-offset σ_z error is corrected within the pulse. From equation (4.13), we see that only two relative phase adjustments ($\phi_\mathrm{a} - \phi_\mathrm{d}$ and $\phi_\mathrm{b} - \phi_\mathrm{c}$) are required to correct the dispersive shift error. Here, we adjust these relative phases by controlling $\phi_1 = \phi_\mathrm{b}$ and $\phi_1 = \phi_\mathrm{d}$, while leaving ϕ_a and ϕ_c fixed. We measure each phase error through Ramsey experiments with initial states that are appropriate superpositions of the basis states, as indicated in Table 4.2.

Sequence	Phase error	Initial state	# CZ's	Measured mode
a	Dispersive shift (SPAM)	$\|10\rangle + \|11\rangle$	1	Target (k)
b	Dispersive shift (Gate)	$\|10\rangle + \|11\rangle$	2	Target (k)
c	DC-offset during gate	$\|01\rangle + \|11\rangle$	1	Control (j)
d	Off-resonant sidebands	$\|00\rangle + \|01\rangle$	1	Target (k)

Table 4.2: Summary of CZ gate phase calibration experiments that correct for each of the sources of the phase errors. The initial states used to calibrate each of the phase errors are indicated.

The phase error from the dispersive shift is obtained by preparing the system in the state $\left|\psi_p\right\rangle = |10\rangle + |11\rangle$. We measure the relative phase between the basis states after applying the CZ gate, using the sequence in Figure 4.15a. The dispersive shift results in the state $|11\rangle$ acquiring an additional phase in the preparation (ϕ_{p}), gate (ϕ_{g}) and measurement segments (ϕ_{m}). Similar additional phase errors accrue during the gate (ϕ_{g}) and the measurement (ϕ_{m}) segments. We sweep the phase ($\delta\phi$) of the first $|e\rangle - |f\rangle$ sideband pulse of the CZ gate (see Equation (4.15)). The phase that *maximizes* the final measured transmon population provides the total added phase, $\phi_{\mathrm{t}}^{\mathrm{ds}} = \phi_{\mathrm{p}} + \phi_{\mathrm{g}} + \phi_{\mathrm{m}}$. $\mathrm{CZ}_{j,k}(\phi_{\mathrm{t}}^{\mathrm{ds}}, 0)$ is a combination of an ideal CZ gate and the Cϕ (a controlled-phase gate with conditional phase ϕ) gate that cancels additional phases arising from the dispersive shift over the entire sequence.

We isolate the state-dependent phase error arising only during the CZ gate by adding a second Cϕ gate to the previous sequence, as shown in Figure 4.15b. We sweep the phase ($\delta\phi$) of the (first) $|e\rangle - |f\rangle$ sideband pulse of the second Cϕ gate, with $\phi_1 = \phi_{\mathrm{ds}}^{\mathrm{t}}$ for the first Cϕ gate. Given the same preparation and measurement sequences, the state preparation and measurement (SPAM) phases are corrected by construction by the first Cϕ gate. We find the phase $\delta\phi$ that *minimizes* the population of the transmon, thus realizing a CZ gate that flips the sign of the $|11\rangle$ state. The $\mathrm{CZ}_{k,j}(\phi_{\mathrm{g}}, 0)$ gate therefore is corrected for phases from dispersive shifts occurring during the gate sequence.

We obtain a fully corrected CZ gate by correcting the relative phase between the $\{|00\rangle, |01\rangle\}$ and $\{|10\rangle, |11\rangle\}$ manifolds. These state manifolds have a relative phase resulting from the transmon frequency DC-offset occurring during the $|e\rangle - |f\rangle$ sidebands of the CZ gate. We correct this additional phase by adjusting the phase of the final $|g\rangle - |e\rangle$ sideband pulse of the CZ gate (ϕ_2 in equation (4.15)), using the experimental sequence of Figure 4.15c. The resulting $\mathrm{CZ_{j,k}}(\phi_{\mathrm{g}}^{\mathrm{ds}}, \phi^{\mathrm{DC}})$ gate is therefore corrected of errors from dispersive shifts and qubit flux-modulation DC-offsets.

The phase error resulting from dispersive shifts due to off-resonant first-order sidebands are measured by acting the CZ gate on the $|00\rangle + |01\rangle$ state. The CZ gate nominally does not

change this state, and we correct this phase error using subsequent qubit pulses as shown in Figure 4.15d. This phase is significant only for gates between modes with spectral spacing near the anharmonicity of the transmon.

4.6 State and process tomography

After calibrating the gate, we measured its fidelity using quantum process tomography. Process tomography of a two-qubit gate consists of quantum state tomography after acting the gate on a set of 16 linearly independent input states that form a basis for representing an arbitrary two-qubit density matrix [49]. Here, we begin by describing how to perform state tomography on this system.

Reconstructing the density matrix of an arbitrary two-qubit state requires the measurement of all possible two-qubit correlations $\{\langle \mathrm{XI}\rangle, \langle \mathrm{XX}\rangle \ldots \langle \mathrm{ZZ}\rangle\}$, i.e.;

$$C_{i,j} = \langle B_i \otimes B_j \rangle \;\; | \;\; B_i \in \{\mathrm{I}, \mathrm{X}, \mathrm{Y}, \mathrm{Z}\} \tag{4.16}$$

An arbitrary correlator comprises products of Pauli operators applied to each of the memory bits, and corresponds to a generalized parity measurement. This is exactly the back-action on the phase measurement of a transmon while serving as the control of a CZ (CX) gate targeting a memory mode [20]. The value of an arbitrary correlator can thus be measured by performing Ramsey interferometry of the transmon with a series of CZ (CX) gates applied to the desired memory modes. We equivalently measure all the necessary correlations with the aid of the single and two-mode gate operations prior to measuring the state of the transmon. A sideband iSWAP pulse (π_{sb}) on the $|g\rangle - |e\rangle$ transition, along with single qubit rotations alone can be used to measure all single-mode correlators $C_{ij} \in \{\langle B_i \otimes I\rangle$ or $\langle I \otimes B_i\rangle\} \mid B_i \in \{\mathrm{X}, \mathrm{Y}, \mathrm{Z}\}$.

The entanglement information is present in two-mode correlators, $C_{i,j} = \langle \mathrm{B_i} \otimes \mathrm{B_j}\rangle \mid \mathrm{B_i} \in \{\mathrm{X}, \mathrm{Y}, \mathrm{Z}\}$. We measure these correlators by acting two-mode gates before measuring a single-

mode correlators. For instance, the $\langle XX \rangle$ correlator of a given state ($|\psi_i\rangle$) is measured by acting CX gate prior to the measurement of $\langle \mathrm{XI} \rangle$. In the Heisenberg picture [25], the transformation is shown below:

$$C = \langle \psi_f | \, X \otimes I \, | \psi_f \rangle = \langle \psi_i | \, U_{\mathrm{CX}}^{\dagger} \, (X \otimes I) \, U_{\mathrm{CX}} \, | \psi_i \rangle = \langle \psi_i | \, X \otimes X \, | \psi_i \rangle \tag{4.17}$$

Here $|\psi_i\rangle$ is the two-mode state to be measured and $|\psi_f\rangle = U_{\mathrm{CX}} \, |\psi_f\rangle$ is the state obtained following action of the CX gate. A summary of pulse sequences used for the measurement of each of the correlations required for two-mode tomography is shown in Table 4.3.

#	Measured Correlation	Pulse Sequence
0	$-\langle \mathrm{IX} \rangle$	$\pi_{\mathrm{sb},k} + \frac{\pi}{2}_y$
1	$\langle \mathrm{IY} \rangle$	$\pi_{\mathrm{sb},k} + \frac{\pi}{2}_x$
2	$\langle \mathrm{IZ} \rangle$	$\pi_{\mathrm{sb},k}$
3	$-\langle \mathrm{XI} \rangle$	$\pi_{\mathrm{sb},j} + \frac{\pi}{2}_y$
4	$-\langle \mathrm{XX} \rangle$	$\mathrm{CX} + \pi_{\mathrm{sb},j} + \frac{\pi}{2}_y$
5	$-\langle \mathrm{XY} \rangle$	$\mathrm{CY} + \pi_{\mathrm{sb},j} + \frac{\pi}{2}_y$
6	$\langle \mathrm{XZ} \rangle$	$\mathrm{CZ} + \pi_{\mathrm{sb},j} + \frac{\pi}{2}_y$
7	$\langle \mathrm{YI} \rangle$	$\pi_{\mathrm{sb},j} + \frac{\pi}{2}_y$
8	$\langle \mathrm{YX} \rangle$	$\mathrm{CX} + \pi_{\mathrm{sb},j} + \frac{\pi}{2}_x$
9	$\langle \mathrm{YY} \rangle$	$\mathrm{CY} + \pi_{\mathrm{sb},j} + \frac{\pi}{2}_x$
10	$-\langle \mathrm{YZ} \rangle$	$\mathrm{CZ} + \pi_{\mathrm{sb},j} + \frac{\pi}{2}_x$
11	$\langle \mathrm{ZI} \rangle$	$\pi_{\mathrm{sb},1}$
12	$-\langle \mathrm{ZX} \rangle$	$\mathrm{CZ} + \pi_{\mathrm{sb},k} + \frac{\pi}{2}_y$
13	$\langle \mathrm{ZY} \rangle$	$\mathrm{CZ} + \pi_{\mathrm{sb},k} + \frac{\pi}{2}_x$
14	$\langle \mathrm{ZZ} \rangle$	$\mathrm{CX} + \pi_{\mathrm{sb},k}$

Table 4.3: Pulse sequences used for the measurement of all two-qubit correlations between mode pairs. These correlations are used to reconstruct a two-qubit density matrix using equation 4.19.

We extract the correlators and construct the density matrix of the two-mode state from the measured transmon population P_{ij} at the end of the sequence for each correlator C_{ij} using;

$$C_{i,j} = \langle B_i \otimes B_j \rangle = 2P_{ij} - 1, \tag{4.18}$$

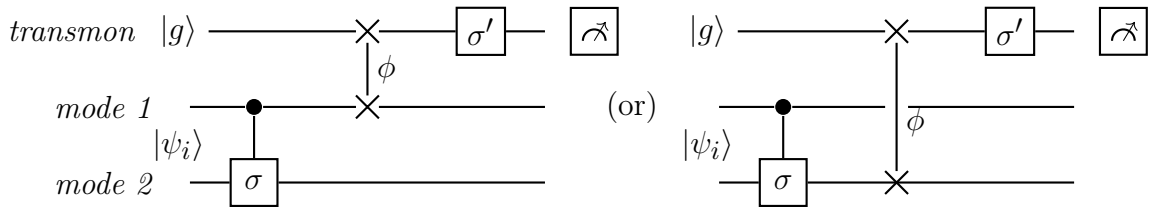

Figure 4.16: General two-mode correlator measurement sequence, where $\sigma, \sigma' \in \{\mathrm{I}, \mathrm{X}, \mathrm{Y}, \mathrm{Z}\}$. To measure and correct additional phase shifts arising in the tomography sequence, we sweep the phase, ϕ, of the final sideband pulse of the sequence used to measure each correlator.

$$\rho = \sum_{ij} \frac{C_{ij} B_i \otimes B_j}{4}. \tag{4.19}$$

In general, fast measurement and reset [23] of the transmon would allow us to perform sequential measurements of two-mode correlations using the transmon without requiring mode-entangling gate operations. For each mode, we would map the mode state to the transmon with an iSWAP, measure the transmon, and reset it to the ground state. The transmon state could be reset with an iSWAP back to the measured mode or to an auxiliary mode. The transmon can subsequently be used to measure the next mode. Additionally, we can perform Wigner tomography [27] of the multimode chain through direct measurements of the multimode fields and parametric amplification. These techniques pose more stringent conditions on the measurement fidelity and speed and are beyond the scope of this work.

As mentioned above process tomography of a two-qubit gate consists of quantum state tomography after acting the gate on a set of 16 linearly independent input states. Process tomography of two-mode gates therefore consists of a set of 240 measurement sequences of the form shown in Figure 4.17.

The gate calibration protocols described in section 4.5 for the CZ gate, and analogous protocols for the CX gate, correct phase errors due to dispersive shifts and the transmon DC-offset from flux modulation during the gate. We additionally correct errors arising from the dispersive shift during the state preparation and tomography (SPAM) segments of the various process tomography sequences. These errors occur in the qubit and iSWAP operations indicated by dashed lines in Figure 4.17. The dispersive shift causes amplitude

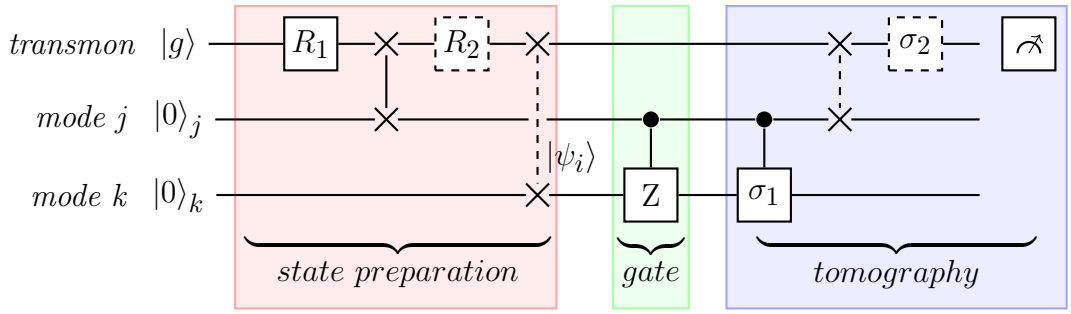

Figure 4.17: Process tomography sequence for two-mode gates, broken down into preparation (red), gate (green), and tomography (blue) segments. For the preparation sequence, we use qubit rotations $R_{1,2} = \left\{I, R_y\left(\frac{\pi}{2}\right), R_x\left(\frac{\pi}{2}\right), R_x\left(\pi\right)\right\}$ and DC-offset corrected sideband iSWAP pulses with an additional $-\frac{\pi}{2}$ phase, such that the target multimode state at the end of the preparation sequence is $|\psi_i\rangle = R_1 \otimes R_2 \left|0_j 0_k\right\rangle$. We measure the density matrix of the gate outputs for given input density matrices $\rho_i = |\psi_i\rangle \langle\psi_i|$ using the state tomography sequences in Table 4.3, corresponding to $\sigma_{1,2} = \{I, X, Y, Z\}$ in the sequence shown above. We note that the iSWAP gate acts on mode k for some of the correlators, and that the tomography sequences that measure single-mode correlators have no additional two-mode gate, corresponding to $\sigma_1 = I$. The qubit and iSWAP operations that are indicated by the dashed lines have errors arising from the dispersive shift.

and phase errors in the transmon and sideband pulses. We again correct only phase errors to first-order in χ/Ω_{sb}. These controlled-phase errors can be formally incorporated as CΦ gates at the end of the preparation sequence (CΦ_p) and prior the to measurement sequence (CΦ_m). These additional gates are concatenated into the gate and tomography sequences as shown in Figure 4.18.

C$\tilde{\mathrm{Z}}$ and C$\tilde{\sigma}_1$ are chosen to give phase-corrected CZ and Cσ_1 gates when concatenated with CΦ_p and CΦ_m, respectively. The preparation error is corrected through an added phase

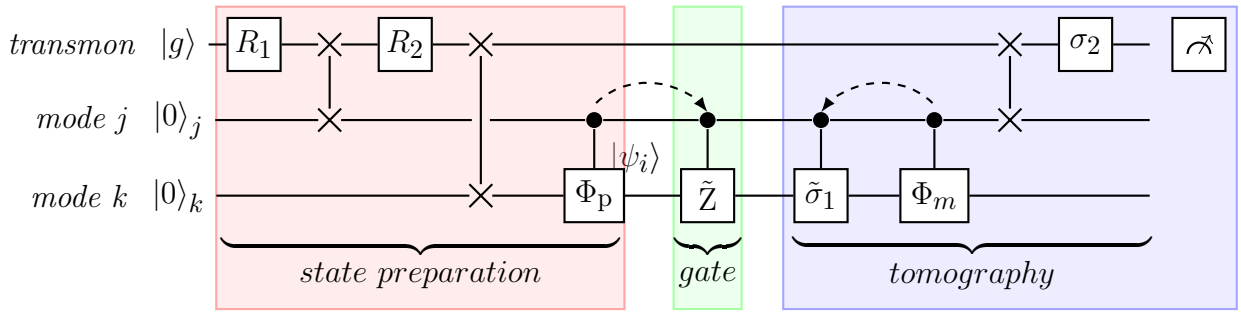

Figure 4.18: Protocol for correcting errors from the dispersive shift, in state preparation and measurement during process tomography of multimode gates.

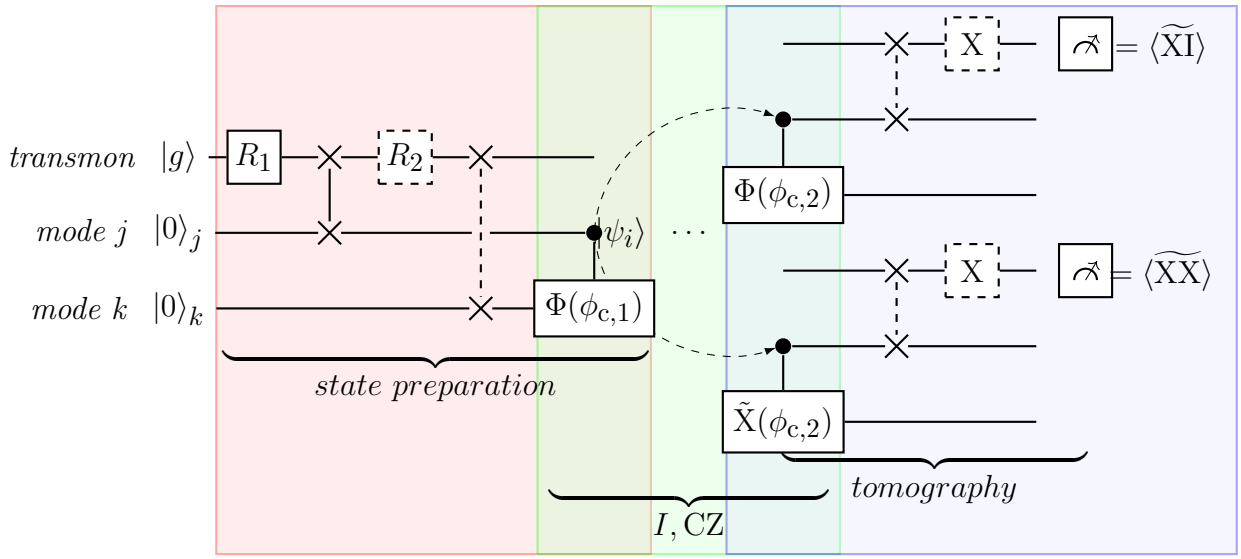

Figure 4.19: Process tomography of the identity gate, used to calibrate the additional SPAM phase errors. We measure the added phases to the $|10\rangle$ and $|11\rangle$ states by comparing the results of correlators with and without CNOT gates, thereby isolating state preparation and measurement errors.

(ϕ_p) in the first $|e\rangle - |f\rangle$ sideband of the first gate, while the tomography error is corrected through an added phase (ϕ_m) in the second $|e\rangle - |f\rangle$ sideband of the last gate of the sequence. We thereby correct the sequence to first-order in the dispersive-shift error. The sideband phases are chosen in this manner in order to correct errors in both the $|10\rangle$ and $|11\rangle$ states (see equations (4.13), (4.14)). The phase errors depend on the duration of the qubit and sideband pulses used in the sequence. In the absence of loss, they can be calculated based on the dispersive shift and pulse shapes.

We calibrate the additional phase errors through process tomography of the identity (I) gate (idling for 10 ns). We find the optimal phases by sweeping the added controlled-phases of the CΦ and Cσ gates, and comparing results for corresponding correlators with and without CX/CY gates (such as XX and XI, respectively) as shown in Figure 4.19.

This scheme allows us to isolate state preparation and measurement errors (ϕ_p and ϕ_m). In the Heisenberg picture, working backward from the transmon measurement, we consider how correlators are modified by the dispersive shift and the correcting two-mode gates.

As an example, for the prepared state $|{+}{+}\rangle$ ($R_{1,2} = Y_{\frac{\pi}{2}}$), the expected values of the

correlators XI and XX are:

$$\langle\widetilde{\mathrm{XI}}\rangle = \cos^2\left(\frac{\phi_{\mathrm{c},1}+\phi_{\mathrm{c},2}-\phi_{\mathrm{p}}-\phi_{\mathrm{m}}}{2}\right), \tag{4.20}$$

$$\langle\widetilde{\mathrm{XX}}\rangle = \cos\left(\frac{\phi_{\mathrm{c},2}-\phi_{\mathrm{c},1}-\phi_{\mathrm{p}}-\phi_{\mathrm{m}}}{2}\right)\cos\left(\frac{\phi_{\mathrm{c},2}+\phi_{\mathrm{c},1}+\phi_{\mathrm{p}}-\phi_{\mathrm{m}}}{2}\right), \tag{4.21}$$

where ϕ_{p} and ϕ_{m} are the phase errors of the $|11\rangle$ state (relative to the other computational basis states) in state preparation and measurement, respectively. Finding and correcting ϕ_{p} and ϕ_{m} amounts to choosing $\phi_{\mathrm{c},1}$ and $\phi_{\mathrm{c},2}$ such that $\langle\widetilde{\mathrm{XI}}\rangle = \langle\widetilde{\mathrm{XX}}\rangle = 1$.

The additional phases only depend on the shape of the qubit and sideband pulse waveforms. As a result, we can calibrate ϕ_{p} and ϕ_{m} for all 240 sequences using a total of 13 unique experiments. We can then extract the full process matrix by measuring at the optimal angles obtained from the calibration experiments. We check that the validity of the calibrations by also additionally sweeping the phase of the final sideband pulse. In order to reduce the SPAM error from decoherence, we combine the state preparation and measurement correction gates (as indicated by the arrows in Figure 4.19) during process tomography of the I and CZ gates, noting that $\mathrm{C}\Phi_{\phi_{\mathrm{c},1}}$ commutes with both of them.

We perform process tomography of the CZ gate by inserting it in place of the I in Figure 4.19, after calibrating the tomography axes. A two-mode gate is fully characterized by the completely positive map $\mathcal{E}$;

$$\mathcal{E}(\rho) = \sum_{m,n=0}^{d^2-1} \chi_{mn}\hat{A}_m\rho\hat{A}_n^\dagger. \tag{4.22}$$

$\hat{A}_m = \hat{B}_i \otimes \hat{B}_j$, with $\hat{B}_i \in \{I, X, Y, Z\}$, forms a basis of operators acting on a two-mode state ρ. χ_{mn} is the process matrix characterizing the two-mode gate, and is extracted from the measured output density matrices ρ_j^{out} for 16 linearly independent input density matrices

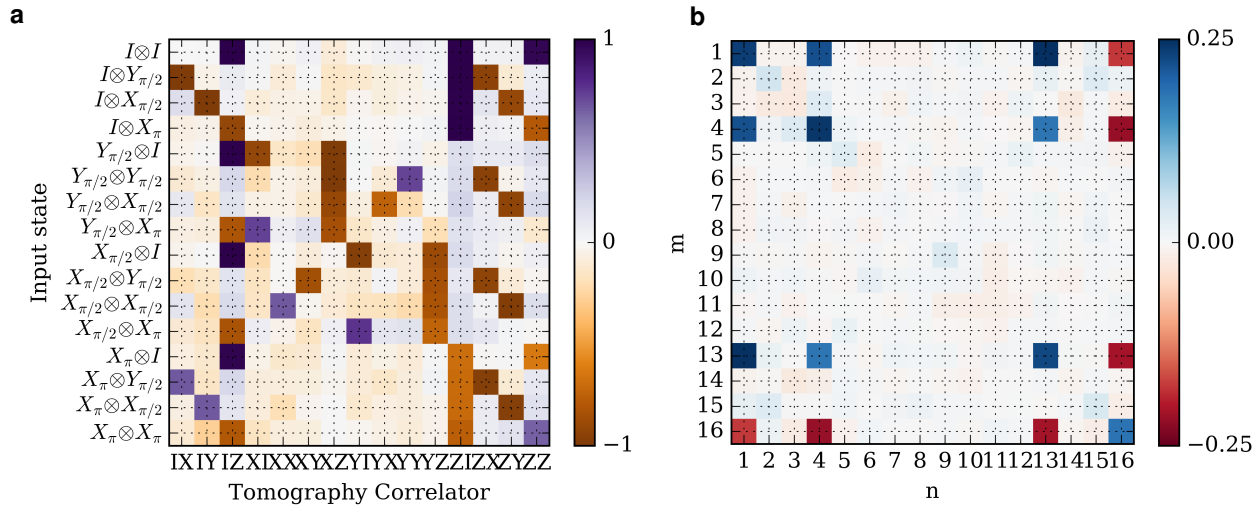

Figure 4.20: **a,** Experimentally measured correlators after correcting for phase errors arising during state preparation and measurement for process tomography of the CZ gate between mode $j = 2$ and $k = 6$. **b,** Process matrix extracted from the resulting measurements by inverting equation (4.24).

(ρ_j) as shown below:

$$\rho_j^{\text{out}} = \mathcal{E}(\rho_j) = \sum_k \lambda_{jk}\rho_k = \sum_{m,n} \chi_{mn}\hat{A}_m\rho\hat{A}_n^\dagger = \sum_{m,n,k} \chi_{mn}\beta_{jk}^{mn}\rho_k, \tag{4.23}$$

$$\Rightarrow \lambda_{jk} = \text{Tr}[\rho_k\rho_j^{\text{out}}] = \sum_{mn} \beta_{jk}^{mn}\alpha_{mn}. \tag{4.24}$$

Equation (4.24) is directly inverted to obtain the process matrix α_{mn}. We do not impose the completeness condition, $\sum_{mn} \chi_{mn}\hat{A}_m\hat{A}_n^\dagger = I$ as a constraint. This constraint arises from the probabilities of states in the relevant two-mode space summing to 1. The process fidelities are extracted from the measured (χ^{m}) and ideal process matrices (χ^{t}) using $F_p = \text{Tr}\left[\chi^{\text{m}}\chi^{\text{t}}\right]$.

In order to obtain a fair estimate of the gate fidelity, each of the process tomography sequences has a single two-mode gate. Additional gates required for tomography are combined with the characterized CZ gate. We use this protocol to characterize the fidelities for gates between 38 mode pairs, as shown in Figure 4.21. The fidelities from full process tomography range approximately from $60 - 80\%$ for the CZ gates between the mode pairs indicated.

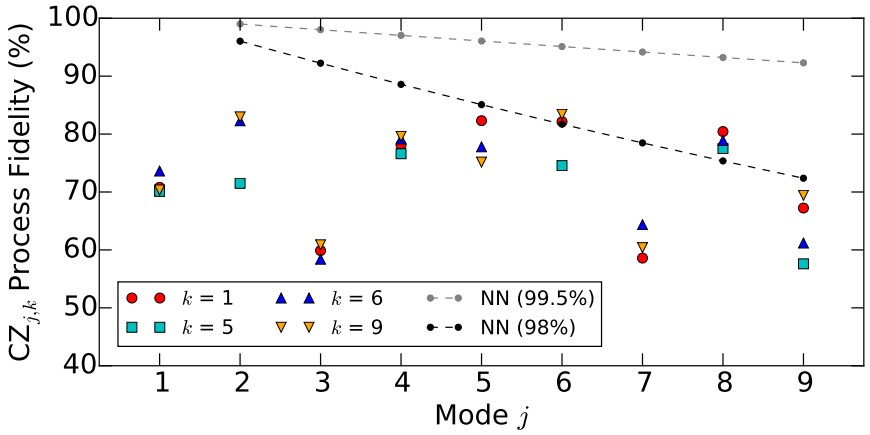

Figure 4.21: Fidelities from process tomography for 38 pairs of memory modes with $k = 2, 5, 6, 8$. The process fidelities are extracted from sequences that include SPAM errors, and are conservative estimates of the gate fidelities. For comparison, the dashed black and gray lines show the decay in fidelity for a two-qubit gate between qubit 1 and qubit j in a corresponding linear array comprising only nearest-neighbor (NN) gates with fidelities of 99.5 [1] and 98%, respectively.

These fidelities incorporate state preparation and measurement (SPAM) errors, with the SPAM sequences being of similar duration as the gates. Conservative estimates from single-mode and transmon RB give SPAM errors of $5 - 10\%$, depending on the modes addressed. The gate fidelities are largely limited by the coherence times of the modes ($\sim 5 - 15\%$ error). The process fidelities are additionally limited by dephasing of the transmon ($\sim 5\%$ error), and residual coherent errors arising from bare and stimulated dispersive shifts. The error from the dephasing can be reduced by coupling a fixed-frequency transmon to the multimode memory using a tunable coupler [7, 41, 35]. Additionally, biasing the tunable coupler at a point with small static coupling also reduces coherent errors from the bare dispersive shift.

Figure 4.21 highlights the advantages of random access in a quantum computing architecture. An entangling gate between the first and the jth qubit of an array with only nearest-neighbor coupling would require $2j - 1$ gates (such as CXs or iSWAPs). This results in an exponential decay of the fidelity with increasing distance between the corresponding qubits. Conversely, in a random access quantum information processor, there is no additional computational cost to perform gates between arbitrary pairs of qubits. Even without con-

sidering potential improvements in the coherence times, we see that the processor performs competitively with state-of-the-art gates [1] between distant qubits in a nearest-neighbor architecture. While we have highlighted the advantages of this processor in terms of random access and minimal control hardware, a resulting requirement is the need to perform sequential operations. The number of modes which can be multiplexed to a single qubit without loss of fidelity, is given by the ratio of the loss from idling in a cavity mode to the loss in performing qubit operations. This suggest using bulk 3D superconducting microwave cavities, for which this ratio can be up to 100 [54] or higher [56]. We will investigate creating a 3D multimode memory cavity in the next chapter.

CHAPTER 5

NOVEL DESIGN OF LONG-LIVED QUANTUM MEMORIES WITH 3D CAVITIES

As mentioned in the previous chapter, an essential ingredient for the aforementioned architecture for viable quantum information processing is a long-lived quantum memory. Recent progress has been made demonstrating single-photon lifetimes from 1-10 ms in bulk, three-dimensional (3D) superconducting microwave cavities [53, 54], a one-to-two order of magnitude improvement over state-of-the-art transmon qubits. Quality factors achieved in modern accelerator cavities promise potential for an additional two orders of magnitude improvement [56]. Furthermore, decoherence in these cavities is dominated by photon loss error, allowing for selective error-correcting codes, such as the cat and binomial codes [43, 42].

In this chapter, we will introduce a novel method for constructing monolithic 3D microwave cavities, thus eliminating a potential source of loss in these cavities: conducting loss at the seam between two pieces of the cavity. This method can be used to make a variety of cavity geometries, allowing for minimization of surface loss susceptibility, as well as allowing for creation of specific spectral distributions for multimode cavities. We conclude by describing quality factors measurements performed on these cavities.

5.1 Types of loss in 3D cavities

Photons in 3D cavities have notably superior lifetimes to planar resonators. This is primarily due to the vastly smaller participation of the photon fields at the surface of cavity, where dielectric and normal metal defects lie. Explicitly, we can calculate surface-to-volume participation ratios for the electric and magnetic fields, which relate the losses at the surface to the effective photon loss of the cavity. The dielectric participation ratio is given by

$$p = \frac{\epsilon \, t \int_S |E|^2 \, \mathrm{d}A}{\int_V |E|^2 \, \mathrm{d}V}, \tag{5.1}$$

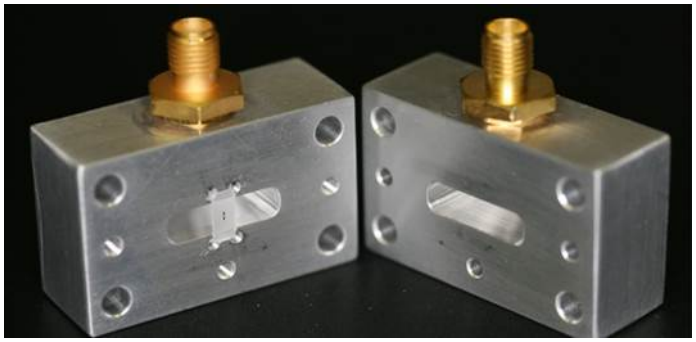

Figure 5.1: Coffin-style rectangular cavity. It is made from two halves of the cavity machined individually and mated together through contact. The seam where these two halves mate is susceptible to conduction loss.

where ϵ and t are the relative permittivity and thickness of the surface dielectric. This ratio gives the surface dielectric-limited quality factor of cavity photons, $Q_E = Q_d/p$, for a given surface dielectric quality factor $Q_d = 1/\tan\delta_d$. Similarly, the surface conductance participation ratio is

$$\alpha = \frac{\lambda \int_S |H|^2 \, \mathrm{d}A}{\int_V |H|^2 \, \mathrm{d}V} \tag{5.2}$$

where λ is the London penetration depth of the surface. In the presence of finite surface resistance, the conductance-limited quality factor of cavity photons is $Q_H = Q_s/\alpha$. Here, the surface conductance quality factor, Q_s, is related to surface resistance, R_s, by $Q_s = \omega\mu\lambda/R_s$, where ω is the cavity frequency. The ratio α is also known as the kinetic inductance fraction, the portion of the effective mode inductance that results from kinetic inductance of Cooper pairs carrying current.

In addition to surface losses, many typical cavities suffer from conduction loss on the seam between the halves that form the cavity, such as in the "coffin"-style rectangular waveguide cavity shown in Figure 5.1. To address this source of loss, monolithic, or "seamless" cavities have been developed [53], in the form of quarter-wave coaxial stub cavities, as show in Figure 5.2. In these cavities, the electromagnetic fields in the cavity are localized around the stub near the bottom of the cavity, far from any seams that may exist. The mode only has evanescent leakage to the top of the cavity, making any conduction loss via that seam

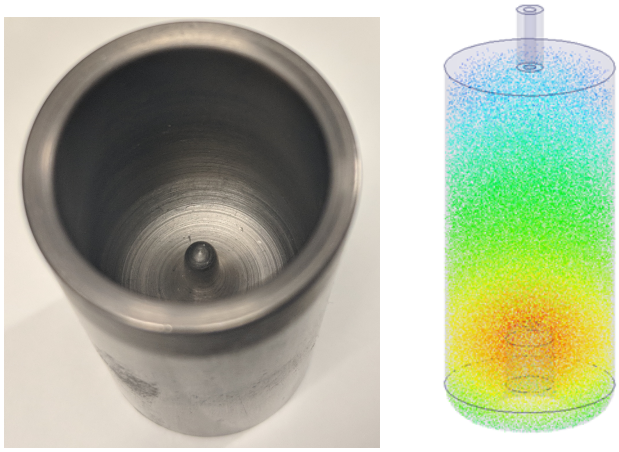

Figure 5.2: A coaxial quarter-wave "stub" cavity. On the left is a picture of a cavity made from niobium. On the right is a plot of the magnitude of the electric field of the fundamental mode of the cavity, on logarithmic scale with arbitrary units. The mode's field is localized near the stub, with only evanescent coupling to any potential seam at the top of the cavity.

marginal.

While coaxial stub cavities have a number of advantages, including isolation of the fundamental mode of the cavity, they are limited in geometric flexibility towards optimizing surface participation ratios, as well for convenience in design multimode spectra. In the rest of this chapter, we will introduce a method to create monolithic cavities of many different geometries with a simple fabrication technique.

5.2 Quantum flute

As an introduction to the quantum flute, first we will describe how to create a rectangular waveguide cavity using the flute method of fabrication. First, from the top of the stock material, we drill a linear array of blind holes with diameter d, spaced by a gap $g < d$. The length end-to-end of this array sets the length of the cavity, a. Next, we flip the stock and drill another array of blind holes, each centered in between two holes on the opposite side of the stock. The overlap between the two arrays of holes form the bulk of the cavity, where the length of overlaps sets the other cavity dimension b. Figure 5.3 depicts how this method indeed creates a rectangular waveguide cavity. The resonant frequencies of the modes of the

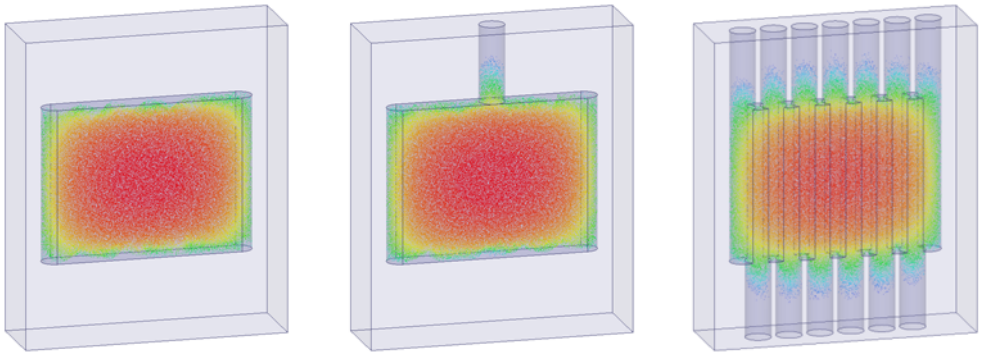

Figure 5.3: Construction of the quantum flute. (a) A rectangular waveguide cavity with the electric field of its fundamental mode, TE_{101}, calculated with a finite element solver, plotted on a logarithmic scale. (b) A blind hole drilled into the cavity, with a diameter equal to width of the cavity. From the exponential decay of the field, it is clear that hole evanescent at the mode frequency. (c) A monolithic rectangular waveguide cavity composed entirely of these evanescent holes, drilled from both the top and bottom of the stock.

cavity are:

$$f_{mn\ell} = \frac{c}{2}\sqrt{\left(\frac{m}{a}\right)^2 + \left(\frac{n}{b}\right)^2 + \left(\frac{\ell}{d}\right)^2}, \tag{5.3}$$

where m, n, ℓ are integers and at least two are non-zero.

To ensure that the holes leading out of the cavity are evanescent, the cutoff frequency of waveguide modes of the holes must be well above the resonance frequency of the relevant cavity mode. In practice, to ensure that the loss due to leakage through all modes of these holes is not limiting the quality factors of any arbitrary geometries, we use finite-element simulation with vacuum impedance boundary conditions at the edge of the holes. For all the cavities in this work, the limits due to seam loss give quality factors of 10^{10} or higher.

5.3 Fabricating flute cavities in various geometries

One of the main benefits of the flute method for 3D cavities is the ability to make cavities in a variety of geometries for various potential applications. First, we will describe the fabrication of a cylindrical disk cavity. In this case, radial holes are drilled around the stock, with the depth of the holes from the center of the stock setting the radius, r, of the cavity and the diameter of the holes setting the height, $h = d$. The resonance frequency of transverse

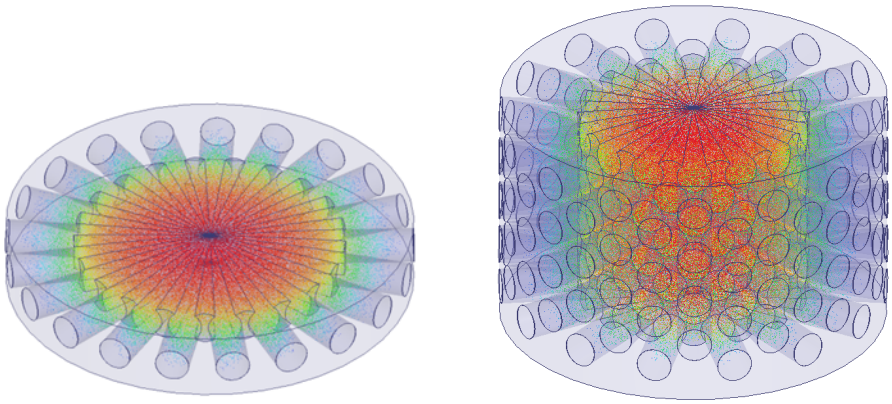

Figure 5.4: Cylindrical flute cavities. The cylindrical disk flute cavity is formed by drilling holes around a circular stock, with the overlap of the holes forming the cavity volume and the depth of the holes from the center determining the radius. This geometry can be expanded to taller cylindrical cavities by stacking overlapping disks on top of one another. To avoid overlapping the evanescent holes from the cavity, every other layer in the stack rotated with respect to the previous layer.

magnetic (TM) and transverse electric (TE) modes of this cavity are given by

$$f_{mn\ell}^{\mathrm{TM}} = \frac{c}{2\pi}\sqrt{\left(\frac{X_{mn}}{r}\right)^2 + \left(\frac{p\ell}{h}\right)^2}, \tag{5.4}$$

$$f_{mn\ell}^{\mathrm{TE}} = \frac{c}{2\pi}\sqrt{\left(\frac{X'_{mn}}{r}\right)^2 + \left(\frac{p\ell}{h}\right)^2}, \tag{5.5}$$

where X_{mn} and X'_{mn} are the nth zeroes of the mth Bessel function and the derivative of the mth Bessel function, respectively. In the "disk" limit, where $d \ll r$, the fundamental mode of this cavity is the TM_{010}, which is shown in Figure 5.4.

While this method works for thin disk cavities, it needs to be modified to create cylindrical cavities with different ratios of height to radius. This can be achieved by "stacking" disk cylindrical cavities on top of one another with some overlap. However, to avoid increasing the cross section of the evanescent holes when stacking the cavities, the orientation of the holes in every other layer is rotated, as shown in Figure 5.4. This enables any ratio of height and radius for cylindrical cavities, allowing for optimization of surface participation ratios and accessibility to other modes of the cavity.

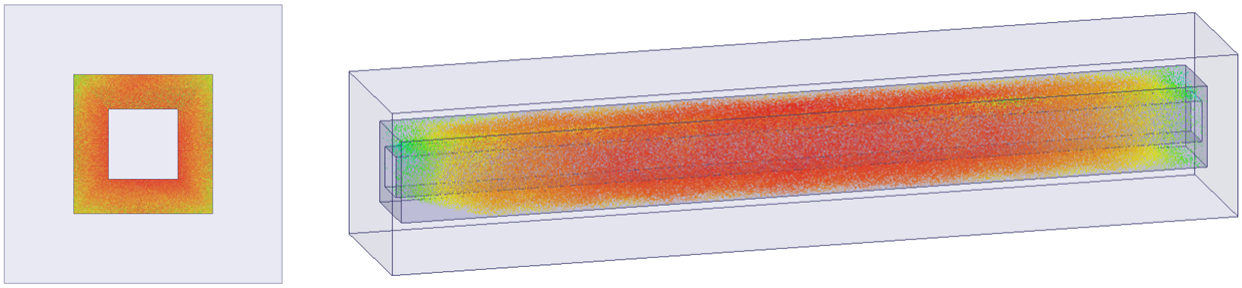

Figure 5.5: A half-wave coaxial cavity. The cavity consists of an inner and outer conductor separated by vacuum and shorted at either end. The electric field of the fundamental mode of the cavity is plotted.

The flute method also allows for the construction of seamless cavity of more exotic forms. For example, we can construct a coaxial half-wave resonator, where the inner conductor is separated from the outer conductor by vacuum and shorted at either end of the cavity. A depiction of such a cavity, along with the electric field of its fundamental mode, is shown in Figure 5.5.

Unlike the rectangular waveguide and cylindrical disk cavities, the boundary conditions determining the fundamental frequency mode of the cavity are one-dimensional. The frequency of the modes of the cavity are

$$f_n = c\frac{n}{2a}, \tag{5.6}$$

where a is the length of the cavity. Because of these boundary conditions, creating cavities with low frequency modes requires only a single large dimension, while the cavities described earlier would require at least two large dimensions to achieve similar frequencies. Creating this cavity with the flute method requires drilling a cross-section in the shape of a square using four holes drilled from four sides, as shown in Figure 5.6. Each of the holes is drilled deep enough to intersect the holes drilled from the faces orthogonal to that holes face. Then, for each of the four sides of the resulting square, we use the technique for making the rectangular waveguide cavity to elongate the cavity to the desired length a. In this sense, the half-wave coaxial cavity can be thought of as a combination of four rectangular waveguide

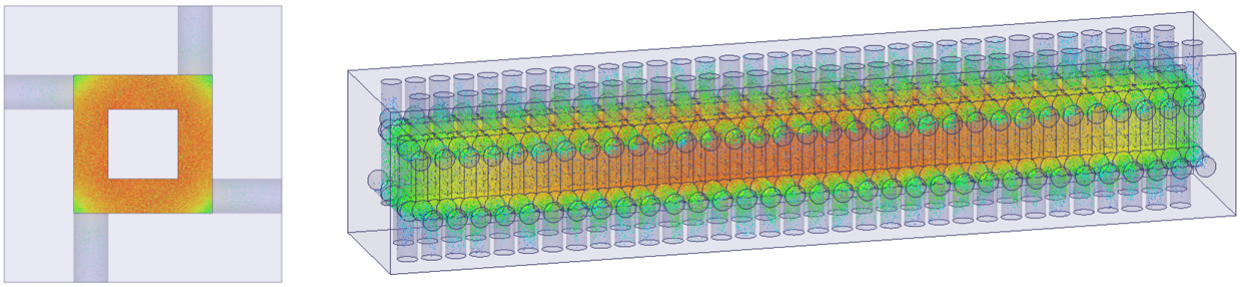

Figure 5.6: A half-wave coaxial cavity, constructed with the flute method. On the left, there is a cross section showing the building block of the cavity, where a square separating the outer and inner portions of the cavity is made from four holes drilled on four faces of the stock. To create the complete cavity, the pattern is repeated for each of the four holes, but alternating the face of the cavity on which the hole is drilled, just as in the rectangular waveguide flute. The electric field of the fundamental mode of the cavity is plotted.

cavities.

5.4 3D Multimode cavities

As seen in the previous sections, 3D cavities are multimodal in nature. To utilize this in the random access quantum information processor described in the earlier sections, the spectra of the modes need to be modified to be useful for the processor. Thus, we need a band of modes that are relatively closely spaced (free spectral range of ~ 100 MHz) and that can all be coupled to a superconducting qubit. To achieve such a mode distribution, we can start by taking a careful look at the spectrum of modes of the rectangular waveguide (5.3). If we take the limit $a \gg b > d$, we find the lowest frequency modes (small m) have a spectrum

$$f_m \approx \frac{c}{2b} + \frac{cb}{4a^2}\, m^2. \tag{5.7}$$

The modes begin with a fundamental frequency primarily determined by the second largest dimension b and then follow a quadratic distribution in m. An example of such a cavity is shown in Figure 5.7.

This cavity can also be created using the flute method for rectangular waveguide cavities described earlier. An example of such a design is shown in Figure 5.8.

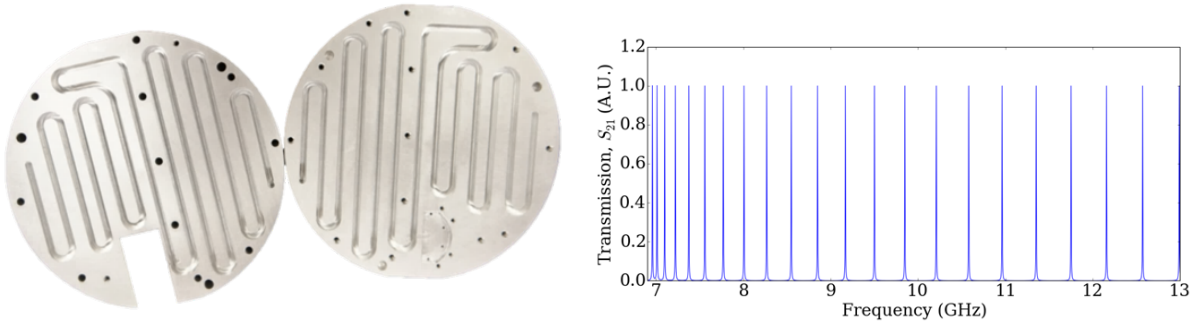

Figure 5.7: A 3D multimode rectangular waveguide cavity and its spectrum. The cavity is a "coffin"-style cavity with dimensions $a = 1$ m, $b = 2$ cm, and $d = 5$ mm. Its modes have a base frequency ~ 7 GHz, with a band of modes above with a quadratic distribution with free spectral range from ten MHz up to several hundred MHz.

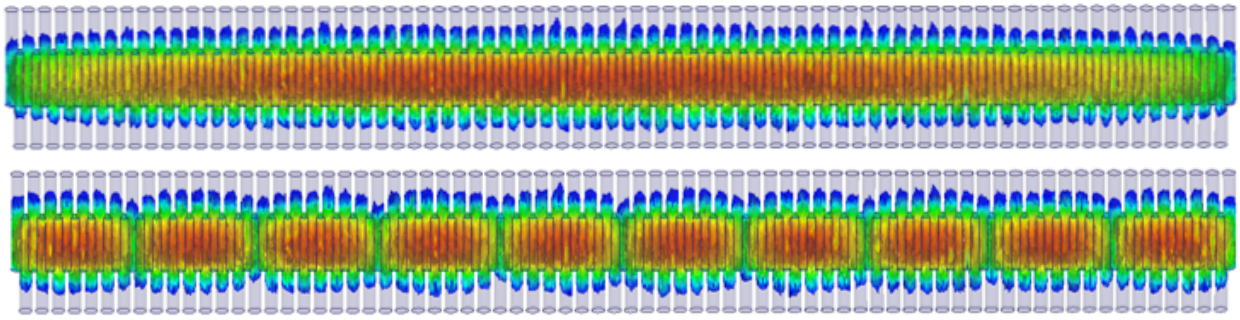

Figure 5.8: A multimode cavity constructed using the flute method. The top figure shows the fundamental mode of the cavity and the bottom figure shows the tenth mode.

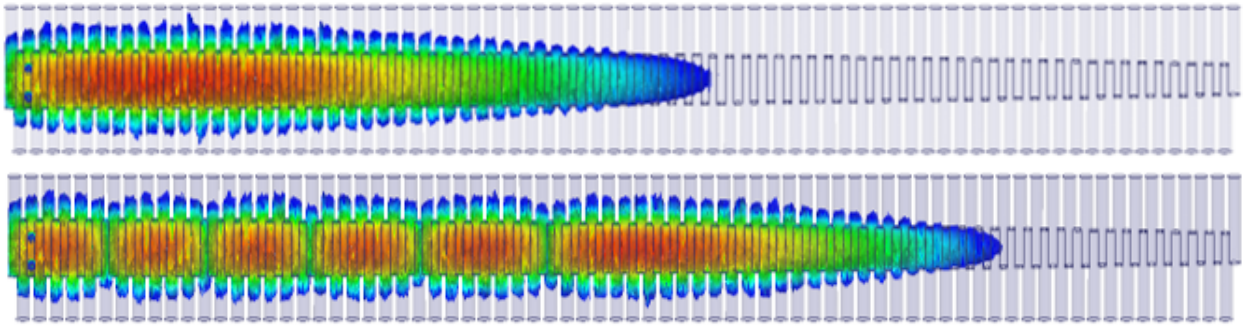

Figure 5.9: A tapered multimode flute cavity. By varying the depth of the drilled holes used to create the flute, the height of the cavity is tapered along its length. This changes the effective length of the modes depending on the mode number, as is clear in the electric field distributions for the first and sixth modes of the cavity in the figure.

In the cavity in Figure 5.7, which has dimensions $a = 1$ m, $b = 2$ cm, and $d = 5$ mm, the eigenmode spectrum has a base frequency of around 7 GHz and a quadratic distribution of eigenmodes with a free spectral range from tens to hundreds of megahertz. While this gets us near the goal for the ideal distribution of modes for the random access quantum information processor, the variation in free spectral can cause potential issues for cross-talk error during operation. This is particularly apparent when considering operations involving higher levels of the transmon, as described in the earlier chapters. Fortunately, the flute method enables us to tailor the mode distribution by perturbing the shape of the cavity.

One possible mode distribution would be linear spacing, where the free spectral range across the eigenmodes was identical. With an appropriate choice of anharmonicity, the higher level sideband transitions can be well detuned from the fundamental sideband transitions, to limit cross-talk during operations. To create such a distribution, we reconsider Equation (5.7). In this equation, we can get linearly spaced modes if the coefficient in front of the term quadratic in m is proportional to m^{-1}. If the effective length, a, of the modes varies with mode number, m, as $a \propto \sqrt{m}$, this condition would be met. In the quantum flute, by parabolically tapering the height of the cavity along its length, we can achieve this, as shown in Figure 5.9. The tapering is created reducing the depth of the drilled holes along the cavity.

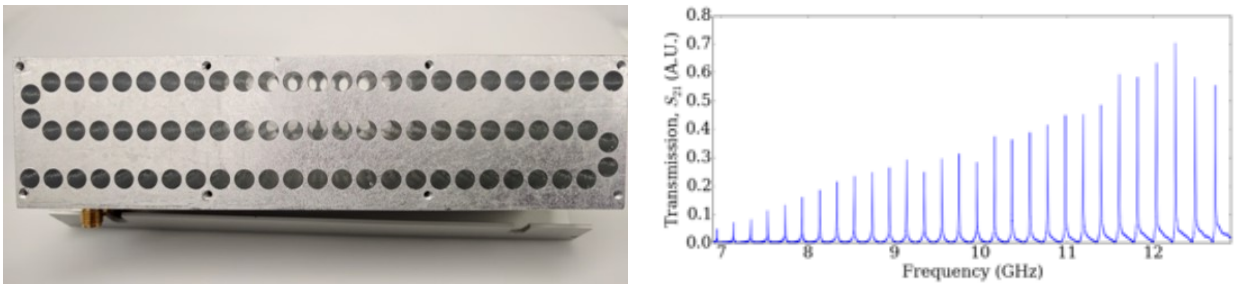

Figure 5.10: A machined multimode flute cavity and its spectrum. The cavity is machined from high-purity aluminum (99.9995%) and is wet etched before measurement to remove oxides and residual defects from machining. The spectrum is a transmission transfer function measured through microwave coaxial ports on the side of the cavity.

With the help of finite element simulation, we designed a cavity with a base frequency of ~ 7 GHz and a free spectral range of ~ 200 MHz for the 25 lowest frequency modes of the cavity. We then machined the cavity out of high-purity (99.9995%) aluminum and measured its spectrum at room temperature, as shown in Figure 5.10.

5.5 Cavity measurements

We cooled down the multimode cavity to 20 mK to measure the quality factors of its eigenmodes. The measurements were done in transmission, with the coupling quality factor of the input and output ports set to be greater than 10^9 as predicted by finite element simulation. As a result, the measured quality factor of the cavities is limited by internal losses. An example of the resulting measurements is given in Figure 5.11. The real and imaginary parts of the transmission profile were measured for each mode and then used to find the magnitude of transmission, which was fit to extract the resonance frequencies and quality factors.

Additionally, we performed ringdown measurements to verify the photon lifetimes in the cavities. This measurement was done by using a pulse to populate the cavity with a small number of photons ($\bar{n} < 1$), then waiting some time and measuring the population of the cavity. An example of this measurement is also shown in Figure 5.11. These measurements are done for 21 modes in the cavity, with the results plotted in Figure 5.12.

In addition to measurements done at 20 mK, the modes are also measured as a function

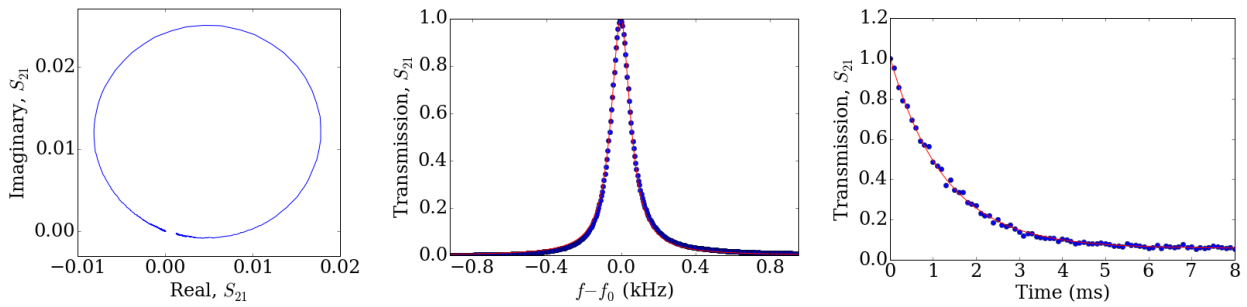

Figure 5.11: Measurements on the fifth mode of the cavity, whose resonance frequency is $f_0 = 7.777$ GHz. On the left is a plot of the real and imaginary parts of the the transmission. From the components of the transmission, we can find the magnitude of the transmission profile and fit it to a Lorentzian profile to extract the quality factor of the mode, 60.1 million. We can do an additional measurement, known as a ringdown, to extract a decay time for photons in the cavity. This measurement consists of a pulse to excite a small number of photons ($\bar{n} < 1$) in the cavity, then wait for a time and measure the population of the cavity. For the fifth mode, this give a lifetime of 1.26 ms, consistent with the quality factor measurement.

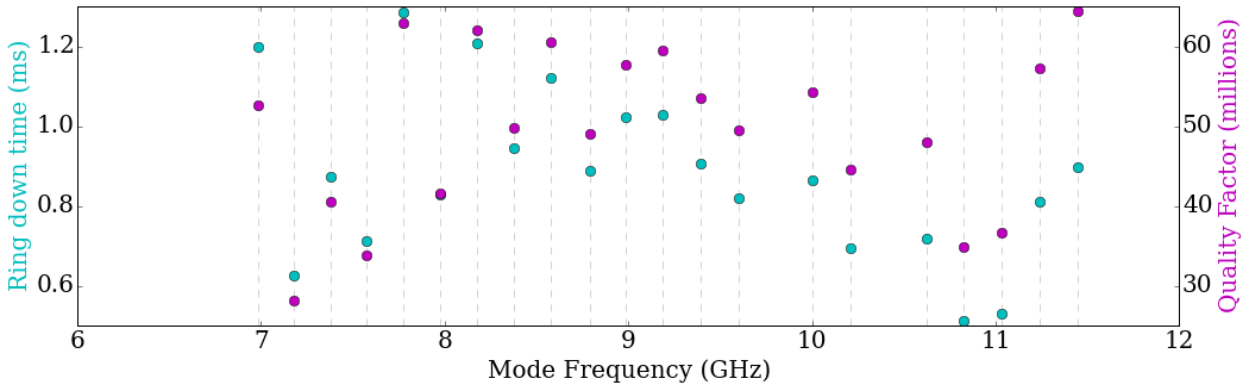

Figure 5.12: Quality factors and ringdown lifetimes for measured modes in the cavity, plotted versus mode frequency. The measured quality factors range from 25-65 million, with corresponding ringdown times from 0.5-1.3 ms. No general trend is apparent over mode frequency.

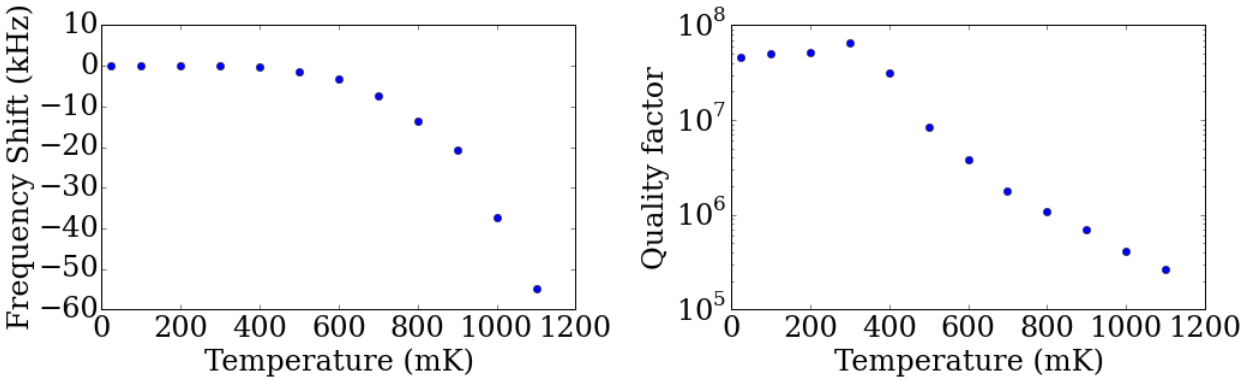

Figure 5.13: Temperature sweep of the fourth mode of the cavity. Due to the increase in kinetic inductance as a function of temperature, the resonance frequency of the modes shifts downward. Additionally, due to the increase in the thermal quasiparticle current carriers, the quality factor decreases exponentially as the temperature approaches the critical temperature of aluminum. However, at low temperatures, less than 300 mK, we in fact see a slight increase in quality factor with temperature. This indicates that the quality factor is limited by some mechanism other than thermal quasiparticle surface resistance, such as non-equilibrium quasiparticles or two-level systems.

of temperature, up to the critical temperature of aluminum. The frequency shifts and the quality factors of the modes are extracted as a function of temperature, as shown for a given mode in Figure 5.13. From these frequency shifts, we can extract the surface conduction participation ratio, α. The temperature dependence of the superconducting gap, Δ, in Bardeen-Cooper-Schrieffer (BCS) theory is determined by [64]

$$\frac{1}{N(0)V} = \int_0^{\omega_c} \frac{\tanh\left(\frac{1}{2}\beta\sqrt{\xi^2+\Delta^2}\right)}{\sqrt{\xi^2+\Delta^2}}\, \mathrm{d}\xi, \tag{5.8}$$

where $\beta = 1/k_B T$, $N(0)$ is the density of states at the Fermi level, V is the binding energy of electrons, and ω_c is related to the critical temperature T_c of the superconductor:

$$k_B T_c = 1.13\hbar\omega_c e^{-1/N(0)V}. \tag{5.9}$$

For conventional superconductors $N(0)V \approx 0.3$ and the critical temperature of aluminum is 1.196 K [12]. The gap as a function of temperature can be determined via numerical

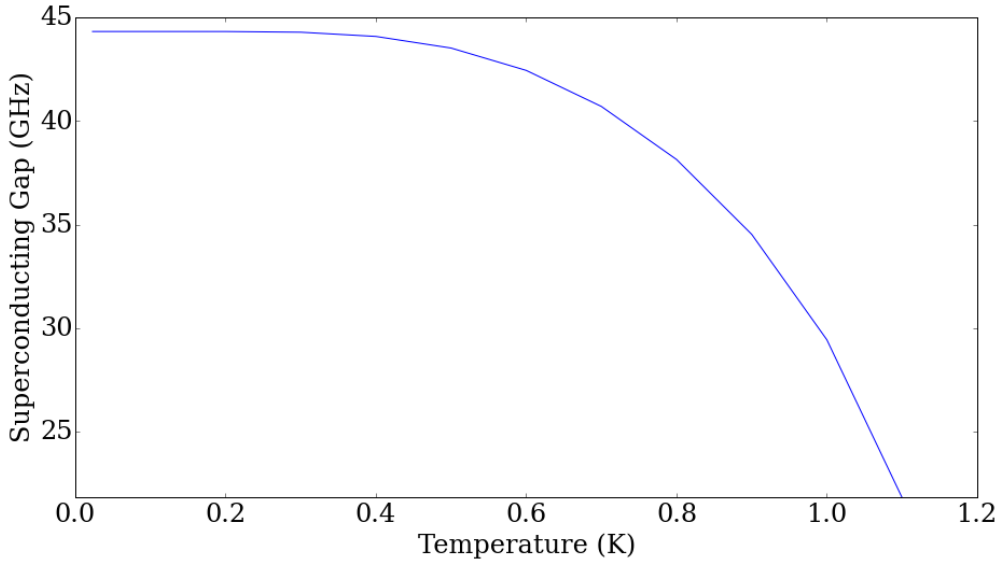

Figure 5.14: The superconducting gap of aluminum as a function of temperature, determined numerically.

integration, as shown in Figure 5.14. Given the gap, we can determine the imaginary part of the complex conductivity, $\sigma = \sigma_1 + i\sigma_2$, of the superconducting surface as a function of temperature

$$\sigma_2 = \frac{1}{\omega}\int_{\Delta-\omega}^{\omega} \frac{(\epsilon+\omega)\epsilon + \Delta^2}{\sqrt{(\epsilon+\omega)^2-\Delta^2}\sqrt{\Delta^2-\epsilon^2}} \tanh\left(\frac{\epsilon+\omega}{2k_BT}\right) \mathrm{d}\epsilon. \tag{5.10}$$

The frequency shift of the resonator is directly related to change in the imaginary part of the surface conductivity by the conduction surface participation ratio:

$$2\frac{\delta f}{f_0} = \alpha\frac{\delta\sigma_2}{\sigma_2}. \tag{5.11}$$

Thus, we can extract the α for each of the modes from the temperature dependent shift, as in Figure 5.15.

For the fourth mode, we compare this ratio to that predicted by finite element simulation, $\alpha_{\mathrm{sim}} = 8.65 \times 10^{-6}$. We could consider the discrepancy between the experiment and simulation as a difference in London penetration depth, which is 16 nm for pure aluminum.

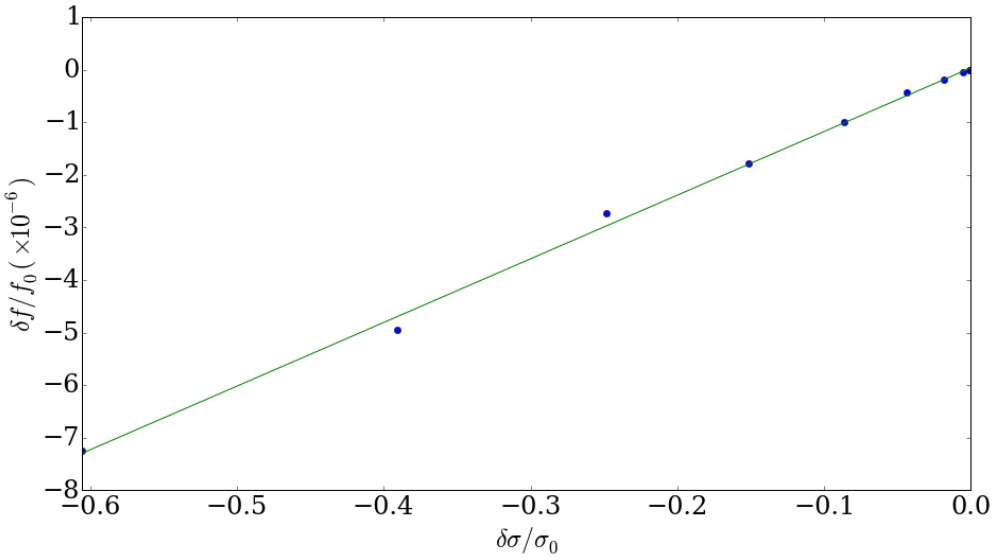

Figure 5.15: The frequency shift of the fourth mode of the cavity, as a function of the change in conductivity. The change in conductivity is determined from BCS theory as a function of temperature and the frequency is measured as a function of temperature. From the fit, we determine the conduction surface participation ratio to be 2.25×10^{-5}.

The experimentally determined depth of 43 nm is likely a result of defects in the surface of the cavity due to imperfections in the surface finish, residual oxide, or other defects.

CHAPTER 6

OUTLOOK

Recent progress in quantum information science has the field on an exciting precipice: demonstration of quantum advantage over classical computers. This has inspired a significant effort for applications to utilize quantum computing on the near term. However, this recent excitement is tempered by the daunting challenge of extending the recent accomplishments toward a fully error-corrected quantum computer. To realize such a goal, we will have to utilize the advantages of many of the schemes that have been developed.

Here, we have presented an implementation of a random access quantum information processor relying on multimode resonator memories and shown methods of making these memories with ultra-high coherence 3D multimode cavities. This type of architecture, where many memory qubits are attached to a central control unit for processing, is ideal when the idling error rate of the memories is much smaller than the error rate of the processor. The question is how does architecture fits into modern proposed error correction schemes.

To understand this one must ask, how often should error correct a given logical qubit? In schemes where the idling error is on the order of the gate error of the qubits, the frequency of error correction is generally a few times slower than the gate times. However, if the idle error is much smaller, one is better off correcting less often. Now, we see that if we utilize a random access processor, we can gain from the fact we can correct other qubits in the manifold while a corrected qubit is idling.

This scheme is compatible generally with many types of error correcting codes. As an example, let us consider an architecture consisting an array of physical qubits organized to be compatible with a surface code [21] that encodes a number of logical qubits. Each of the physical qubits would have a multimode memory attached to it, which is randomly accessible. Now, we can think of one memory qubit at an array site as a part of "layer" of surface code. To do gates between layers would require gates between the layers' memory qubits at each array site, which is straightforward between any two qubits in a random access

processor.

The scheme outlined here is compatible with number of other multibit codes, including the Shor [58] and Steane codes [62]. Additionally, because the memory modes are harmonic oscillators, they are also compatible with bosonic error correction schemes [43, 42]. Given this vast error correction compatibility, random access processors using multimode cavities hold promise as an ingredient in a viable quantum information processor.

BIBLIOGRAPHY

[1] R Barends et al. "Superconducting quantum circuits at the surface code threshold for fault tolerance". In: *Nature* 508.7497 (2014), pp. 500–503.

[2] Félix Beaudoin et al. "First-order sidebands in circuit QED using qubit frequency modulation". In: *Phys. Rev. A* 86 (2 Aug. 2012), p. 022305. DOI: 10.1103/PhysRevA.86.022305. URL: http://link.aps.org/doi/10.1103/PhysRevA.86.022305.

[3] J. J. Bollinger et al. "Optimal frequency measurements with maximally correlated states". In: *Phys. Rev. A* 54 (6 Dec. 1996), R4649–R4652. DOI: 10.1103/PhysRevA.54.R4649. URL: http://link.aps.org/doi/10.1103/PhysRevA.54.R4649.

[4] Satyendra Nath Bose. "Plancks gesetz und lichtquantenhypothese". In: (1924).

[5] Peter Brooks, Alexei Kitaev, and John Preskill. "Protected gates for superconducting qubits". In: *Physical Review A* 87.5 (2013), p. 052306.

[6] Jonas Bylander et al. "Noise spectroscopy through dynamical decoupling with a superconducting flux qubit". In: *Nat. Phys.* 7.7 (2011), pp. 565–570.

[7] Yu Chen et al. "Qubit architecture with high coherence and fast tunable coupling". In: *Phys. Rev. Lett.* 113.22 (2014), p. 220502.

[8] Jerry M Chow et al. "Implementing a strand of a scalable fault-tolerant quantum computing fabric". In: *Nat. Comm.* 5 (2014), p. 4015.

[9] Jerry M Chow et al. "Optimized driving of superconducting artificial atoms for improved single-qubit gates". In: *Physical Review A* 82.4 (2010), p. 040305.

[10] JM Chow et al. "Randomized benchmarking and process tomography for gate errors in a solid-state qubit". In: *Phys. Rev. Lett.* 102.9 (2009), p. 90502.

[11] John Clarke, Wolfgang M Goubau, and Mark B Ketchen. "Tunnel junction dc SQUID: fabrication, operation, and performance". In: *Journal of Low Temperature Physics* 25.1-2 (1976), pp. 99–144.

[12] John F. Cochran and D. E. Mapother. "Superconducting Transition in Aluminum". In: *Phys. Rev.* 111 (1 July 1958), pp. 132–142. DOI: 10.1103/PhysRev.111.132. URL: https://link.aps.org/doi/10.1103/PhysRev.111.132.

[13] *Creative Commons Attribution 4.0 International License*. Creative Commons. URL: https://creativecommons.org/licenses/by/4.0/legalcode.

[14] S Debnath et al. "Demonstration of a small programmable quantum computer with atomic qubits". In: *Nature* 536.7614 (2016), pp. 63–66.

[15] Michel H Devoret and Robert J Schoelkopf. "Superconducting circuits for quantum information: an outlook". In: *Science* 339.6124 (2013), pp. 1169–1174.

[16] L DiCarlo et al. "Demonstration of two-qubit algorithms with a superconducting quantum processor". In: *Nature* 460.7252 (2009), pp. 240–244.

[17] R. H. Dicke. "Coherence in Spontaneous Radiation Processes". In: *Phys. Rev.* 93 (1 Jan. 1954), pp. 99–110. DOI: 10.1103/PhysRev.93.99. URL: http://link.aps.org/doi/10.1103/PhysRev.93.99.

[18] Georg Duffing. *Erzwungene Schwingungen bei veränderlicher Eigenfrequenz und ihre technische Bedeutung*. 41-42. F. Vieweg & sohn, 1918.

[19] Nathan Earnest et al. "Realization of a Λ System with Metastable States of a Capacitively Shunted Fluxonium". In: *Physical review letters* 120.15 (2018), p. 150504.

[20] Artur K Ekert et al. "Direct estimations of linear and nonlinear functionals of a quantum state". In: *Phys. Rev. Lett.* 88.21 (2002), p. 217901.

[21] Austin G Fowler et al. "Surface codes: Towards practical large-scale quantum computation". In: *Phys. Rev. A* 86.3 (2012), p. 032324.

[22] Jay M. Gambetta, Jerry M. Chow, and Matthias Steffen. "Building logical qubits in a superconducting quantum computing system". In: *npj Quantum Information* 3.1 (2017), p. 2. ISSN: 2056-6387. DOI: 10.1038/s41534-016-0004-0. URL: https://doi.org/10.1038/s41534-016-0004-0.

[23] K. Geerlings et al. "Demonstrating a Driven Reset Protocol for a Superconducting Qubit". In: *Phys. Rev. Lett.* 110 (12 Mar. 2013), p. 120501. DOI: 10.1103/PhysRevLett.110.120501. URL: http://link.aps.org/doi/10.1103/PhysRevLett.110.120501.

[24] Sergey Gladchenko et al. "Superconducting nanocircuits for topologically protected qubits". In: *Nat. Phys.* 5.1 (2009), pp. 48–53.

[25] Daniel Gottesman. "The Heisenberg representation of quantum computers". In: *arXiv preprint quant-ph/9807006* (1998).

[26] Peter Groszkowski et al. "Coherence properties of the 0-π qubit". In: *New Journal of Physics* 20.4 (2018), p. 043053.

[27] Serge Haroche and Jean-Michel Raimond. *Exploring the Quantum: Atoms, Cavities, and Photons*. Oxford University Press, 2006.

[28] D. Hucul et al. "Modular entanglement of atomic qubits using photons and phonons". In: *Nat. Phys.* 11.1 (Jan. 2015), pp. 37–42. ISSN: 1745-2473. URL: http://dx.doi.org/10.1038/nphys3150.

[29] Brian David Josephson. "Possible new effects in superconductive tunnelling". In: *Physics letters* 1.7 (1962), pp. 251–253.

[30] Julian Kelly et al. "State preservation by repetitive error detection in a superconducting quantum circuit". In: *Nature* 519.7541 (2015), pp. 66–69.

[31] H Jeff Kimble. "The quantum internet". In: *Nature* 453.7198 (2008), pp. 1023–1030.

[32] Emanuel Knill et al. "Randomized benchmarking of quantum gates". In: *Phys. Rev. A* 77.1 (2008), p. 012307.

[33] Jens Koch et al. "Charge-insensitive qubit design derived from the Cooper pair box". In: *Phys. Rev. A* 76 (4 Oct. 2007), p. 042319. DOI: 10.1103/PhysRevA.76.042319. URL: http://link.aps.org/doi/10.1103/PhysRevA.76.042319.

[34] Norbert M Linke et al. "Experimental comparison of two quantum computing architectures". In: *Proceedings of the National Academy of Sciences* 114 (2017), pp. 3305–3310.

[35] Yao Lu et al. "Universal Stabilization of a Parametrically Coupled Qubit". In: *Phys. Rev. Lett.* 119 (15 Oct. 2017), p. 150502. DOI: 10.1103/PhysRevLett.119.150502. URL: https://link.aps.org/doi/10.1103/PhysRevLett.119.150502.

[36] Ruichao Ma et al. "Hamiltonian tomography of photonic lattices". In: *Phys. Rev. A* 95.6 (2017), p. 062120.

[37] Vladimir E Manucharyan et al. "Fluxonium: Single cooper-pair circuit free of charge offsets". In: *Science* 326.5949 (2009), pp. 113–116.

[38] John M Martinis. "Superconducting phase qubits". In: *Quantum Information Processing* 8.2-3 (2009), pp. 81–103.

[39] John M Martinis et al. "Rabi oscillations in a large Josephson-junction qubit". In: *Physical review letters* 89.11 (2002), p. 117901.

[40] David C. McKay et al. "High-Contrast Qubit Interactions Using Multimode Cavity QED". In: *Phys. Rev. Lett.* 114 (8 Feb. 2015), p. 080501. DOI: 10.1103/PhysRevLett.114.080501. URL: http://link.aps.org/doi/10.1103/PhysRevLett.114.080501.

[41] David C McKay et al. "Universal Gate for Fixed-Frequency Qubits via a Tunable Bus". In: *Phys. Rev. Appl.* 6.6 (2016), p. 064007.

[42] Marios H Michael et al. "New class of quantum error-correcting codes for a bosonic mode". In: *Phys. Rev. X* 6.3 (2016), p. 031006.

[43] Mazyar Mirrahimi et al. "Dynamically protected cat-qubits: a new paradigm for universal quantum computation". In: *New Journal of Physics* 16.4 (2014), p. 045014.

[44] Christopher R Monroe, Robert J Schoelkopf, and Mikhail D Lukin. "Quantum connections". In: *Scientific American* 314.5 (2016), pp. 50–57.

[45] JE Mooij et al. "Josephson persistent-current qubit". In: *Science* 285.5430 (1999), pp. 1036–1039.

[46] RK Naik et al. "Random access quantum information processors using multimode circuit quantum electrodynamics". In: *Nature Communications* 8.1 (2017), p. 1904.

[47] Yasunobu Nakamura, Yu A Pashkin, and JS Tsai. "Coherent control of macroscopic quantum states in a single-Cooper-pair box". In: *nature* 398.6730 (1999), p. 786.

[48] Francois Nguyen et al. "Quantum Interference between Two Single Photons of Different Microwave Frequencies". In: *Phys. Rev. Lett.* 108 (16 Apr. 2012), p. 163602. DOI: 10.1103/PhysRevLett.108.163602. URL: http://link.aps.org/doi/10.1103/PhysRevLett.108.163602.

[49] Jeremy L O'Brien et al. "Quantum process tomography of a controlled-NOT gate". In: *Phys. Rev. Lett.* 93.8 (2004), p. 080502.

[50] Nissim Ofek et al. "Extending the lifetime of a quantum bit with error correction in superconducting circuits". In: *Nature* 536 (2016), pp. 441–445.

[51] Edward Mills Purcell. "Spontaneous emission probabilities at radio frequencies". In: *Confined Electrons and Photons*. Springer, 1995, pp. 839–839.

[52] Robert Raussendorf, Daniel E Browne, and Hans J Briegel. "Measurement-based quantum computation on cluster states". In: *Phys. Rev. A* 68.2 (2003), p. 022312.

[53] Matthew Reagor et al. "Quantum memory with millisecond coherence in circuit QED". In: *Phys. Rev. B* 94.1 (2016), p. 014506.

[54] Matthew Reagor et al. "Reaching 10 ms single photon lifetimes for superconducting aluminum cavities". In: *App. Phys. Lett.* 102.19, 192604 (2013), p. 192604. DOI: http://dx.doi.org/10.1063/1.4807015. URL: http://scitation.aip.org/content/aip/journal/apl/102/19/10.1063/1.4807015.

[55] M. D. Reed et al. "High-Fidelity Readout in Circuit Quantum Electrodynamics Using the Jaynes-Cummings Nonlinearity". In: *Phys. Rev. Lett.* 105 (17 Oct. 2010), p. 173601. DOI: 10.1103/PhysRevLett.105.173601. URL: http://link.aps.org/doi/10.1103/PhysRevLett.105.173601.

[56] A Romanenko et al. "Ultra-high quality factors in superconducting niobium cavities in ambient magnetic fields up to 190 mG". In: *App. Phys. Lett.* 105.23 (2014), p. 234103.

[57] David Isaac Schuster. *Circuit quantum electrodynamics*. Yale University, 2007.

[58] Peter W Shor. "Scheme for reducing decoherence in quantum computer memory". In: *Physical review A* 52.4 (1995), R2493.

[59] I Siddiqi et al. "Dispersive measurements of superconducting qubit coherence with a fast latching readout". In: *Physical Review B* 73.5 (2006), p. 054510.

[60] AJ Sirois et al. "Coherent-state storage and retrieval between superconducting cavities using parametric frequency conversion". In: *App. Phys. Lett.* 106.17 (2015), p. 172603.

[61] Chunhua Song et al. "Reducing microwave loss in superconducting resonators due to trapped vortices". In: *App. Phys. Lett.* 95.23 (2009), p. 232501.

[62] Andrew Steane. "Multiple-particle interference and quantum error correction". In: *Proceedings of the Royal Society of London A: Mathematical, Physical and Engineering Sciences*. Vol. 452. 1954. The Royal Society. 1996, pp. 2551–2577.

[63] J. D. Strand et al. "First-order sideband transitions with flux-driven asymmetric transmon qubits". In: *Phys. Rev. B* 87 (22 June 2013), p. 220505. DOI: 10.1103/PhysRevB.87.220505. URL: http://link.aps.org/doi/10.1103/PhysRevB.87.220505.

[64] M. Tinkham. *Introduction to Superconductivity*. Dover Books on Physics Series. Dover Publications, 2004. ISBN: 9780486134727. URL: https://books.google.com/books?id=VpUk3NfwDIkC.

[65] John S Toll. "Causality and the dispersion relation: logical foundations". In: *Phys. Rev.* 104.6 (1956), p. 1760.

[66] Uri Vool and Michel Devoret. "Introduction to quantum electromagnetic circuits". In: *International Journal of Circuit Theory and Applications* 45.7 (2017), pp. 897–934.

[67] A. Wallraff et al. "Approaching Unit Visibility for Control of a Superconducting Qubit with Dispersive Readout". In: *Phys. Rev. Lett.* 95 (6 Aug. 2005), p. 060501. DOI: 10.1103/PhysRevLett.95.060501. URL: http://link.aps.org/doi/10.1103/PhysRevLett.95.060501.

[68] Fei Yan et al. “The flux qubit revisited to enhance coherence and reproducibility”. In: *Nature communications* 7 (2016), p. 12964.

[69] Eva Zakka-Bajjani et al. “Quantum superposition of a single microwave photon in two different ‘colour’ states”. In: *Nat. Phys.* 7.8 (Aug. 2011), pp. 599–603. ISSN: 1745-2473. DOI: 10.1038/nphys2035. URL: http://dx.doi.org/10.1038/nphys2035.